Longitudinal Atom Optics: Measuring the Density Matrix of a Matter Wave Beam

by

Richard Alan Rubenstein
A.B. Amherst College (1993)

Submitted to the Department of Physics
in partial fulfillment of the requirements for the degree of

Doctor of Philosophy

at the

MASSACHUSETTS INSTITUTE OF TECHNOLOGY

February 1999

Author _____
Department of Physics
December 17, 1998

Certified by _____
David E. Pritchard
Professor of Physics
Thesis Supervisor

Accepted by _____
Thomas J. Greytak
Associate Department Head for Education

Longitudinal Atom Optics: Measuring the Density Matrix of a Matter Wave Beam

by

Richard Alan Rubenstein

A.B. Amherst College (1993)

Submitted to the Department of Physics
on December 17, 1998, in partial fulfillment of the
requirements for the degree of
Doctor of Philosophy

Abstract

This thesis describes recent developments of theoretical and experimental techniques for longitudinal atom optics and interferometry, in which time-dependent interactions are used to create coherences in the longitudinal momentum of a matter wave.

We present a fully quantum mechanical treatment of the classic molecular beams resonance experiment, a beam of two state particles interacting with temporally oscillating potentials, showing that such oscillatory potentials shift not only the internal state, but also the momentum of an incident matter wave. Amplitude modulation of a matter wave adds coherent momentum sidebands within a single internal state. Two successive differentially detuned separated oscillatory fields (DSOF) can be used to detect a pre-existing momentum superposition or create one that rephases downstream. Phase modulation also generates coherent momentum sidebands which can rephase into amplitude modulation at a sufficient distance downstream.

We employed a DSOF longitudinal atom interferometer to search for off-diagonal density matrix elements produced by a supersonic atom source. This search placed a stringent upper bound on the size of the off-diagonal matrix elements which could have been present within the limits of our search, effectively ruling out the existence of coherent wavepackets in the beam in this range.

The DSOF interferometer, along with a novel deconvolution method, was used to measure the density matrix of a longitudinally modulated atomic beam which possessed complicated structure both along and off the diagonal. The results of this experiment, the first to determine the longitudinal quantum state of a matter wave beam, are compared with theoretical predictions.

Thesis Supervisor: David E. Pritchard
Title: Professor of Physics

To Patricia

and

our family

MEDITATION ON STATISTICAL METHOD

Plato, despair!
We prove by norms
How numbers bear
Empiric forms,

How random wrong
Will average right
If time be long
And error slight,

But in our hearts
Hyperbole
Curves and departs
To infinity.

Error is boundless.
Nor hope nor doubt,
Though both be groundless,
Will average out.

— J. V. Cunningham

Contents

1 Introduction **10**

1.1 Longitudinal Atom Optics and the Density Matrix 11

1.2 Historical Background of Longitudinal Atom Optics 13

1.3 Structure of Thesis 15

2 Longitudinal Atom Optics: Theory **17**

2.1 Introduction to Longitudinal Atom Optics and Interferometery 17

2.2 Paper: Longitudinal Atom Optics with Localized Oscillating Fields: A Fully Quantum Mechanical Treatment 20

2.2.1 Introduction 20

2.2.2 Creating Entanglements with a Single Oscillatory Field 23

2.2.3 Differentially Detuned Separated Oscillatory Fields 27

2.2.4 Amplitude Modulation 29

2.2.5 Velocity Spread and Remote Quantum Rephasing 32

2.2.6 Measuring Upstream Coherence with DSOF 35

2.2.7 Phase Modulation 37

2.2.8 Conclusion 42

2.2.9 Appendix: Classical Derivation of Rephased Fringes 43

2.3 More on the Semiclassical Approximation 47

3 Measuring the Density Matrix with DSOF **52**

3.1 The Density Matrix 52

3.2 DSOF Deconvolution Scheme 56

3.3 Semiclassical Interpretation of the Deconvolution Scheme 60

4 Apparatus **63**

4.1 Beam Machine 63

4.1.1 Source 65

4.1.2 Detector 66

4.1.3 Vacuum System 68

4.2 Experimental Realization of LAO Devices 69

4.2.1 Beamline 72

4.2.2 Radiofrequency Electronics 74

4.3 General Data Acquisition Procedures: Aligning the Beam and Optimizing Resonance Regions 78

4.3.1 Beam Alignment 78

4.3.2 Single Coil Linewidth Enhancement 79

5 Search for Off-Diagonal Matrix Elements **83**

5.1 Introduction to Search 83

5.2 Paper: Search for Off-Diagonal Density Matrix Elements for Atoms in a Supersonic Beam 85

5.2.1 Using DSOF to Search for Off-Diagonal Matrix Elements . . . 87

5.2.2 Conclusion 92

5.3 Theoretical Issues for the Source Search 95

5.3.1 Search Resolution and Range 95

5.3.2 Amplitude Modulation Index and Signal Contrast 96

5.3.3 Sensitivity to Non-AM ODEs 97

5.4 Data Analysis 97

5.4.1 Calibration 98

5.4.2 Data Acquisition 101

5.4.3 Establishing a Confidence Level 103

5.4.4 Instrument Response 106

6 Deconvolving the Density Matrix of a Longitudinally Modulated Atomic Beam **110**

6.1 Introduction to Deconvolution Experiment 110

6.2 Paper: Measurement of the Density Matrix of a Longitudinally Modulated Atomic Beam 112

6.2.1 Measuring the Density Matrix 115

6.2.2 Experiment 117

6.2.3 Conclusion 120

6.3 Theoretical Issues 122

6.3.1 Three-State Double AM 122

6.3.2 Double AM Density Matrix 124

6.4 Deconvolution Data Acquisition 128

6.5 Analysis and Modeling 133

A Paper: Determining the Density Matrix of a Molecular Beam Using a Longitudinal Matter Wave Interferometer **137**

List of Figures

2-1 Kinetic energy surplus for detuned RF transition 18
2-2 DSOF interferometer 27
2-3 DSOF interferometer to detect phase modulation 41
2-4 Transverse and longitudinal Talbot length 49
2-5 Longitudinal Talbot effect: PM $\rightarrow$ AM 50

3-1 Alternate density matrix coordinates 54
3-2 DSOF interferometer employed to measure density matrix 56

4-1 Apparatus schematic 64
4-2 Detector frequency response 67
4-3 Na level structure 71
4-4 Beamline for LAO experiments 73
4-5 Schematic of single sideband modulator 76
4-6 Schematic of double AM circuit 77
4-7 Ramsey fringes 80
4-8 Single coil resonance scans with and without power boost 81
4-9 Rabi profile scan with single sideband modulator 82

5-1 Schematic of source search experiment 88
5-2 Rephasing peak 90
5-3 P_{ave} for calibration AM 92
5-4 Source search data and instrument response 93
5-5 Simulated data and fit for periodogram behavior 99

5-6 Time-dependent data for determining contrast of calibration AM . . . 100
5-7 Contrast as a function of periodogram peak height and $\overline{n}$ 101
5-8 Rephasing peak 102
5-9 Histogram of search data peak heights 105
5-10 Close-up of histogram of search data peak heights 105
5-11 Mean counts/sample over range of search 107
5-12 Contrast over range of search 107
5-13 Mean counts/sample and contrast as a function of Ω_{coh} 108
5-14 Instrument response function of source search experiment 109

6-1 Schematic of density matrix deconvolution experiment 114
6-2 Ramsey fringes for double amplitude modulated atomic beam 118
6-3 Amplitude and phase of density matrix 119
6-4 Time-dependent signal produced by double AM 125
6-5 Double AM phase space paths 127
6-6 Mean velocity and velocity width as a function of detector position . 130
6-7 Data and model rephased Ramsey fringes 132
6-8 $\Omega_{coh} = 2\omega_m$ stripe of density matrix for various $\theta_{1,2}$ 136

Chapter 1

Introduction

Motion on the microscopic scale is described by the Schrödinger equation, which predicts that every particle has a wavelength $\lambda = \frac{h}{p}$ (de Broglie's relation [1]), where h is Planck's constant and p is the particle momentum. While the small size of h generally prevents observation of wave mechanical phenomena in the macroscopic world, the wave nature of particle motion has been not only confirmed, but also put to use in a long series of experiments, beginning with the demonstration of diffraction and interference for electrons [2, 3, 4, 5, 6], and continuing in studies of neutrons [7, 8].

Over the last quarter century the new disciplines of atom optics and interferometry, which examine the wave behavior of larger particles possessing many internal degrees of freedom, have pushed at the boundary between the microscopic and macroscopic world, demonstrating diffraction of atoms [9, 10, 11] and molecules [12, 13]. The atom interferometer [14], in which atomic de Broglie waves are coherently split and recombined, has emerged as a powerful tool, providing insight into fundamental questions of wave particle duality and quantum measurement theory [15] as well as techniques for measuring fundamental constants [16], atomic properties [17], gravitational acceleration [18, 19], and rotation [20, 21].

To date, most atom interferometers have employed transverse atom optical elements, which coherently shift the momentum of the de Broglie wave perpendicular to its propagation direction, in order to split and recombine the beams. A number of

different techniques, including Raman-Nath [11, 22] and Bragg [23] scattering from standing light waves [24, 25], optical Ramsey interferometry [26], and microfabricated structures [27, 28] have been used to create such transverse interferometers.

However, longitudinal atom optics and interferometry, in which the momentum of a matter wave is shifted parallel to its direction of motion, have been relatively unexplored, despite the interesting new possibilities that they offer. This thesis describes recent theoretical and experimental developments in the field of longitudinal atom optics and interferometry performed in the Pritchard group at MIT. These theoretical developments provide a valuable addition to the field of atom optics, extending important transverse atom optical concepts to the longitudinal case. Our longitudinal atom optics experiments served not only to demonstrate these techniques, but also to provide the first direct measurements of the longitudinal quantum state of an atomic beam.

1.1 Longitudinal Atom Optics and the Density Matrix

Longitudinal atom optics (LAO) is the coherent manipulation of the longitudinal center of mass motion of an atom wave. The longitudinal coherences produced by LAO are intrinsically time-dependent (in contrast to transverse momentum coherences) because they involve changes in the total energy of an incident wave. To alter the energy, LAO elements must employ non-conservative, time-dependent potentials. If such potentials are resonant, they can change the internal state of the atom and entangle the internal degrees of freedom with the external momentum. Non-resonant potentials, which generate a coherent superposition of energy/momentum components (coherences) in a single internal state, can also be employed to alter the longitudinal energy of an incident wave.

LAO provides a new set of tools for the investigation and manipulation of the quantum state of atomic beams. This allows the implementation of new devices

such as longitudinal beamsplitters and longitudinal atom interferometers, which can create high frequency pulses of atoms. The LAO experiments which we describe below inhabit the borderland between quantum and classical physics; hence these investigations provide fresh insight into the relationship between the two regimes. The extension of LAO techniques into the slow atom regime would hold out the possibility of producing useful atom optical devices such as an atomic Fabry-Perot cavity.

The most immediate application of LAO techniques is the study of the momentum coherence properties of atomic beams. Despite the ubiquity of such beams in atomic physics, no previous experiment has been able to investigate the quantum state of the longitudinal degree of freedom of this system.

To gain the most complete possible quantum description of this (or any) system, we must determine its density matrix, which contains information not only about coherent superpositions of different basis states, but also about incoherent averages over the ensemble of atoms being observed [29]. The density matrix (or equivalently the Wigner function, to which it is closely related), has been the subject of much interest in quantum measurement theory [30, 31, 32, 33]. Recent experiments with light [34], the vibrational mode of a diatomic molecule [35], and trapped ions [36] have successfully demonstrated measurements of the density matrix or Wigner function of these systems. The study of the Wigner function of the transverse degree of freedom of atoms in a beam has also been the subject of a great deal of theoretical discussion [37, 38, 39, 40], culminating in a recent measurement [41]. This thesis describes the first experimental measurement of the longitudinal energy/momentum density matrix of a matter wave beam, which we achieve through application of the techniques of LAO.

1.2 Historical Background of Longitudinal Atom Optics

This section provides a brief discussion of previous theoretical and experimental work that relates to our development of longitudinal atom optics.

The roots of our approach to longitudinal atom optics lie in the classic radiofrequency molecular beam resonance experiments performed at the dawn of modern atomic physics. In the late 1930's Rabi developed the technique of molecular beam resonance [42, 43], in which oscillatory magnetic fields are employed to drive transitions between internal energy levels of atoms or molecules. This technique was originally employed to obtain precise measurements of the magnetic moments of various atoms and molecules [43], but its basic concern, the two state resonance problem, is now our fundamental model for understanding the interaction of atomic and molecular systems with electromagnetic radiation.

In 1950, Ramsey demonstrated that two oscillatory field resonance regions placed in succession could be employed to provide a significantly narrower resonance lineshape than Rabi's single field resonance [44, 45]. This separated oscillatory field (SOF) method, which can be interpreted as an atom interferometer in internal state space, is now a standard atomic physics technique.

The Ramsey SOF method was subsequently extended from the radiofrequency to the optical regime. It was then pointed out that such optical Ramsey experiments constitute atom interferometers not only in internal state space, but also in external momentum space as well [46, 47], since the momentum recoil caused by absorption of an optical photon shifts the transverse momentum of the excited state relative to the ground state.

In addition to linking the Ramsey resonance method to atom interferometery, this observation prefigures the development of longitudinal atom optics: by angling the incident lasers so that they are no longer perpendicular to the atomic beam propagation direction, longitudinal momentum shifts can be imparted to the atoms. Longitudinal atom interferometers have also been developed using non-resonant methods of

preparing superpositions of different internal states [48]. However, these longitudinal atom interferometers do not employ time-dependent optical elements, and hence are incapable of altering the total energy of an incident atom wave and creating a time-dependent superposition.

The techniques of spin resonance, initially developed by Rabi and Ramsey in the context of atomic physics, have also been employed in the study of neutrons, where they stimulated the performance of a number of experiments with relevance to LAO. In particular, theoretical treatments of neutron spin echo [49, 50] and neutron resonance spin echo [51, 52] have espoused the idea that oscillating magnetic fields affect the external degree of freedom of a propagating matter wave. Experimental developments in this field include devices which can be employed to measure small changes in kinetic energy of a neutron [51] or ^{3}He [53] inelastically scattered from a target.

Neutron spin resonance was also combined with transverse neutron interferometry, in an experiment which employed resonant oscillatory fields of differing frequencies applied to the two spatially separated beams of a transverse single crystal neutron interferometer [54]. The time-dependent interference signal observed in this experiment is the result of the interference of two plane wave states differing in total energy, the hallmark of longitudinal matter wave optics.

Another precursor of LAO is a series of theoretical and experimental papers in which oscillatory, but non-resonant, potentials are used to alter the longitudinal energy/momentum of an incident matter wave. In 1952, Moshinsky [55] pointed out that a matter wave propagating through an abruptly opened shutter should exhibit temporal amplitude oscillations downstream which are analogous to the transverse spatial fringes which occur when a plane wave passes a sharp edge (Fresnel diffraction). Later theoretical treatments of both resonant [56, 57] and non-resonant [58, 59, 60, 61, 62] time-dependent Hamiltonians have pointed out the ability of such potentials to modify the energy/momentum spectrum of matter waves.

This theoretical work on the longitudinal energy effects of time-dependent potentials has lead to a number of experimental studies. In recent slow neutron ex-

periments, coherent multiphoton [63] and multiphonon [64] exchanges, caused by the application of periodic phase modulation, have been observed. Experiments with cold atoms have demonstrated phase modulation [65] and atomic diffraction and interference with temporal slits [66].

For the case of fast atoms, Bragg diffraction from an amplitude modulated standing light wave has been employed to coherently shift atomic longitudinal kinetic energy [67]. A great deal of work in longitudinal atom optics and interferometry with fast atomic beams has also been performed in our group at MIT over the last three years. Our experiments, which include the demonstration of novel longitudinal atom beamsplitters and of a differentially detuned separated oscillatory field (DSOF) interferometer [68], as well as the application of these devices to the study of the longitudinal energy/momentum density matrix [69, 70], can be seen as re-interpretations and extensions of the classic molecular beams experiments of Rabi and Ramsey.

1.3 Structure of Thesis

The main results of this thesis are contained in four papers, two discussing theoretical topics and two describing experimental results. These papers are included in the thesis, along with supplemental material for each that contains additional derivations, data analysis, and experimental details.

Chapter 1 (this one) contains brief discussions of the historical context of atom optics in general and of LAO in particular.

Chapter 2 provides a theoretical development of the subject of longitudinal atom optics, and describes the function of the main LAO elements that we employ in our experiments: longitudinal beamsplitters and the DSOF longitudinal interferometer. The heart of this chapter is a paper, "Longitudinal Atom Optics with Localized Oscillating Fields: A Fully Quantum Mechanical Treatment," which has been submitted to Physical Review A. This chapter also further discusses the semiclassical limit in LAO.

Chapter 3 develops the theory of the density matrix of a matter wave beam in the

longitudinal energy/momentum basis, with particular attention to the importance of off-diagonal matrix elements. This chapter also describes the DSOF density matrix deconvolution scheme developed by our group, which is discussed in a paper, "Determining the Density Matrix of a Molecular Beam Using a Longitudinal Matter Wave interferometer," published in the Journal of Modern Optics and included as Appendix A of this thesis. This chapter concludes with a discussion of a semiclassical interpretation of our quantum deconvolution scheme.

Chapter 4 provides a description of the experimental apparatus with which we performed our LAO experiments. Since this apparatus has been described in great detail in a previous thesis [71], this description focuses on changes to the device and on new techniques which enabled our recent experiments.

Chapter 5 contains a discussion of an experiment in which we employed our DSOF longitudinal interferometer to search for off-diagonal density matrix elements in our supersonic atomic beam. This work, which is the first experimental investigation of the longitudinal quantum state of an atomic beam, is described in a paper, "Search for Off-Diagonal Density Matrix Elements for Atoms in a Supersonic Beam," which has been submitted to Physical Review Letters. This paper is followed by a description of the data analysis procedures employed in this experiment.

Chapter 6 presents the results of our experimental measurement of the longitudinal energy/momentum density matrix of an atomic beam possessing complicated structure both along and off the diagonal. The main elements of this experiment are presented in the draft of a paper "Measurement of the Density Matrix of a Longitudinally Modulated Atomic Beam," to be submitted to Physical Review Letters. This chapter also includes a brief discussion of the double amplitude modulation scheme which we employed to create the measured density matrix, along with additional data not presented in the paper.

Chapter 2

Longitudinal Atom Optics: Theory

This chapter develops some of the tools of longitudinal atom optics, describing how localized oscillatory fields can be employed to generate entanglements and energy/momentum coherences. Various LAO elements are discussed, including amplitude and phase modulation longitudinal beamsplitters. Two successive differentially detuned separated oscillatory fields (DSOF) comprise a longitudinal atom interferometer. The chapter concludes with a discussion of the semiclassical limit in LAO.

2.1 Introduction to Longitudinal Atom Optics and Interferometery

This section provides a brief qualitative introduction to some of the main themes of longitudinal atom optics. A full derivation of these is presented in Sec. 2.2.

Our development of longitudinal atom optics is based on a fully quantum mechanical treatment of an atomic beam interacting with localized oscillating fields, in which the center of mass coordinate of the longitudinal motion of the atoms is represented as a coherent matter wave. This fully quantum picture is in contrast to the usual analysis of atomic beam resonance, in which the atom is treated as a point particle

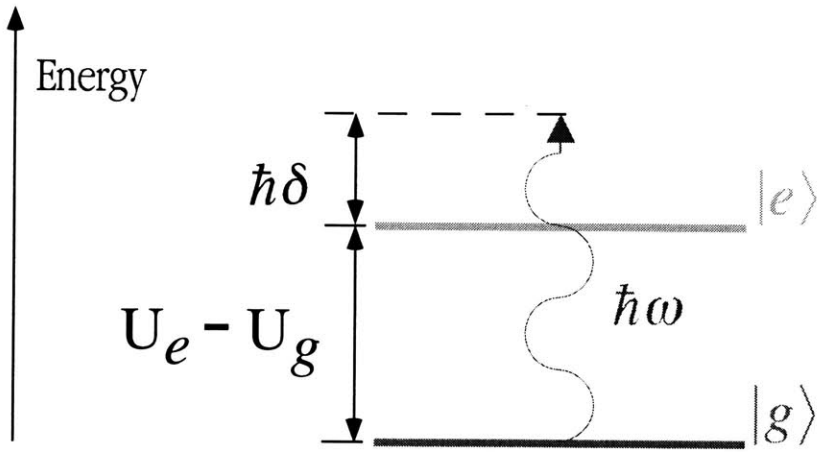

Figure 2-1: For a fast atomic beam, the energy surplus or deficit caused by detuning the applied radiation from the atomic resonance is compensated by a shift $\hbar\delta$ in the atomic kinetic energy.

traveling on a classical trajectory, with the oscillatory field turned on and off as a function of time.

In general, a change in the longitudinal momentum $\hbar k$ of a free matter wave necessitates a change in its total energy $\frac{\hbar^2 k^2}{2m}$, which in turn requires the application of a time-dependent potential. We use this quantum mechanical center of mass viewpoint to describe a number of time-dependent LAO elements which can coherently shift an incident matter wave's energy and momentum.

We first consider the Rabi two-state resonance problem, in which an atomic plane wave traverses a short region containing a radiofrequency oscillatory field which couples two internal atomic energy levels U_e and U_g (where $U_e > U_g$). In our fully quantum analysis, the kinetic energy (and hence the momentum) of the matter wave is altered when the atom undergoes a transition that is detuned from resonance.

Figure 2-1 shows a pictorial representation of this energy shift, which is a consequence of the conservation of energy as the atom absorbs a single quantum of energy $\hbar\omega$ from the oscillatory field. The total energy of the atom in the excited (ground) state is $\hbar\Omega_{e(g)} = \frac{(\hbar k_{e(g)})^2}{2m} + U_{e(g)}$ where m is the atomic mass. In the limit of a fast atomic beam ($U_{e(g)}, \omega \ll \Omega_{e(g)}$) the kinetic energy shift is approximately equal to $\hbar\delta$, where $\delta = \omega - \frac{U_e - U_g}{\hbar}$ is the detuning of the applied oscillatory field from resonance.

The energy shift caused by a detuned transition means that a resonance region not

only changes an atom's internal state, but also entangles internal and external degrees of freedom. Thus, a resonance region can function as a beamsplitter in longitudinal energy/momentum space: an incoming plane wave with a single total energy can emerge in a coherent superposition of two different energies/momenta.

Time-dependent but non-resonant interactions, such as amplitude modulation (AM) and phase modulation (PM), function as longitudinal beamsplitters which create coherent superpositions of different energy/momentum states (sidebands) in a single internal state. Amplitude modulation of a matter wave beam can be created by periodic modulation, or chopping, of an incident beam, which causes partial longitudinal localization of the downstream atomic probability whose description requires a coherent superposition of plane wave states with more than one wavelength. A matter wave can be phase modulated by passage through a region of periodically varying potential $U_g(t)$, which creates a periodic modulation of the phase of the wavefunction at the end of the PM region. In both cases, a Fourier transform of the downstream wavefunction reveals the presence of energy sidebands.

Longitudinal atom optical elements, as in transverse optics, can be combined to create useful devices. Two differentially detuned separated oscillatory fields (DSOF) constitute a longitudinal atom interferometer, which we employ for most of our LAO experiments. The two field regions of the DSOF can apply two different energy shifts $\hbar\omega_{1,2}$ to an incident matter wave, creating a coherent superposition of energy/momentum components in a single internal state. Conversely, two incident plane wave components with initially distinct energies can be overlapped by the DSOF, allowing comparison of their relative phase. The DSOF can also reverse the effects of the vacuum dispersion (wavepacket spreading) of matter waves in a technique analogous to the second half of a spin echo [72].

2.2 Paper: Longitudinal Atom Optics with Localized Oscillating Fields: A Fully Quantum Mechanical Treatment

D. E. Pritchard, R. A. Rubenstein, A. Dhirani, D. A. Kokorowski,
E. T. Smith, T. D. Hammond, and B. Rohwedder[1]

Massachusetts Institute of Technology,
Cambridge, Massachusetts 02139

Abstract

We develop a number of novel longitudinal atom optics devices, through a fully quantal treatment of a beam of two state particles interacting with temporally oscillating potentials. A single oscillatory potential, in coupling the two internal states, generally entangles each with a different longitudinal momentum. An oscillatory potential can also act as an amplitude modulator, creating momentum coherences within a single internal state. Two successive oscillatory fields, if differentially detuned (DSOF), can couple an initially monochromatic state to a coherent momentum superposition, or alternatively may be used to detect a pre-existing momentum superposition. DSOF can also create amplitude modulation which, despite the presence of a broad velocity distribution, rephases at a selected distance downstream of the device. Phase modulation also generates coherent momentum sidebands which can evolve into amplitude modulation at a particular location downstream.

PACS: 03.75.Be,03.75.Dg,39.20.+q,32.80.Lg

2.2.1 Introduction

Past work in atom optics and interferometry has focused overwhelmingly on transverse momentum coherences [14], leaving the study and application of entanglements and coherences involving longitudinal momentum largely untapped despite interesting new possibilities that they offer. Longitudinal coherences are superpositions of states whose momenta have different magnitudes, and hence different kinetic and total

[1]Current Address: Facultad de Física Pontificia Universidad Católica de Chile, Casilla 306, Santiago 22, Chile.

energy. Such superpositions are inherently time-dependent, a qualitative distinction vis a vis transverse coherences. Their creation, manipulation and detection therefore involve time-dependent interactions.

Manipulation of longitudinal momentum is beginning to receive attention in the literature. Theoretical treatments of resonance interactions employing the longitudinal motion of particles have been presented [52, 57, 73, 74, 75, 76], as have theoretical studies of the effects of a time-dependent shutter on the downstream wave amplitude [55, 58, 59, 77]. Several papers have addressed the subject of time-dependent but non-resonant interactions as well [57, 60, 61, 78]. A number of groups have experimentally demonstrated the ability of time-dependent potentials to coherently shift and manipulate the longitudinal momentum of either pulsed or continuous beams of both neutrons [63, 64, 79, 80] and atoms [53, 65, 66, 67, 68].

Longitudinal atom optics provides a new set of tools for the manipulation and control of the quantum state of matter wave beams, and may allow the study of small momentum shifts and the production of rapidly pulsed atom sources. In addition, it points the way towards the creation of novel devices such as longitudinal atom interferometers and beam splitters. The techniques of longitudinal atom optics also provide a method of probing the coherence structure of atomic beams [81], and can shed new light on their correct quantum description, a subject of some controversy in recent years [82, 83, 84, 85].

In this paper we present a theoretical development of several longitudinal atom optical devices. The key to demonstrating these is our treatment of atomic beams in which the longitudinal momentum of the atoms is fully quantum mechanical. This treatment reveals (Sec. 2.2.2) that passage of the beam through a single near resonant oscillatory field region can entangle each internal state with a different longitudinal momentum. By placing two of these oscillatory field regions in succession, each with a different excitation frequency, we create a novel longitudinal interferometer called DSOF (Differential Separated Oscillatory Fields), an extension of Ramsey's method [44, 45], as described in Sec. 2.2.3. We note that time-independent but spatially changing fields [86] can form similar entanglements that are time-independent; these

have also been combined to form longitudinal interferometers [48].

We discuss in Sec. 2.2.4 an amplitude modulated oscillatory field region, showing that this process can create an amplitude modulated atomic beam possessing coherent momentum sidebands. While the effects of a time-dependent shutter [55, 58, 77] on the downstream wave amplitude have been considered before, ours is the first treatment of continuous amplitude modulation of a plane matter wave.

Unfortunately real atomic beams are not monochromatic, necessitating consideration of the effects of their velocity spread. Since the momentum change caused by an amplitude modulation region depends inversely on the velocity of the atom, the spatial period of the imposed modulation is different for atoms of differing velocities, causing the modulation to average away downstream of the region. In Sec. 2.2.5 we demonstrate that our DSOF technique can compensate for this averaging via a rephasing technique analogous to a spin echo [72] or a neutron spin echo [49, 52, 87]. In our scheme, the DSOF acts on a atomic beam like a virtual amplitude modulator situated at a selected downstream location. A real amplitude modulator at that location is able to detect the modulation imposed by the DSOF. In Sec. 2.2.6, we show how DSOF can detect coherences created by an upstream amplitude modulator.

Section 2.2.7 treats phase modulation, another method of adding coherent momentum sidebands to a matter wave. Phase modulation of matter waves has been the subject of much recent interest, as evidenced by demonstrations using non-resonant oscillatory field regions [63] as well as vibrating mirrors [64, 65]. We show that phase modulation sidebands cannot be detected by intensity detectors even in conjunction with amplitude modulation regions unless sufficient downstream propagation is allowed. However, phase modulation can be observed if it is applied to only one of the atom's states in between the two oscillating field regions of a DSOF interferometer.

Finally, in an appendix, we discuss the relationship between our fully quantum mechanical treatment of atomic beam resonance and the standard treatment which assumes classical motion of the center of mass.

2.2.2 Creating Entanglements with a Single Oscillatory Field

In standard RF (or Rabi) resonance experiment [88] a beam of two-state atoms or molecules, assumed monochromatic for now, interacts with a spatially localized field oscillating at frequency ω. The two internal states of the atom have potential energy $U_{e,g}$, with $U_e > U_g$. We represent the *total* (kinetic plus potential) energy of each state as $\hbar\Omega_{e,g}$, hence the wave vector is

$$k_{e,g} = [2m(\hbar\Omega_{e,g} - U_{e,g})]^{1/2}/\hbar, \tag{2.1}$$

and the wavefunction representing a freely propagating atom in a single state is

$$\Psi_{e,g}(\Omega_{e,g}, x, t) = e^{i(k_{e,g}x - \Omega_{e,g}t)}|e,g\rangle, \tag{2.2}$$

which is an eigensolution of the Hamiltonian for the free atom,

$$H_o = -\frac{\hbar^2}{2m}\frac{\partial^2}{\partial x^2} + U_e|e\rangle\langle e| + U_g|g\rangle\langle g|. \tag{2.3}$$

The atom interacts with continuous monochromatic radiation, which we treat as a classical field, of frequency ω, via the Hamiltonian

$$H_{int} = \frac{\hbar\omega_R(x)}{2}\left[e^{-i\omega t}|e\rangle\langle g| + e^{i\omega t}|g\rangle\langle e|\right]. \tag{2.4}$$

The Rabi frequency, $\omega_R(x)$, is determined by the field strength of the radiation as a function of position. The radiation couples excited and ground states whose total energy differs by ω. This condition ($\Omega_e - \Omega_g = \omega$) conserves energy and also allows stationary solutions for the time-dependent Schrödinger equation of the form

$$\Psi(x,t) = a_g(x)e^{i(k_g x - \Omega_g t)}|g\rangle + a_e(x)e^{i(k_e x - \Omega_e t)}|e\rangle, \tag{2.5}$$

where the amplitudes, $a_{g,e}(x)$ vary with position, but *not* with time.

The evolution equations for the coefficients $a_{g,e}(x)$ are formed by substituting Eq. 2.5 into Schrödinger's equation and neglecting the second derivative of the coefficients.

This approximation is equivalent to the JWKB approximation, and is valid if the kinetic energy is much larger than both $U_e - U_g$ and $\hbar\omega_R(x)$, and if the applied potentials change slowly on the scale of the matter wavelength $\lambda = 2\pi/k_{e,g}$. The resulting equations are

$$\frac{\partial a_g(x)}{\partial x} = \frac{-i\omega_R(x)}{2v} e^{i\Delta k x} a_e(x) \tag{2.6}$$

$$\frac{\partial a_e(x)}{\partial x} = \frac{-i\omega_R(x)}{2v} e^{-i\Delta k x} a_g(x), \tag{2.7}$$

where

$$\begin{aligned} \Delta k &\equiv k_e - k_g \\ &= \frac{\sqrt{2m}}{\hbar}\left[(\hbar\Omega_g + \hbar\omega - U_e)^{1/2} - (\hbar\Omega_g - U_g)^{1/2}\right] \\ &\simeq \delta/v. \end{aligned} \tag{2.8}$$

The last line applies because in our approximation the kinetic energy is much larger than the Rabi energy, $\hbar\omega_R$, the potential energy $U_{e,g}$, and $\hbar\delta$, where we have defined the detuning

$$\delta = \omega - \frac{(U_e - U_g)}{\hbar}. \tag{2.9}$$

This assures that the velocities v_e and v_g are approximately equal to v, the longitudinal velocity of the beam.

In principle, Eqs. 2.6-2.7 can be solved (numerically if necessary) for an arbitrary oscillatory field profile $\omega_R(x)$. To demonstrate the qualitative features, we consider a square profile, which can be solved exactly:

$$\omega_R(x) = \begin{cases} \omega_R & \text{if } 0 < x < l \\ 0 & \text{otherwise} \end{cases} \tag{2.10}$$

for which we find the solution inside the oscillatory field

$$
\begin{aligned}
a_g(x) &= \left[\left(\cos\theta - \frac{i\Delta k}{\Delta k'}\sin\theta\right) a_{go} - \frac{ik_R}{\Delta k'}\sin\theta\ a_{eo}\right] e^{i\frac{\Delta k\, x}{2}} \\
a_e(x) &= \left[\left(\cos\theta + \frac{i\Delta k}{\Delta k'}\sin\theta\right) a_{eo} - \frac{ik_R}{\Delta k'}\sin\theta\ a_{go}\right] e^{-i\frac{\Delta k\, x}{2}}
\end{aligned}
\tag{2.11}
$$

for $0 < x < l$, where $k_R = \omega_R/v$, $\Delta k' = \sqrt{\Delta k^2 + k_R^2}$, $\theta = \Delta k' x/2$, and a_{go}, a_{eo} are the initial amplitudes in the ground and excited states respectively. These position dependent amplitudes reproduce the well-known Rabi oscillations in time if we employ the classical relation $x = vt$. One can determine the full wavefunction downstream of the oscillatory field zone by matching the wavefunction inside the oscillatory field, whose ground and excited state amplitudes are given by Eq. 2.11, to free plane wave solutions at $x = 0$ and $x = l$.

The most striking difference between the above fully quantal treatment of atomic beam resonance and the standard treatment occurs when $\delta \neq 0$, i.e. when $\hbar\omega$ differs from the internal energy separation $U_e - U_g$. In this case, when a particle makes a transition between internal levels, conservation of energy requires that its kinetic energy change, resulting in a momentum difference between the two coupled states according to Eq. 2.8. Thus, the particle exits the resonance region in a superposition of plane waves differing in both internal state and momentum—the resonance interaction has *entangled* momentum and internal states. By contrast, in the standard treatment of resonance the frequency of the oscillatory field is said to be broadened by the finite transit time of the atom through the spatially limited region of applied field, thus allowing internal state transitions with no momentum change.

We note that the plane wave description of resonance presented here is similar to the analysis of Golub *et al.* [52]. Our view is also similar to that of atom interferometry using lasers, where conservation of momentum determines which of the available photon momentum components in the laser is actually absorbed [76, 89].

Our treatment demonstrates that a single oscillatory field region acts as a longitudinal beamsplitter, transforming a single incident momentum into a coherent sum of

two outgoing momenta. The resonance region, in this sense, is analogous to a Stern-Gerlach magnet, which can transform an incoming spin quantized in the $\hat{z}$ direction into an outgoing coherent superposition of states quantized along $\pm\hat{x}$, each with a distinct transverse momentum.

The maximum attainable momentum difference between the radiatively coupled states is limited by the spatial profile of the oscillatory field $\omega_R(x)$ (which may in general have arbitrary shape, but vanishes outside the range $[0, l]$). For large momentum shifts (detunings), the amplitude in the excited state is small, $a_g \simeq 1$, and we can apply first order perturbation theory to obtain the excited state amplitude for $x > l$

$$a_e(\Delta k) \simeq \frac{-i}{2v} \int_0^l dx\, \omega_R(x) e^{-i\Delta k\, x}. \tag{2.12}$$

For smooth profiles of $\omega_R(x)$, the probability of making a transition falls off for $\Delta k > 1/l$, where off-resonant transitions are suppressed by the rapid oscillations of the $e^{-i\Delta k\, x}$ factor in Eq. 2.12. The corresponding frequency width of the resonance curve, $\Delta\omega \sim v\Delta k \sim v/l$, agrees with the limit derived from the usual finite transit time argument.

The transition-induced longitudinal momentum differences Δk are *not* related to or limited by the momentum of photons of frequency ω, even though the change in total energy *is* determined by $\hbar\omega$. For an RF resonance experiment, one can construct regions with l thousands of times smaller than the wavelength of the radiation, λ, yielding a maximum momentum difference, $\hbar\Delta k \sim \hbar/l$ thousands of times larger than h/λ, the corresponding photon momentum. Significantly, this large momentum can be transferred with high probability even when the oscillating field has the strength to transfer only a single photon (i.e. $\omega_R l/v \simeq \pi$). This large momentum transfer may be ascribed to the interaction of the particle's oscillating dipole moment with the gradients of the oscillating field at the ends of the RF region [90].

The fully quantum mechanical picture of resonance also explains the Doppler shifts that appear in laser spectroscopy, where a beam of laser radiation illuminates the atomic beam and causes coupling to some excited state. If the propagation direction

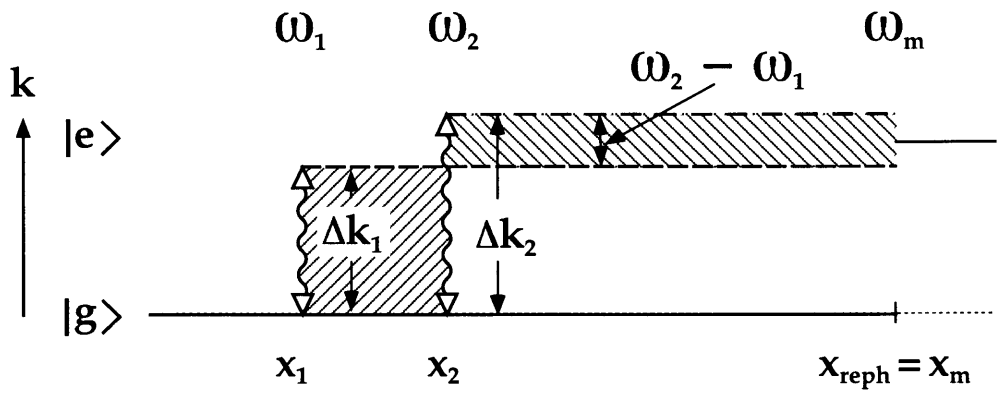

Figure 2-2: The DSOF interferometer is formed by oscillatory fields of frequency ω_1 (ω_2) applied at x_1 (x_2). Ground (excited) state plane wave components are shown as solid (dashed) lines. The left (right) hatched area denotes the differential phase accumulated by the atoms excited at x_1 (x_2). The ground state output port of the interferometer is not shown. As discussed in Sec. 2.2.5, an amplitude modulator can be placed at $x_{reph} = x_m$ in order to rephase the AM produced by the DSOF. In this case the total area, and hence the differential phase between the two momentum components, is equal to zero downstream of x_m.

of the laser radiation is not perpendicular to the atomic beam, then $\omega_R(x) \propto e^{ik_x x}$ where k_x is the component of the laser's k-vector along the atomic beam. When incorporated into Eq. 2.12 this will produce the usual Doppler shift observed from a misaligned laser, $\Delta\omega = k_x v$.

2.2.3 Differentially Detuned Separated Oscillatory Fields

Since passage through a single oscillatory field produces a coherence between the original ground state wavefunction and an excited state wavefunction whose momentum differs by $\hbar\Delta k = \hbar\delta/v$, it follows that passage through two successive oscillatory fields which are tuned to different frequencies, δ_1 and δ_2, can produce an excited state wavefunction whose momentum state is a superposition of two different momenta. We call the two differentially detuned separated oscillatory field regions "DSOF" to emphasize the similarity of this arrangement to the separated oscillatory fields (SOF) method of Ramsey [44], where $\delta_1 = \delta_2$.

The relevant geometry is pictured in Fig. 2-2, where the two oscillatory field regions are located at positions x_1, x_2. The output wavefunction for $x > x_2$ is deter-

mined by matching boundary conditions at the interfaces (not shown) between the oscillating field and field free zones, while neglecting reflection at these boundaries. For an incident wavefunction $\Psi(x,t) = e^{i(k_o x - \Omega_o t)}|g\rangle$, the wavefunction beyond the second oscillatory field is:

$$\begin{aligned}\Psi(x,t) &= \frac{1}{2}\left(e^{i(\phi_1+\phi_2)} - e^{-i(\phi_1-\phi_2)}e^{i[\Delta k_1(x_2-x_1)-(\Delta k_2-\Delta k_1)(x-x_2)-(\omega_1-\omega_2)t]}\right)e^{i(k_o x-\Omega_o t)}|g\rangle \\ &\quad -\frac{i}{2}\left(e^{-i(\phi_1+\phi_2)}e^{i[\Delta k_1(x-x_1)-\omega_1 t]} + e^{i(\phi_1-\phi_2)}e^{i[\Delta k_2(x-x_2)-\omega_2 t]}\right)e^{i(k_o x-\Omega_o t)}|e\rangle,\end{aligned} \tag{2.13}$$

where we have made the simplifying assumption that the field strength, ω_R, in the two field regions is tuned to produce nearly perfect $\pi/2$ pulses (i.e. $\theta \simeq \pi/2$ in Eq. 2.11). We have also defined $\phi_i \equiv \Delta k_i l_i/2$, and $\hbar\Delta k_i = \hbar\delta_i/v$, where l_i is the length of each square oscillatory field region (the index $i = 1,2$). For simplicity, in later equations we neglect ϕ_i, the phases due to the finite coil lengths, which merely cause a slight change in the effective value of $x_2 - x_1$.

If the frequencies of the two oscillatory field regions are equal, so that $\Delta k_1 = \Delta k_2 \simeq \delta/v$, this wavefunction is consistent with the standard SOF result [45] if we introduce the classical transit time through a resonance zone, $\tau = l/v$, and time of flight between zones, $T = (x_2 - x_1)/v$.

Both the original SOF configuration and the more general DSOF configuration can be interpreted as interferometers in momentum/internal state space. In each case, an incident particle in state $|g\rangle$ has two paths by which to reach state $|e\rangle$ at the interferometer output, namely excitation in either the first or second oscillatory field region (see Fig. 2-2). In SOF, the momentum shift $\hbar\Delta k$ which accompanies the change in internal state is the same for both paths; therefore both are excited into the same final momentum eigenstate with the same total energy. These two paths will exhibit time-independent interference, producing Ramsey fringes in the excited state probability as a function of detuning. The phase of this interference is just the additional phase, $\phi = \Delta k\,(x_2 - x_1)$, accrued by Path 1 relative to Path 2 in the

interval between the two oscillatory field zones.

A time-dependent interference occurs in the DSOF case because the two interfering paths are energy shifted by different amounts. The outgoing excited state (as well as the ground state) is a coherent superposition of two distinct total energy components, each with a different corresponding longitudinal momentum. The probability of detecting a particle in the excited state is the square of the coefficient of $|e\rangle$ in Eq. 2.13:

$$\begin{aligned} P_e &\simeq \frac{1}{2}\{1+\cos[\Delta k_1(x_2-x_1) \\ &\quad -(\Delta k_2-\Delta k_1)(x-x_2)-(\omega_1-\omega_2)t]\}. \end{aligned} \tag{2.14}$$

This coherent superposition produces a temporal oscillation in the detection probability at a frequency $\omega_1 - \omega_2$. In addition, the spatial contribution to the interference includes not only a term representing the phase accumulated between the two field regions $[\Delta k_1 (x_2 - x_1)]$, but also a contribution with opposite sign $[(\Delta k_2 - \Delta k_1)(x - x_2)]$ which is accumulated after the second region. A similar time-dependent signal can be obtained for more complex arrangements of oscillatory and static magnetic field regions as well (e.g. neutron resonance spin echo [52, 87]).

2.2.4 Amplitude Modulation

The temporally oscillating probability of observing excited state atoms after the DSOF (Eq. 2.14) indicates amplitude modulation (AM) of the excited state. By definition, AM of a plane wave involves a time-varying change in the amplitude of the wave propagating downstream from the point of modulation, causing an initially uniform wavefunction to have local maxima and minima in both time and space. In our plane wave picture, this longitudinal localization requires a coherent superposition of states with more than one longitudinal wavelength or momentum: AM acts as a beam splitter in longitudinal momentum space.

There are a number of ways to amplitude modulate an atomic beam. A periodic

chopper is a simple example of an amplitude modulator. Another, more sophisticated amplitude modulator is the DSOF discussed in the previous section, which produces an excited state wavefunction that is amplitude modulated, but with an additional phase shift that depends on the wavevector of the incoming wave. An effective and flexible amplitude modulator can also be realized with a single oscillatory field region which drives transitions to some undetected state. If the Rabi frequency $\omega_R(t)$ is time-dependent, it allows smooth temporal variation of the atomic transmission through the region. To demonstrate this, we again consider a beam of two-state atoms, initially in the ground state, incident on an oscillatory field region tuned exactly to resonance ($\delta = 0$). The ground state amplitude transmission function is

$$\begin{aligned} T(t) &= \cos\left(\frac{\omega_R(t)l}{2v} + \phi_m\right) \\ &= \cos\left(\omega_m t + \phi_m\right), \end{aligned} \tag{2.15}$$

where l is the length of the oscillatory field, ω_m is the desired modulation frequency, and ϕ_m is the phase of the modulator. The first line of Eq. 2.15 is valid only if $\omega_R(t)$ changes slowly in a time $t = l/v$. The second line follows from the choice $\omega_R(t) = 2\omega_m vt/l$. (Since the indefinite increase in field strength implied by this choice is impractical in a real experiment, a suitable triangle wave modulation of ω_R can be employed instead.) A more general treatment of amplitude modulation with resonance regions, including arbitrary spatial and temporal dependence of the field amplitude $\omega_R(x,t)$, will be given in a future paper.

In this section, we discuss two simple amplitude modulation schemes, both short spatial regions whose transmission coefficient varies periodically with time. Our treatment is steady state, in contrast with previous discussions [55, 58, 59, 77] of the transmission of a matter wave through a time-dependent shutter.

The first amplitude modulation scheme, called "suppressed carrier AM," employs the amplitude transmission function of Eq. 2.15. For simplicity, we assume a wavefunction $\Psi(x,t) = e^{i(k_o x - \Omega_o t)}$ incident upon this modulator at $x = 0$ and consider

only the ground state. The outgoing wavefunction is a sum of plane wave states. By neglecting reflection and matching boundary conditions for all t, we find the wavefunction at $x = 0$

$$\begin{aligned}\Psi\left(0_+,t\right) &= \cos(\omega_m t+\phi_m)\Psi\left(0_-,t\right)\\ &= \frac{1}{2}\left(e^{-i[(\Omega_o+\omega_m)t+\phi_m]}+e^{-i[(\Omega_o-\omega_m)t-\phi_m]}\right).\end{aligned} \tag{2.16}$$

We next employ $\hbar k_o^2/(2m) = \Omega_o$ to determine the wavefunction beyond the modulator

$$\begin{aligned}\Psi(x,t)_{x>0} &= \frac{1}{2}e^{i[(k_o+\Delta k_m)x-(\Omega_o+\omega_m)t-\phi_m]}\\ &\quad+\frac{1}{2}e^{i[(k_o-\Delta k_m)x-(\Omega_o-\omega_m)t+\phi_m]},\end{aligned} \tag{2.17}$$

where $\Delta k_m \simeq \omega_m/v$ (valid when $\Omega_o \gg \omega_m$).

In the second case,"traditional" AM, the amplitude transmission function is $T(t) = [1+\cos(\omega_m t+\phi_m)]/2$. This produces a wavefunction at $x = 0$

$$\begin{aligned}\Psi(0_+,t) &= \frac{1+\cos(\omega_m t+\phi_m)}{2}\Psi(0_-,t)\\ &= \frac{1}{2}e^{-i\Omega_o t}+\frac{1}{4}\left(e^{-i[(\Omega_o+\omega_m)t+\phi_m]}\right.\\ &\quad\left.+e^{-i[(\Omega_o-\omega_m)t-\phi_m]}\right),\end{aligned} \tag{2.18}$$

which will propagate downstream as

$$\begin{aligned}\Psi(x,t)_{x>0} &= \frac{1}{2}e^{i[k_o x-\Omega_o t]}+\frac{1}{4}e^{i[(k_o+\Delta k_m)x-(\Omega_o+\omega_m)t-\phi_m]}\\ &\quad+\frac{1}{4}e^{i[(k_o-\Delta k_m)x-(\Omega_o-\omega_m)t+\phi_m]}.\end{aligned} \tag{2.19}$$

Equations 2.17 and 2.19 show that amplitude modulation is a beamsplitter that gen-

erates a multi-state coherence in longitudinal momentum space from a single incident state.

AM beamsplitters are not time-reversible, and no incident multi-state coherence will emerge as a single output beam. This is closely connected with their non-unitarity: a substantial fraction of the incident amplitude is absorbed by the modulator (or is transferred to an internal state which is not observed), hence it is a lossy optical element. Traditional amplitude modulation leaves 1/2 of the initial amplitude (1/4 of the initial population) unshifted in momentum, while forming two momentum sidebands, at $k_o \pm \Delta k_m$, each with 1/4 the amplitude (1/16 the initial intensity). The suppressed carrier AM scheme is the analog of double sideband suppressed carrier amplitude modulation in radio engineering, and is more efficient at putting intensity in the sidebands: with the carrier eliminated, 1/4 of the initial intensity appears in each sideband.

The fully quantum mechanical treatment of amplitude modulation presented here can be applied to any periodic modulation function $\omega_R(t)$, even if non-sinusoidal (for example to a square wave beam chopper). Fourier decomposition of such transmission functions with respect to time results in a spectrum of sidebands spaced at multiples of the modulation frequency, ω_m, implying an outgoing matter wave that has many momentum components shifted by negative and positive multiples of $\hbar\omega_m/v$.

2.2.5 Velocity Spread and Remote Quantum Rephasing

In this section, we introduce the effects of the finite velocity spread of real atomic beams on the visibility of momentum coherences created by AM beamsplitters and DSOF interferometers, demonstrating that it can wash out the time-dependent signals these devices produce. In addition, we demonstrate a remarkable feature of DSOF: its additional phase term can be adjusted to rephase the amplitude modulation of different velocity classes at a preselected downstream location.

Simple amplitude modulators, discussed in Sec. 2.2.4, create momentum sidebands by chopping a monochromatic plane wave into a series of packets. Typical supersonic atomic beams have a 10% velocity spread, which leads to a spread in the packet

lengths. This spread causes the fastest packets in the beam to get one packet length ahead of the slowest ones after traveling for about 10 packet lengths; beyond this distance, packets with intermediate speeds will completely fill in the voids initially present between the packets. In terms of momentum sidebands, this loss of visibility is the result of the variation in the momentum transfer (sideband spacing) applied by the amplitude modulator, since this momentum shift ($\hbar\Delta k_m = \hbar\omega_m/v$) is a function of the initial particle velocity.

The amplitude modulation created by DSOF is unlike the AM discussed in Sec. 2.2.4. Instead of creating AM directly at the position of the modulator which subsequently dephases downstream, DSOF can create a complex momentum superposition (undetectable at the DSOF location) which rephases to become detectable AM at a controllable downstream position—a process which we term remote quantum rephasing and which is analogous to the "time focusing" possible in a neutron resonance spin echo experiment [87]. To demonstrate the rephasing, we rewrite, from Eq. 2.14, the total phase difference between the two excited state plane wave components at a point x downstream of the DSOF

$$\phi(x,t) = \frac{\delta_1(x_2 - x_1)}{v} - \frac{(\delta_2 - \delta_1)(x - x_2)}{v} - (\omega_1 - \omega_2)t. \tag{2.20}$$

For a 10% velocity spread, the spatial part of $\phi(x,t)$ typically varies by more than 2π if either of the first two terms exceeds 20π, rendering the temporal beats caused by the $(\omega_1 - \omega_2)t$ term invisible. However, for the particular downstream location $x = x_{reph}$, where

$$x_{reph} = \frac{\delta_2 x_2 - \delta_1 x_1}{\delta_2 - \delta_1}, \tag{2.21}$$

the total spatially dependent phase (first two terms of Eq. 2.20) sum to zero *independent* of the velocity of the incident plane wave state. This position, x_{reph}, is the location at which the amplitude modulation imposed by the DSOF will rephase, producing a detectable AM signal. Hence, the DSOF acts like a virtual suppressed

carrier amplitude modulator (Sec. 2.2.4) positioned at x_{reph}.[2]

Figure 2-2 provides a graphical explanation of the location of x_{reph}. The total spatial phase difference evolved between the two interfering paths is the difference of the two hatched areas, which represent the phase differences induced inside and downstream of the DSOF respectively. At x_{reph} this phase difference is equal to zero, because these areas are opposite in sign and of equal magnitude independent of velocity. This configuration is a "white fringe" longitudinal interferometer, because the temporally oscillating fringes for different wavelengths are all in phase.

The ability of an intensity detector placed at x_{reph} to observe the rephased amplitude modulation is limited by its frequency response. However, for frequencies higher than the detector response, a heterodyne detection technique can be employed to mix the signal down to an observable frequency.

An amplitude modulator (Sec. 2.2.4) placed downstream of the DSOF at $x = x_{reph}$ (Fig. 2-2) is a suitable heterodyne device. At this downstream position, the amplitude modulation created by the modulator can heterodyne the amplitude modulation produced by the DSOF to low frequency. To calculate the excited state probability for this geometry, we propagate each component of the wavefunction downstream of the DSOF (Eq. 2.13) through the suppressed carrier amplitude modulator (Eq. 2.17). Squaring this amplitude yields, for a single velocity, an excited state probability

$$\begin{aligned}\langle P_e(\delta_1,\delta_2,v,x,t)\rangle &= \frac{1}{4}+\frac{1}{8}\cos\left[(\delta_1-\delta_2+2\omega_m)\left(\frac{x}{v}-t\right)\right.\\ &\quad\left.+\frac{\delta_2 x_2-\delta_1 x_1-2\omega_m x_m}{v}-2\phi_m\right],\end{aligned} \tag{2.22}$$

for $x > x_m$, where x_m is the modulator position, and we have used $\delta_1 - \delta_2 = \omega_1 - \omega_2$. The $\langle\rangle$ denotes a time-average over high frequencies ($> \omega_m$) which we assume are lost due to the limited frequency response of the detector. The excited state probability

[2]Note for large values of $\delta_1 - \delta_2 + 2\omega_m$ the rephasing condition is actually satisfied at a slightly different value of x_{reph}, because in this case the non-zero momentum difference downstream of x_{reph} adds some additional phase.

exhibits low frequency beats at a frequency $\omega_1 - \omega_2 + 2\omega_m$. If we select this beat frequency to be equal to zero, so that the sidebands produced by the downstream modulator overlap the sidebands previously created by the DSOF, we obtain a dc signal,

$$\langle P_e(\delta_1, \delta_2, v)\rangle = \frac{1}{4} + \frac{1}{8}\cos\left[\frac{(x_{reph} - x_m)(\delta_2 - \delta_1)}{v} - 2\phi_m\right]. \tag{2.23}$$

Equation (2.23) shows that the remote quantum rephasing of the DSOF's amplitude modulation at the position of the downstream AM region results in the recovery of the coherence lost due to the initial velocity spread.

If we include the effects of velocity averaging by integrating Eq. 2.23 over the beam's velocity distribution, a scan of x_{reph} (implemented by varying δ_1 and δ_2 while keeping their difference fixed) sweeps out damped dc fringes in P_e. These fringes look like standard SOF fringes except that they occur far from $\delta_{1,2} = 0$. The center of these "rephased" Ramsey fringes, which occurs at $x_{reph} = x_m$, provides a determination of the modulator position x_m, telling us not only that AM was applied to the beam, but *where* it was applied as well, as demonstrated by a recent experiment [68]. Varying the phase ϕ_m of the amplitude modulator results in sinusoidal modulation of P_e, demonstrating the coherent nature of the momentum superposition created by the DSOF.

2.2.6 Measuring Upstream Coherence with DSOF

We now discuss how DSOF may be employed as a tool to detect coherent superpositions of longitudinal momentum (coherences) present in the quantum state of an incident matter wave beam. To do so we consider detecting coherences produced by a suppressed carrier amplitude modulator placed *upstream* of a DSOF interferometer (in contrast to the downstream modulator location described in Sec. 2.2.5). As discussed above, the finite velocity distribution of the atomic beam causes this coherence to dephase—an intensity detector alone, if placed beyond a short distance downstream of the modulator, cannot detect it. We show that a DSOF interferometer

can reverse the effects of this velocity dephasing.

To rephase the upstream AM coherence, we again employ the heterodyne technique described in Sec. 2.2.5, which allows us to beat down high frequency coherences to either low frequency or dc. To find the wavefunction produced by this configuration, we take the AM wavefunction of Eq. 2.17 and propagate it through the DSOF interferometer (Eq. 2.13). Squaring this to obtain the probability gives a result identical to Eq. 2.23 with an important difference: x_{reph} (Eq. 2.21), formerly the downstream position at which the amplitude modulation produced by the DSOF rephased, is chosen to be equal to the location of the modulator, which is now *upstream* of the DSOF. The sign of ϕ_m is also reversed. As in Sec. 2.2.5, a scan of x_{reph} yields fringes around x_m. A set of measurements of the time-dependent signal (Eq. 2.22) for all possible values of both the rephasing position x_{reph} and the heterodyne frequency $\delta_1 - \delta_2$ can be inverted [81] to determine the density matrix of the incident beam, yielding all possible information about the quantum ensemble.

The DSOF velocity rephasing technique that we have discussed so far in Secs. 2.2.5-2.2.6 is analogous to half of a spin echo experiment [72]. In a spin echo, the coherence produced by an initial $\pi/2$ pulse is dephased by inhomogeneities in the spin ensemble being studied. A π pulse then rearranges the dephased spins so that further inhomogeneous evolution rephases them at a later time. A DSOF interferometer produces an initial ensemble which is dephased in just such a way that its inhomogeneous velocity distribution leads to a rephasing at a particular location downstream, as in the rephasing half of the spin echo. If an amplitude modulator is placed upstream of a DSOF, it acts like the first $\pi/2$ pulse in the echo, producing a transient coherence that quickly damps out. The DSOF can recognize the coherent nature of the dephased ensemble and reveal the location of the modulator, despite the fact that the transient coherence is not reconstituted as it is in a spin echo experiment. The DSOF can also play the role of a π pulse in full spin echo, altering the dephased atoms produced by an upstream amplitude modulator so that they rephase at the location of a second, downstream AM region.

2.2.7 Phase Modulation

We now provide a quantum mechanical treatment of phase modulation, another technique that can add coherent sidebands to an incident matter wave, and can therefore act as a beamsplitter in longitudinal momentum space. One can phase modulate a matter wave by transmitting it through a localized region containing a periodically varying potential U_g which creates a periodic modulation of k (according to Eq. 2.1), and thus of the wavefunction's phase at the end of the region. A Fourier transform of the downstream phase modulated wavefunction reveals the presence of coherent energy and momentum sidebands, despite the fact that the amplitude of the matter wave is unchanged. Reflection of matter waves from a vibrating mirror is another mechanism for producing phase modulation [60, 64, 65].

In a classical picture of the phase modulation process, the atom exchanges kinetic for potential energy (i.e. it climbs up or falls down a potential hill) when it enters or exits the modulation region, receiving a momentum shift which depends on the time of entrance or exit. Since U_g is time-dependent, the momentum shifts imparted at these times are unequal, producing a net change in the momentum of the atom. A periodic U_g generates a continuous classical spectrum of final momenta that approximates the discrete quantum momentum spectrum.

In this section, we first present a fully quantum mechanical treatment of a matter wave phase modulator. We next derive conditions for which phase modulation is physically observable with an intensity detector, showing that while phase modulation sidebands are unobservable if the detector is placed close to the PM beamsplitter, they can be observed if the detector is sufficiently far downstream. Finally, we suggest an experimental configuration in which phase modulation is observable in the near field, by placing the phase modulator inside a DSOF interferometer.

A plane wave $\Psi(x,t) = e^{i(k_o x - \Omega_o t)}$ will be phase modulated by passing through a region with interaction potential

$$U_g = U(x)\sin(\omega_m t), \tag{2.24}$$

where $U(x) = 0$ outside the modulation region $0 < x < l$. We postulate that the wavefunction inside this region contains energy components shifted by multiples of the modulation frequency,

$$\Psi(x,t)_{0<x<l} = \sum_{n=-\infty}^{\infty} a_n(x) e^{i[k_n x - (\Omega_o + n\omega_m)t]}, \tag{2.25}$$

where $\hbar^2 k_n^2/(2m) = \hbar(\Omega_0 + n\omega_m)$. Substituting into Schrödinger's equation with the Hamiltonian $H = -\hbar^2 \frac{\partial^2}{\partial x^2} + U_g$ and taking the kinetic energy to be the dominant energy in the problem ($\hbar\Omega_o \gg U, \hbar\omega_m$), we obtain a recursion relation

$$\frac{2\hbar k_n}{m}\frac{\partial a_n(x)}{\partial x} + \frac{U(x)}{\hbar}\left(a_{n+1}(x)e^{i(k_{n+1}-k_n)x} - a_{n-1}(x)e^{-i(k_n - k_{n-1})x}\right) = 0. \tag{2.26}$$

In the large kinetic energy limit we may take $\hbar k_n/m \simeq v$ in the first term of Eq. 2.26 and $k_n \simeq k_o + n\omega_m/v$ in the arguments of the exponentials, and write

$$\Delta k_n = k_{n+1} - k_n \simeq \Delta k_m \equiv \omega_m/v. \tag{2.27}$$

This results in the simplified expression:

$$2\frac{\partial a_n(x)}{\partial x} + \frac{U(x)}{\hbar v}\left(a_{n+1}(x)e^{i\Delta k_m x} - a_{n-1}(x)e^{-i\Delta k_m x}\right) = 0. \tag{2.28}$$

For the case of a square potential ($U(x) = U$ on the interval $[0, l]$ and zero elsewhere), Eq. 2.28 can be solved exactly. Employing the ansatz $a_n(x) = e^{-in\Delta k_m x/2}\tilde{a}_n\left[\frac{2U}{v\hbar\Delta k_m}\sin(\Delta k_m x/2)\right]$, we find that the $\tilde{a}_n$ satisfy Bessel function recursion relations [91]. Beyond the phase modulation zone, the eigensolutions are again plane wave states. Matching boundary conditions at $x = 0, l$ (and neglecting reflection as usual) we obtain the outgoing wavefunction

$$\begin{aligned}\Psi_{x>l}(x,t) &= \sum_{n=-\infty}^{\infty} e^{\frac{-in\Delta k_m l}{2}} J_n\left[\frac{2U}{\hbar\Delta k_m v}\sin\left(\frac{\Delta k_m l}{2}\right)\right] \\ &\quad \times e^{i[(k_o + n\Delta k_m)x - (\Omega_o + n\omega_m)t]},\end{aligned} \tag{2.29}$$

which agrees with the more general solution obtained by Summhammer [57] in the limit of large velocities. In this wavefunction, matter wave sidebands exist at multiples of $\hbar\omega_m$ in energy and $\hbar\omega_m/v$ in momentum. The Bessel function distribution of sideband amplitudes seen in Eq. 2.29 is also obtained for phase modulation of radio or light waves.

To explicitly demonstrate that this solution represents a pure phase modulation of the matter wave beam, we rewrite [91] Eq. 2.29 as:

$$\Psi_{x>l}(x,t) = e^{i[(k_o x - \Omega_o t) + \xi \sin(\frac{\omega_m(x-l/2)}{v} - \omega_m t)]}, \tag{2.30}$$

where $\xi = \frac{2U}{\hbar\omega_m} \sin\left(\frac{\omega_m l}{2v}\right)$. The fact that the amplitude of this wavefunction does not vary with time shows that it is not possible to detect phase modulation with a conventional intensity detector. This is true for radio waves as well—an AM receiver will not detect PM signals.

Matter waves propagate dispersively in free space, raising the possibility of detecting phase modulation with an intensity detector placed sufficiently far downstream. The "sufficient" distance is determined by the failure of the approximation in Eq. 2.27. To take higher order terms into account, we rewrite the wavevector $k_n = k_o + n\omega_m/v + \delta k_n$, where

$$\delta k_n \equiv k_n - (k_o + \frac{n\omega_m}{v}) \simeq -n^2 \frac{\hbar\omega_m^2}{2mv^3} = -n^2 \frac{2\pi}{L_{Talbot}}. \tag{2.31}$$

Here we include terms that are second order in the small parameter ω_m/Ω_o, and introduce the Talbot length

$$L_{Talbot} = 2d^2/\lambda, \tag{2.32}$$

where λ is the atomic de Broglie wavelength and $d = 2\pi v/\omega_m$ is the spatial period of the modulated beam. The Talbot length, a quantity used in transverse optics, is the distance downstream from a periodic structure at which its first near field image revival occurs [92].

In the longitudinal case, the extra relative phase accumulated over a distance

x due to the difference in wavevectors is given by $\delta k_n x$, allowing us to rewrite the wavefunction downstream of the phase modulator (Eq. 2.30) as

$$\begin{aligned}\Psi_{x>l}(x,t) &= e^{i(k_o x-\Omega_o t)}\sum_{n=-\infty}^{\infty} J_n(\xi) \\ &\quad \times e^{i\left[n\omega_m\left(\frac{(x-l/2)}{v}-t\right)-n^2\frac{2\pi x}{L_{Talbot}}\right]}.\end{aligned} \tag{2.33}$$

When $x/L_{Talbot} \ll 1$, the wavefunction is in the near field of the phase modulator, Eq. 2.33 reduces to Eq. 2.30, and the phase modulation sidebands are invisible to an intensity detector. For typical atomic beam velocities ($v \sim 1000m/s$) and for sufficiently slow modulation frequencies ($\omega_m < 2\pi \times 10^8 Hz$), $L_{Talbot} > 10m$ and this near field criterion is met both inside the PM region and for relevant distances downstream. However for slower velocities or faster modulation, L_{Talbot} can be smaller. At a distance $x \simeq L_{Talbot}/4$, the second order terms in Eq. 2.31 can no longer be neglected and the initially pure phase modulation evolves into observable amplitude modulation. The evolution of PM into AM, allowing detection in the intermediate field, can thus be described as a longitudinal Talbot effect.

Although the phase of a wavefunction is unobservable by intensity detectors, it can be studied interferometrically. Thus, PM sidebands *can* be observed in the near field, by applying phase modulation to one arm of a matter wave interferometer. The resulting time-dependent relative phase of the arms temporally modulates the interference fringes; this has been demonstrated with neutrons, using sufficiently low frequency modulation that velocity averaging was not important [63]. We also note that PM sidebands have been observed in the far field, as shown in experiments with cold neutrons [64] and pulsed cold atoms [65].

A DSOF interferometer can detect phase modulation applied to only one of the two states between two DSOF regions, as shown in Fig. 2-3, even in a regime where velocity averaging is significant and in which the two arms of the interferometer are not spatially separated. The phase modulation can be applied differentially to the two states if one of the states interacts more strongly with the modulation. For example,

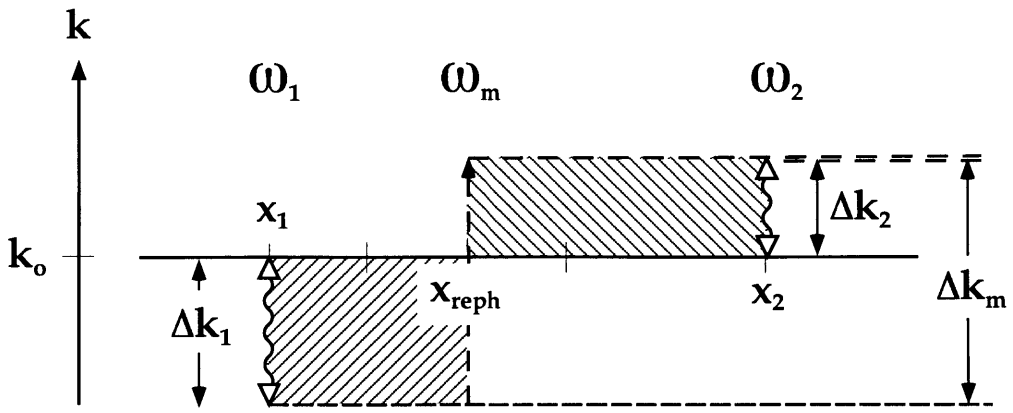

Figure 2-3: The DSOF employed to detect phase modulation applied to the excited state arm. Ground (excited) state plane wave components are shown as solid (dashed) lines. The areas of the hatched regions are proportional to the phase accumulated by atoms excited at x_1 and modulated at x_{reph} relative to those excited at x_2. The total area, and hence the differential phase, between the two momentum components is equal to zero downstream of x_2. For clarity, only one PM sideband is shown.

if the DSOF involves a superposition of $m = 0$ and $m = \pm 1$ magnetic sublevels, and phase modulation is created by varying the strength of the bias field, the $m = 0$ state (which has no linear Zeeman shift) is not modulated.

To find the detection probability for such a geometry, we propagate an initial plane wave through a DSOF interferometer whose first coil is located at x_1 (where $x_1 < 0$). The resultant coherent superposition is propagated through a PM region $0 < x < l$ which affects only the excited state component. The output of the PM region is then propagated through the second DSOF region at x_2. For modulation at frequency ω_m, a state-sensitive detector after the second DSOF region would measure,

$$\begin{aligned}
\langle P_e(\delta_1, \delta_2, v, x, t)\rangle &= \frac{1}{2}\left\{1 + \cos\left[\frac{\delta_1}{v}(x - x_1) - \frac{\delta_2}{v}(x - x_2) - (\omega_1 - \omega_2)\,t \right.\right. \\
&\qquad \left.\left. + \xi \sin\left(\frac{\omega_m(x - l/2)}{v} - \omega_m t\right)\right]\right\} \\
&= \frac{1}{2}\left\{1 + \left\langle \sum_{n=-\infty}^{\infty} J_n(\xi) \cos\left[(\delta_1 - \delta_2 + n\omega_m)\left(\frac{x}{v} - t\right)\right.\right.\right. \\
&\qquad \left.\left.\left. + \frac{\left(\delta_2 x_2 - \delta_1 x_1 - n\omega_m \frac{l}{2}\right)}{v}\right]\right\rangle\right\} \qquad (2.34)
\end{aligned}$$

where $\delta_1 - \delta_2 = \omega_1 - \omega_2$, and $\langle\rangle$ denotes a time-average over high frequencies. If, for some $n = N$, we select $\delta_1 - \delta_2 + N\omega_m = 0$, we can heterodyne a particular sideband down to dc and rewrite Eq. 2.34 as

$$\langle P_e(\delta_1, \delta_2, v)\rangle \simeq \frac{1}{2}\left\{1 + J_N(\xi)\cos\left[\frac{x_{reph} - \frac{l}{2}}{v}(\delta_2 - \delta_1)\right]\right\}, \tag{2.35}$$

where x_{reph} is given by Eq. 2.21.

As in the case of AM detection (Sec. 2.2.5) the DSOF can be used to overcome the effects of velocity spreading by setting $x_{reph} = l/2$ (a result which suggests that the phase modulator can be treated as a virtual amplitude modulator located in the middle of the PM region). In this case, however, the effects of velocity averaging will still be felt in the argument of the Bessel functions, since ξ is a function of velocity. The relative weight of these sidebands shows the Bessel function distribution predicted by Eq. 2.29.

2.2.8 Conclusion

We have presented in this paper a fully quantum mechanical treatment of time-dependent potentials applied to atomic beams in which we explicitly include the quantum mechanical wave representing the particles' longitudinal motion. Using this treatment we have developed a novel view of the classic single oscillatory field resonance experiment which treats RF and laser fields on an equal footing, and shows that both generate quantum entanglement of internal and translational states. We have also discussed both amplitude and phase modulators for matter waves that generate coherent, longitudinal momentum space superpositions.

We have proposed the use of differentially detuned, radiofrequency separated oscillatory fields (DSOF) as a technique to manipulate longitudinal momentum. We have shown that DSOF can interfere different initial momentum components, revealing momentum coherences present in the beam. We have also described a novel momentum rephasing technique, in which DSOF can be employed to create or detect modulation which would ordinarily be dephased by the finite velocity distribution of

the atomic beam.

The longitudinal atom optics methods we have developed in this paper have a variety of future applications. In general, they are natural extensions of the many successful techniques of transverse atom optics, allowing greater control of the quantum state of particle motion. For example, the ability of DSOF to create virtual amplitude modulation may find use in beam preparation for future experiments requiring bright, but extremely short, pulses of atoms.

Sequences of longitudinal atom optical elements (resonance regions, and AM or PM beamsplitters), when combined with novel atom sources such as slow atoms or Bose-Einstein condensates, may allow the creation of useful devices, such as atomic resonators or new longitudinal interferometers. Finally, the DSOF longitudinal interferometer can determine density matrix of an incident matter wave [81], potentially settling the controversial question [82, 83, 84, 85] of the correct quantum description of a thermal or supersonic beam.

Acknowledgments

We thank J. Schmiedmayer for helpful conversations and D. Kleppner, W. Ketterle, D. Stamper-Kurn, W. Smith, T. Roberts, J. Lerner, and S. Gupta for helpful comments on the manuscript. This work was supported by Army Research Office contracts DAAH04-94-G-0170 and DAAH04-95-1-0533, Office of Naval Research contracts N00014-89-J-1207 and N000014-96-1-0432, Joint Services Electronics Program contract DAAH04-95-1-0038, and National Science Foundation contract PHY-95-14795. B. Rohwedder acknowledges the support of FONDECYT Grant No. 2950068.

2.2.9 Appendix: Classical Derivation of Rephased Fringes

Much of the quantum treatment of center of mass motion given in this paper has been conducted under the approximation made for Δk in Eq. 2.8, which ignores terms quadratic in δ/Ω_o. This approximation linearizes the relationship between Δk, the momentum shift induced by a detuned transition, and δ, its detuning. The validity

of this approximation is limited to within a downstream distance given by the Talbot length of Eq. 2.32, after which the integrated phase error $(\Delta k - \delta/v)x$ caused by neglect of the quadratic terms becomes appreciable. As discussed in Sec. 2.2.7, for typical molecular beam experiments $L_{Talbot} \gg 10m$.

For experiments in which all distances are shorter than the Talbot length, this approximation is equivalent to taking a classical position and velocity for the atom while treating its internal evolution quantum mechanically. In this picture, the amplitude and phase of any applied oscillatory field(s), evaluated at the classical position $x = \frac{\hbar k}{m}(t - t_i)$, determine whether a particular atom is excited (without any accompanying change in momentum) or remains in the ground state. This is the usual approximation made in the standard treatment of molecular beam resonance [45]. The equivalence between these two pictures stems from the fact that Eq. 2.8 forces the additional waves created by any oscillatory fields to have the same group velocity v as the initial wave.

To demonstrate this equivalence, we present an analysis of the rephasing phenomenon using the conventional resonance picture: assume that a particle is emitted from a source at position x_0 with classical velocity v at time t_0. The transmission probability through an amplitude modulator at position x_m is just the square of amplitude transmission function $T(t)$ used previously in Eq. 2.15:

$$\begin{aligned} P_m &= \cos^2(\omega_m t_m + \phi_m) \\ &= \frac{1}{2}\left\{1 + \cos\left[2\omega_m(t_d - \frac{x_d - x_m}{v}) + 2\phi_m\right]\right\}, \end{aligned} \tag{2.36}$$

where (x_m, t_m) and (x_d, t_d) are the positions and times of arrival at the modulator and detector respectively.

The probability of detection in the excited state after passing through a DSOF region was calculated in Eq. 2.14. For the present discussion, we replace x and t with x_d and t_d, and explicitly include the velocity dependence:

$$P_e \simeq \frac{1}{2}\left\{1+\cos\left[\frac{\delta_1}{v}(x_2-x_1) - \frac{\delta_2-\delta_1}{v}(x_d-x_2) - (\omega_1-\omega_2)t_d\right]\right\}. \quad (2.37)$$

To illustrate the classical origin of the time dependence produced by DSOF, we employ the relationship, $x = x_0 + v(t-t_0)$, and the fact that $\delta_1 - \delta_2 = \omega_1 - \omega_2$, to rewrite Eq. 2.37 as:

$$\begin{aligned} P_e &\simeq \frac{1}{2}\left\{1+\cos\left[\frac{\delta_1}{v}(x_2-x_1) + (\omega_1-\omega_2)\left(\frac{x_d-x_2}{v} - t_d\right)\right]\right\} \\ &\simeq \frac{1}{2}\left\{1+\cos\left[\frac{\delta_1}{v}(x_2-x_1) - (\omega_1-\omega_2)t_2\right]\right\}. \end{aligned} \quad (2.38)$$

In the standard Ramsey picture, the phase difference between the two oscillatory fields determines the probability of a particle exiting in the excited state. Equation 2.38 shows that this phase, $(\omega_1 - \omega_2)\, t_2$, is now a periodic function of the particle's arrival time at the second coil.

To find the total probability of detecting the particle in the excited state, we multiply the AM transmission probability by the DSOF excitation probability, keeping only terms which oscillate slowly in time (see discussion in Sec. 2.2.5) to obtain a signal identical to equation Eq. 2.22:

$$\begin{aligned} P_{tot} &\simeq \left\langle \frac{1}{4}\left\{1+\cos\left[\frac{\delta_1}{v}(x_2-x_1) - \frac{\delta_2-\delta_1}{v}(x_d-x_2) - (\omega_1-\omega_2)t_d\right]\right\} \right. \\ &\quad \left. \times \left\{1+\cos\left[2\omega_m\left(t_d - \frac{x_d-x_m}{v}\right) + 2\phi_m\right]\right\}\right\rangle \\ &\simeq \frac{1}{4}\left\{1+\frac{1}{2}\cos\left((\delta_1-\delta_2+2\omega_m)\left(\frac{x}{v}-t\right) + \frac{\delta_2 x_2 - \delta_1 x_1 - 2\omega_m x_m}{v} - 2\phi_m\right)\right\}. \end{aligned} \quad (2.39)$$

While the equivalence of Eq. 2.22 and Eq. 2.39 demonstrates that the quantum and classical center of mass treatments lead to identical results for distances much less than the Talbot length, the plane wave analysis we have adopted in this paper has several advantages. It extends correctly to the case of slow atoms, where the classical longitudinal velocity picture fails. Perhaps more important is the intuition our analysis provides when considering extensions to the standard techniques of atomic beam resonance. The DSOF rephasing of coherences created by up- or downstream amplitude modulators, for example, has an appealingly intuitive explanation in terms of the cancellation of spatial phases (see Sec. 2.2.5). Our treatment of amplitude and phase modulation (which may also be described classically) as longitudinal momentum beamsplitters suggests new roles for these devices as well.

2.3 More on the Semiclassical Approximation

Our derivations of LAO in the previous section employ the approximation

$$\frac{\hbar\Delta\omega}{\hbar\Omega_o} \ll 1, \tag{2.40}$$

where $\hbar\Delta\omega$ is the energy shift applied by the LAO element (resonant oscillatory field, AM or PM region) and $\hbar\Omega_o$ is the total (overwhelmingly kinetic) energy of the incident beam. This approximation, which allows us to simplify the Schrödinger equation (by neglecting second derivative terms and terms proportional to $\frac{\Delta k}{k_o}$ in the amplitude), to write Eqs. 2.6, 2.7, 2.26, and to linearize the relationship between the momentum shift Δk and the phase in Eqs. 2.8, 2.27, is equivalent to the semiclassical or JWKB approximation, which is valid if the wavefunction changes only slowly on the scale of the applied potentials [93].

Since the energy shifts we apply in our experiments are $\sim$ 2 MHz at most and the mean energy of our Na atomic beam is about 3.4×10^7 MHz, the inequality in Eq. 2.40 is well satisfied in all our LAO elements. However, as we showed in Sec. 2.2.7 higher order terms in the expression for Δk, while unimportant over the short distance which the wave traverses inside an LAO element, can have an effect if the beam is allowed to propagate a longer distance downstream.

In longitudinal atom optics, as in transverse light optics, the Talbot length L_{Talbot} (Eq. 2.32) sets the length scale for near field optical effects [92], and is useful in explaining how higher order terms in the expansion of Δk alter the wavefunction. At distances much less than L_{Talbot}, the atoms follow ray-like, classical trajectories, just like light rays which form a geometric shadow after passing through an opening much larger than their wavelength.

For the case of longer distances, if monochromatic radiation is incident on a periodic structure, exact replica images of the structure will appear at downstream distances that are integer multiples of $\frac{L_{Talbot}}{n}$ for integer n. We can qualitatively understand this result in both the longitudinal and transverse case by determining $\frac{T_{Talbot}}{4} = \frac{L_{Talbot}}{4v}$, the time it takes for the ± 1 diffracted orders produced by a transverse

amplitude grating (or equivalently the ± 1 sidebands produced by a phase or amplitude modulated atomic beam) to overlap as they propagate downstream, producing near field interference effects (see Fig. 2-4). The relative velocities of the two orders or sidebands is

$$\Delta v = 2\frac{\hbar}{m}\frac{2\pi}{d}, \tag{2.41}$$

where d is the grating period in the transverse case and $d = v\frac{2\pi}{\omega_m}$, the spatial period of the modulated beam, in the longitudinal case. As the two orders/sidebands must travel a distance d in order to overlap, the time it takes to do so is

$$\begin{aligned} \frac{T_{Talbot}}{4} &= \frac{d}{\Delta v} \\ &= \frac{md^2}{4\pi\hbar}, \end{aligned} \tag{2.42}$$

leading to a Talbot length $L_{Talbot} = vT_{Talbot}$ in agreement with Eq. 2.32.

As a demonstration of the longitudinal Talbot effect, we calculate the absolute value squared of Eq. 2.33, the atomic probability far ($\sim L_{Talbot}$) downstream of a phase modulation region

$$P_{Talbot} = \sum_{n=-\infty}^{\infty} e^{in(\theta+\pi/2)} J_n\left(2\xi \sin[n\phi]\right), \tag{2.43}$$

where $\theta = \omega_m\left[\frac{(x-l/2)}{v} - t\right]$ is the phase describing the time- and space-dependence of any visible amplitude modulation, and $\phi = \frac{2\pi x}{L_{Talbot}}$.

We can employ the coefficients $J_n\left(2\xi \sin[n\phi]\right)$ to determine the modulation index m of the amplitude modulation in the beam at each frequency $n\omega_m$. Figure 2-5 displays m as a function of ϕ for several values of n and ξ, the strength of the applied phase modulation. As predicted, phase modulation evolves into observable amplitude modulation on the scale of L_{Talbot}. Figure 2-5c demonstrates that strong phase modulation, as well as observation of high frequency sidebands, leads to faster visibility of the AM.

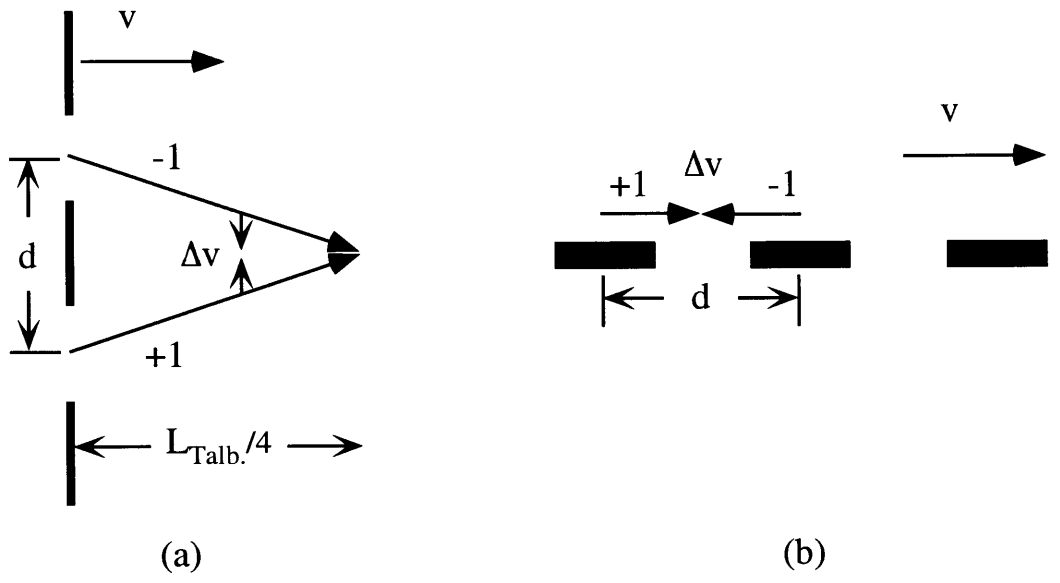

Figure 2-4: Transverse (a) and longitudinal (b) Talbot length. In the transverse case the ± 1 diffracted orders have a relative velocity $\Delta v = 2\frac{\hbar}{m}\frac{2\pi}{d}$, and must travel a distance $\frac{L_{Talbot}}{4}$ to overlap and interfere. In the longitudinal case the ± 1 sidebands overlap in a time $\frac{T_{Talbot}}{4} = \frac{d}{\Delta v}$, yielding an identical result for $\frac{L_{Talbot}}{4}$, the downstream distance the beam must propagate for near field interference to be observed.

The Talbot length is on the order of 3000 m for the LAO experiments we describe in this thesis, preventing our observation of the longitudinal Talbot effect. However, for $\xi = 2\pi$, $v = 700$ m/sec, and $\omega_m = 2\pi \times 10$ MHz, measurable AM is visible after only 1.5 m. These parameters might be achievable for an experiment in which a rapidly modulated, narrowly focused ($\sim$ 20 micron waist) off-resonant laser is used to phase modulate the atomic beam, allowing observation of this phenomenon.

For our current experiments, in which the atoms travel distances $\ll L_{Talbot}$ and their trajectories may be treated classically, the internal state evolution nevertheless remains entirely quantum mechanical. If the internal state evolution is treated in terms of quantum amplitudes, the result of the near field approximation is that the total transmission probability for a plane wave propagated through a succession of LAO elements is the product of the transmission probability through each individual element.

For the experimentally realistic case of a continuous momentum distribution incident on an LAO element, the wavevector spread σ_k may have an additional role in

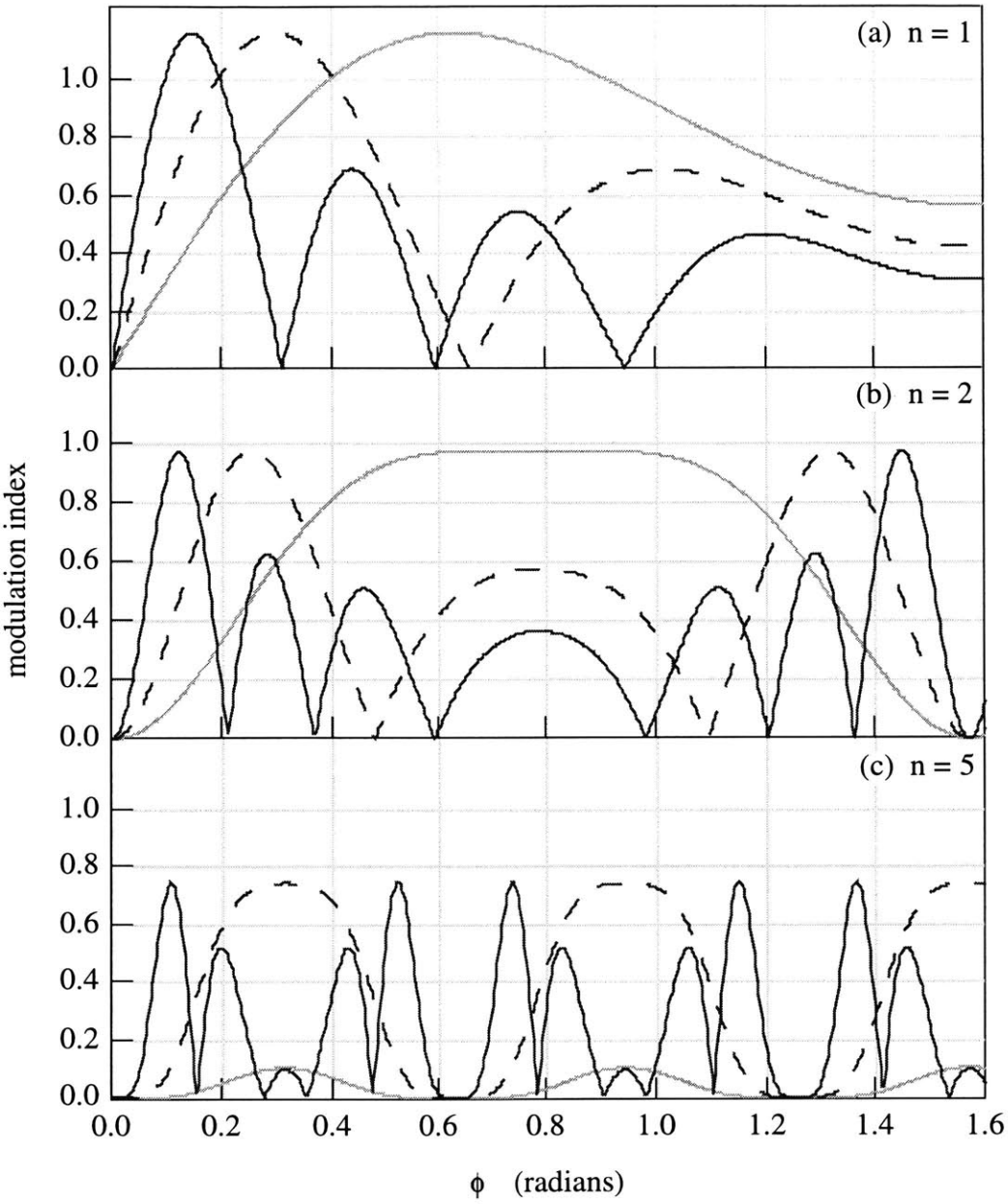

Figure 2-5: Amplitude modulation index (m) for $n = 1, 2, 5$ (i.e. signals with time-dependence at ω_m, $2\omega_m$, $5\omega_m$). The lower axis represents the distance downstream of the PM region in units of $\frac{2\pi}{L_{Talbot}}$. Three different "strengths" of phase modulation are shown: $\xi = \frac{\pi}{2}$ (light line), $\xi = \pi$ (dashed line), $\xi = 2\pi$ (dark line). (Note that, despite the fact that $m > 1$ in (a), $P_{Talbot} \leq 1$ at all times as required by conservation of probability. In all cases where $m > 1$,the presence of other time-dependent sidebands prevents $P_{Talbot} > 1$.)

determining whether the atomic trajectory has quantum or classical behavior. For such beams, non-classical longitudinal motion can be expected when $\Delta k > \sigma_k$ [50, 94]. However, the large momentum width of our atomic beam relative to the momentum shift which our LAO elements can impart ($\frac{\Delta k}{\sigma_k} \ll 1$) have thus far prevented us from exploring this regime.

Several experiments by other groups employ matter wave beams with small kinetic energies and narrow initial energy distributions, and are able to demonstrate interesting quantum effects. Felber *et al.* investigated the quantum/classical boundary in an experiment in which amplitude and phase modulation were applied to an incident neutron beam reflected at grazing incidence from a vibrating neutron mirror. Similar experiments measured phase modulation [65] and temporal diffraction and interference [66] of cold atoms reflected from a modulated evanescent light wave.

Chapter 3

Measuring the Density Matrix with DSOF

This chapter provides a theoretical discussion of the density matrix of an atomic beam in the longitudinal center of mass energy/momentum basis, paying particular attention to the role of the off-diagonal elements, which contain information about coherent superpositions of energy states. A description of our DSOF deconvolution scheme, which can be used to measure the density matrix of a nearly diagonal atomic beam, is presented, along with a semiclassical picture of both the density matrix and the deconvolution method.

3.1 The Density Matrix

Coherently prepared quantum systems are adequately described by a wavefunction, which contains information about coherent superpositions of basis states. However, a complete description of a quantum ensemble of individual particles requires a way to include the effects of incoherent, or purely statistical sums of various states. The density matrix (as well as the related Wigner function [95]), describes both coherent superpositions and incoherent averages, providing the most complete possible description of a quantum system [29, 31].

We represent the density matrix describing a freely propagating atomic beam in

the kinetic energy basis $\hbar\Omega = \frac{(\hbar k)^2}{2m}$ and write the wavefunction as

$$|\Psi\rangle = \int d\Omega\, a(\Omega)\, |\Omega\rangle\,, \tag{3.1}$$

where $a(\Omega)$ is the amplitude associated with each energy eigenstate $|\Omega\rangle$ of the free particle Hamiltonian at some initial time t_o.

The density operator can then be constructed from the wavefunction

$$\begin{aligned} \widehat{\rho} &= \overline{|\Psi\rangle\langle\Psi|} \\ &= \int\int d\Omega'\, d\Omega''\, \overline{a(\Omega')a^*(\Omega'')}\, |\Omega'\rangle\langle\Omega''|\,, \end{aligned} \tag{3.2}$$

where the overbar denotes an ensemble average over all possible initial preparations of the atoms in the beam. The density matrix is this basis is then [85]

$$\begin{aligned} \rho(\Omega', \Omega'') &= \langle\Omega'|\,\widehat{\rho}\,|\Omega''\rangle \\ &= \overline{a(\Omega')a^*(\Omega'')}. \end{aligned} \tag{3.3}$$

Equation 3.3 shows that the density matrix is Hermitian ($\rho(\Omega', \Omega'') = \rho^*(\Omega'', \Omega')$).

The density matrix can be employed to determine the outcome of measurements of observables of the system, since $\mathrm{tr}(\widehat{\rho}\widehat{A})$ is the expectation value of the operator $\widehat{A}$ for the ensemble. The density matrix also has a simple physical interpretation: the diagonal elements $\rho(\Omega', \Omega')$ correspond to the probability of measuring an atom with energy Ω'. The off-diagonal matrix elements $\rho(\Omega', \Omega'')$ measure the presence of coherences between two different energy components.

Employing the Schrödinger equation for the time evolution of the basis states and the Hamiltonian $H = \hbar\Omega\,|\Omega\rangle\langle\Omega|$, we can write the time-dependent form of the density matrix [31]

$$\rho(\Omega', \Omega'', t) = \rho_o(\Omega', \Omega' + \Omega_{coh})e^{i\Omega_{coh}(t-t_o)}, \tag{3.4}$$

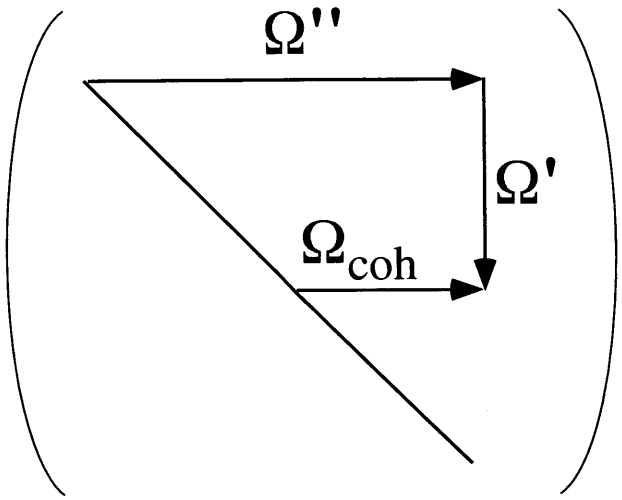

Figure 3-1: Coordinates for describing location of density matrix elements. Ω' determines location parallel to the diagonal of the density matrix. $\Omega_{coh} = \Omega'' - \Omega'$ is the distance to the right of the diagonal.

where $\rho_o = \rho(t = t_o)$ and $\Omega_{coh} \equiv \Omega'' - \Omega'$.

The quantities Ω', Ω_{coh} employed in Eq. 3.4 are a useful way to express the density matrix, since they simplify the time-dependence of the off-diagonal elements. The coordinate Ω' governs translation parallel to the diagonal of the density matrix, while Ω_{coh} denotes the distance away from the diagonal (see Fig. 3-1).

The off-diagonal elements (ODEs) of the energy/momentum density matrix determine the coherence structure of the ensemble. If all ODEs are zero, then ρ is "diagonal" and it possesses no correlations between different energy components. This absence of correlations means that no physically observable wavepackets can be measured in the beam, since these require the presence of definite phase relationships between the different plane wave components which compose the wavepacket.

The subject of longitudinal correlations in matter wave beams has attracted substantial theoretical [96, 97] and experimental interest. In an early experiment, Werner *et al.* [82] measured the contrast reduction of interference fringes in a transverse separated beam neutron interferometer as a function of an increasing path length in one arm. This contrast reduction was attributed [82, 83] to the lessening of spatial overlap of the shifted and unshifted neutron wavepackets, and hence as a measurement of their coherence length.

However, this interpretation was quickly challenged by Comsa [84], who showed that no conclusion about the wavepacket coherence length could be drawn from Werner's experiment, because the contrast loss could be equally well explained by a beam consisting of an incoherent sum of plane wave components. Comsa's choice of a plane wave basis leads immediately to a diagonal density matrix, possessing no correlations [60, 69]. While Werner's initial choice of a wavepacket basis was suggestive of the presence of momentum correlations, a correct treatment of the ensemble average[1] over emission times of the packets in the beam (necessary for his steady state experiment) also leads to a diagonal density matrix. Thus, Werner's experiment is incapable of observing the density matrix off-diagonal structure.

The time-dependence of the ODEs (Eq. 3.4) necessitates a time-dependent technique to study them. In fact, while it has been shown [85] that time-independent experiments (such as Werner's static interferometer) can only measure diagonal density matrix elements, time-dependent measurements *can* study ODEs, and hence determine the entire density matrix.

A number of time-dependent schemes have been suggested for measuring correlations in or the density matrix of a matter wave beam. One proposal employs reflection of cold neutrons from a vibrating surface [60], while several others use measurements of the spatial probability distributions $P(x)$ while rotating the ensemble in phase space, employing a tomographic reconstruction algorithm to recover the Wigner function (which is related to the density matrix via a single Fourier transform) [94, 98]. We chose a third technique, which employs a DSOF interferometer (Sec. 2.2.3) and a double Fourier transform to determine the density matrix. This deconvolution technique is described in Sec. 3.2 and in Appendix A.

Our group's first demonstration of the DSOF interferometer [68, 71] can be reinterpreted as a partial measurement of a density matrix produced by amplitude

[1]The destruction of off-diagonal matrix elements by the ensemble average over initial times can be seen by treating Eq. 3.4 as the density matrix for a *single* coherent wavepacket possessing ODEs. In this case, to form the final density matrix we must average together various ρ's with different t_o's a process which leads to a total $\rho(\Omega', \Omega' + \Omega_{coh}) = 0$ for $\Omega_{coh} \neq 0$.

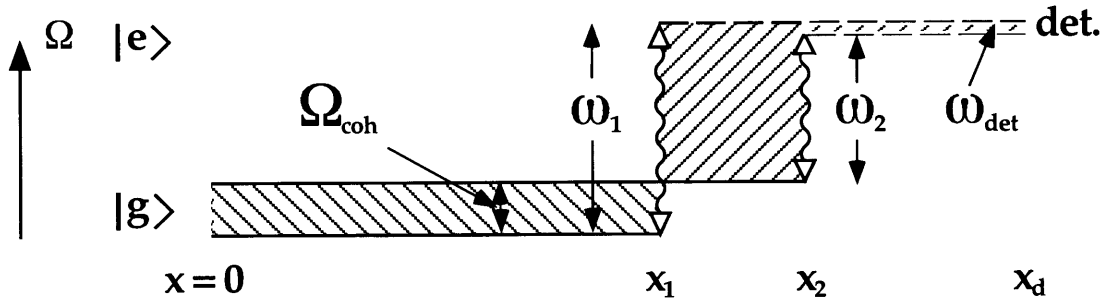

Figure 3-2: DSOF interferometer employed to detect off-diagonal density matrix elements. Two initially coherent ground state (solid line) plane wave components with frequencies differing by Ω_{coh} are driven to the excited state (dashed line) by oscillatory field regions of frequency $\omega_{1,2}$ at positions $x_{1,2}$ respectively, allowing study of their relative phase by a time-sensitive detector at x_d. This process can overlap the two incident components, causing them to interfere (creating a time-dependent signal at ω_{det} and allowing their relative amplitudes and phases to be measured. The rephasing condition, where atoms of all velocities create time-dependent fringes in phase, occurs when the two hatched areas are equal.

modulation of our atomic beam.[2] In a second experiment (see Ch. 5) we employed the DSOF to search for off-diagonal matrix elements created by our supersonic atom source. Since our search found no non-zero off-diagonal matrix elements, our measurement of the energy distribution then completely determined this simple density matrix. Finally, we used the DSOF to measure the complete structure of a novel density matrix with complicated behavior both along and off the diagonal, which we produced by placing two amplitude modulators in our beam path (Ch. 6).

3.2 DSOF Deconvolution Scheme

A derivation of our DSOF density matrix deconvolution scheme is developed in a paper by our group, "Determining the Density Matrix of a Molecular Beam Using a Longitudinal Matter Wave Interferometer" [81], which is included as Appendix A of this thesis. The key elements of this derivation are presented here.

To illustrate our deconvolution scheme, we propagate the density matrix of Eq.

[2]This demonstration did not constitute a complete measurement because only one value of Ω_{coh} was studied.

3.4, which contains plane wave components with energy difference $\hbar\Omega_{coh}$ in the ground state, through the DSOF interferometer [99] (Sec. 2.2.3). Applying $\frac{\pi}{2}$ pulses at the DSOF regions and assuming a nearly diagonal density matrix ($\Omega_{coh} \ll \Omega'$), we find that this geometry (Fig. 3-2) leads to an excited state probability

$$P_e(\delta,\tilde{\delta},t) = \int d\Omega'\, d\Omega'' \left[\rho_o(\Omega',\Omega'')e^{i(\Omega'-\Omega'')[\frac{x_d}{v'}-t]}\right] \times \frac{1}{2}\left[1+\cos\left(\frac{\tilde{\delta}L}{v'}+\frac{\delta x_d}{v'}-\delta t\right)\right], \tag{3.5}$$

at x_d, the position of the atom detector, where we have taken $t_o = 0$ and defined the differential detuning

$$\begin{aligned} \delta &\equiv \omega_1 - \omega_2 \\ &= \delta_1 - \delta_2, \end{aligned} \tag{3.6}$$

and the scaled detuning

$$\tilde{\delta} \equiv \frac{\delta_2 x_2 - \delta_1 x_1}{x_2 - x_1}. \tag{3.7}$$

As shown in Fig. 3-2, the DSOF causes the Ω' frequency component (excited by ω_1) and the $\Omega'' = \Omega' + \Omega_{coh}$ component (excited by ω_2) to interfere, producing a time-dependent beat at the detector with frequency $\omega_{det} = \delta - \Omega_{coh}$. The presence of this time-dependent signal reveals the existence of non-zero off-diagonal matrix elements. In addition, the phase of this time-dependent signal contains information about the relative phase between the two interfering plane wave components.

The detected signal can be rewritten in the form

$$\begin{aligned} P_e(\delta,\tilde{\delta},x_d,t) &= A(x_d,\Omega',\Omega'',t) \\ &+ \frac{1}{4}\int d\Omega'\, d\Omega'' \rho_o(\Omega',\Omega'') e^{i\left[\frac{[(\Omega'-\Omega'')-\delta]x_d-\tilde{\delta}L}{v'}-(\Omega'-\Omega''-\delta)t\right]} \end{aligned} \tag{3.8}$$

$$+ \quad \frac{1}{4}\int d\Omega'\, d\Omega'' \rho_o(\Omega', \Omega'') e^{i\left[\frac{[(\Omega'-\Omega'')+\delta]x_d+\tilde{\delta}L}{v'} - (\Omega'-\Omega''+\delta)t\right]},$$

where $v' = \sqrt{2\hbar\Omega'/m}$ is the velocity, and $A(\Omega', \Omega'', x_d, t)$ is defined in Appendix A. As the $e^{-i(\Omega'-\Omega''\pm\delta)t}$ terms in Eq. 3.8 show, the DSOF acts as a heterodyne device, with δ as its local oscillator frequency, which mixes down high frequency oscillatory signals caused by the presence of ODEs (at frequency $\Omega_{coh} = \Omega'' - \Omega'$) to a low frequency $(\Omega' - \Omega'' \pm \delta)$, within the frequency response range of our slow atom detector. Fourier transforming Eq. 3.8, with respect to time yields

$$\begin{aligned}\tilde{P}_e(\delta, \tilde{\delta}, \omega_{det}) &= \tilde{A}(\Omega', \Omega'', x_d, \omega_{det}) + \frac{\pi}{2}\int d\Omega' \rho_o(\Omega', \Omega' - \omega_{det} - \delta) e^{i\left[\frac{\omega_{det}x_d+\tilde{\delta}L}{v'}\right]} \\ &+ \frac{\pi}{2}\int d\Omega' \rho_o(\Omega', \Omega' - \omega_{det} + \delta) e^{i\left[\frac{\omega_{det}x_d+\tilde{\delta}L}{v'}\right]}, \qquad (3.9)\end{aligned}$$

where ω_{det} (which may be negative) is the transform variable conjugate to t. Equation 3.9 demonstrates that $\tilde{P}_e$, the time Fourier transform of the DSOF signal, is sensitive to ODE's over a range $\Omega_{coh} = \delta \pm \omega_{max}$, where ω_{max} is the maximum detector response frequency ($\sim 2\pi \times 3$ kHz for our atom detector).

The sensitivity of the observed signal to a range of Ω_{coh} means that the full bandwidth of our atom detector can be used to study the density matrix. In principle, we could efficiently study the entire off-diagonal range by acquiring time-dependent data[3] while taking steps of $\delta \simeq \omega_{max}$. However, if we take smaller steps in δ, each off-diagonal stripe of the density matrix is observed multiple times, a technique we employ in Ch. 5 to increase the sensitivity of our search for ODEs produced by our atom source. Taking the opposite extreme, if we choose to measure only the dc component of the DSOF signal ($\omega_{det} = 0$) the entire density matrix can still be determined (Ch. 6).

We can determine the density matrix by performing a final Fourier transform, this time with respect to $\tilde{\delta}$ [81], obtaining

[3]The variable $\tilde{\delta}$ must be scanned as well to provide Ω' information.

$$\rho\left(\Omega', \Omega' - \omega_{det} + \delta\right) = \frac{L}{2\pi^2}\left(\frac{m}{2\hbar}\right)^{\frac{1}{2}} \frac{e^{-i\omega_{det}\sqrt{\frac{mx_d^2}{2\hbar\Omega'}}}}{\Omega'^{3/2}} \int d\tilde{\delta}\tilde{P}_e\left(\delta, \tilde{\delta}, \omega_{det}\right) e^{-i\tilde{\delta}\sqrt{\frac{mL^2}{2\hbar\Omega'}}}. \quad (3.10)$$

The density matrix deconvolution equation (Eq. 3.10) only yields the exact density matrix if a sufficient range of δ, $\tilde{\delta}$ can be observed, and data collected for infinitely long times. In a realistic experiment, acquisition time is finite and only a subset of δ, $\tilde{\delta}$ can be reached because of the limited widths of the single coil resonance lines (Rabi pedestal [71]) of the individual DSOF regions. These restrictions limit the resolution with which the density matrix can be measured.

The resolution in Ω_{coh} is given [100] by the resolution in ω_{det}, which in turn depends on ΔT, the length of time that data is acquired for a given δ value

$$\Delta\Omega_{coh} = \frac{\pi}{\Delta T}. \quad (3.11)$$

To understand how the finite range in $\tilde{\delta}$ limits density matrix the resolution, we employ the fact that $\tilde{\delta}$ is the Fourier transform conjugate variable of the parameter $\tau = \frac{L}{v'}$. Here τ is the transit time of an atom with a particular velocity between the two DSOF coils, which in turn determines Ω', the coordinate parallel to the diagonal of the density matrix. The resolution in Ω' for a narrow energy width beam is approximately

$$\begin{aligned} \Delta\Omega' &\simeq 2\Omega'_o \frac{\Delta\tau}{\tau_o} \\ &\simeq 2\pi \frac{\Omega'_o}{\Delta\tilde{\delta}} \left(\frac{mL^2}{2\hbar\Omega'_o}\right)^{-\frac{1}{2}}, \end{aligned} \quad (3.12)$$

where $\hbar\Omega'_o$ is the mean energy, τ_o the mean transit time, and $\Delta\tilde{\delta}$ the range of $\tilde{\delta}$ for which data is available.

The effect of the finite $\tilde{\delta}$ range on the measurement of the density matrix of an amplitude modulated beam can also be considered in terms of the rephased Ramsey

fringes produced by the AM and DSOF (discussed in Sec. 2.2.5). To measure the density matrix, $\tilde{\delta}$ must be scanned over a range which includes these rephased fringes, which appear centered around:

$$\tilde{\delta}_{reph} \simeq (\Omega_{coh} - \delta)\frac{(x_d - x_o)}{L} - \delta\frac{x_o}{L}, \tag{3.13}$$

where x_o is the location of the source of the AM, and $\tilde{\delta}_{reph} = \frac{-\delta x_{reph}}{L}$ (see Eq. 2.21). If the $\tilde{\delta}$ range is not sufficient to measure the presence of these fringes, the density matrix cannot be observed.

The choice of the origin of the coordinate system, which in turn defines the DSOF coil distances $x_{1,2}$, has an effect on the form of the density matrix produced by amplitude modulation. If we choose our coordinate system for the DSOF such that $x = 0$ at the position of the modulator (i.e. $x_o = 0$), the density matrix has its simplest possible numerical form. However, if the position of the AM is instead at $x_o \neq 0$, the density matrix off-diagonal elements have a dependence $\rho_o \times e^{i\frac{\Omega_{coh}x_o}{v'}}$. These high frequency phase oscillations require a longer range in $\tilde{\delta}$ to achieve the resolution in Ω' necessary to measure the the density matrix. It is important to note that this shift in the phase of the ODEs (which results purely from a shift in the origin of the coordinate system) does not affect any physically measurable observable: the rephased fringes always appear at the same positions in the physical variables $\omega_{1,2}$.

3.3 Semiclassical Interpretation of the Deconvolution Scheme

The density matrix deconvolution method presented in Sec. 3.2 relies on a quantum mechanical treatment of the center of mass motion. However, the semiclassical approximation which applies to our fast atomic beam leads to a classical interpretation of both the density matrix and the deconvolution scheme.

We can demonstrate this alternative picture by re-examining the excited state detection probability (Eq. 3.5) measured after an atomic beam, prepared with some

arbitrary density matrix $\rho(\Omega', \Omega'')$, is passed through the DSOF interferometer. We can employ the hermiticity of the density matrix and a change of variables to rewrite Eq. 3.5 as[4]

$$P_e(\delta, \tilde{\delta}, t) = A(\Omega', \Omega'', x_d, t) + \int_{-\infty}^{\infty} d\Omega' \int_{-\Omega'}^{0} d\Omega_{coh} \, |\rho(\Omega', \Omega' + \Omega_{coh})| \times \cos\left(\Omega_{coh}\left[\frac{x_d}{v'} - t\right] - \phi(\Omega', \Omega' + \Omega_{coh})\right) \times \cos\left(\frac{\tilde{\delta}L}{v'} + \delta\left[\frac{x_d}{v'} - t\right]\right) \quad (3.14)$$

where we have written $\rho(\Omega', \Omega' + \Omega_{coh}) = |\rho(\Omega', \Omega' + \Omega_{coh})| \, e^{i\phi(\Omega', \Omega' + \Omega_{coh})}$. Equation 3.14 emphasizes the semiclassical interpretation of the deconvolution method. The integrand, the probability of detecting an excited state atom with velocity v' after transmission through the DSOF, is the product of two time-dependent probabilities, as predicted by the semiclassical approximation discussed in Sec. 2.3. The first of these results from the atom detection probability due the density matrix alone, while the second reflects the velocity dependent transmission probability through the DSOF.

To simplify our calculations, we consider the time average of Eq. 3.14. This is equivalent to studying only the $\omega_{det} = 0$ term in the deconvolution method of Sec. 3.2, and yields

$$\tilde{P}_e(\delta, \tilde{\delta}, \omega_{det} = 0) = A_o + \frac{1}{2}\int_{-\infty}^{\infty} d\Omega' \, |\rho(\Omega', \Omega' - \delta)| \times \cos\left(\frac{\tilde{\delta}L}{v'} - \phi(\Omega', \Omega' - \delta)\right). \quad (3.15)$$

For the case of $\delta = 0$ Eq. 3.15 reproduces[5] the usual expression for velocity averaged Ramsey fringes [45]. An appropriate cosine transform of this signal with respect to $\tilde{\delta}$ (Eq. 3.10) then yields the velocity distribution of the atoms in the ensemble, or equivalently the diagonal of density matrix.

If $\delta \neq 0$, the measured signal (*rephased* Ramsey fringes, as in Sec. 2.2.5) is sensitive to atoms whose time dependence is given by $\cos(\delta t)$, where $\delta = -\Omega_{coh}$ (the distance

[4] An extra factor of $\frac{1}{2}$ appears in the case of $\Omega_{coh} = 0$.

[5] For this dc term $\phi(\Omega', \Omega') = 0$ and, as Eq. 3.7 shows, $\tilde{\delta} \to \delta_1$ for $\delta = 0$.

off the diagonal of the density matrix in the quantum picture). In this case the time-dependent beat of the DSOF has been employed to heterodyne down the time-dependence of the initial atomic probability to dc. The amplitude of the Fourier transform of this signal yields the velocity distribution of the atoms oscillating at Ω_{coh}. The phase of this transform yields the phase of the time-dependent atom signal relative to a "clock" $\cos(\Omega_{coh}t)$ located at $x = 0$. This picture of the density matrix, in which off-diagonal stripes correspond to the velocity distributions of atoms in the beam associated with time-dependences at frequencies Ω_{coh}, is equivalent to the standard quantum picture in our semiclassical limit.

Chapter 4

Apparatus

The experimental apparatus used to perform our LAO and density matrix studies is described in this chapter. The major element, our atomic beam machine, has been continually improved by successive graduate students for more than twenty years. In the most recent round of rebuilding, we replaced the entire main beam tube in order to both accommodate our LAO experiments and to increase the flexibility of the apparatus for future transverse atom optics work. Since most of these changes have been described in great detail elsewhere [71], only a brief outline of the essential features of our machine is provided here, along with a more detailed description of elements that enabled the experiments in this thesis.

4.1 Beam Machine

The basic geometry of our beam machine is shown in Fig. 4-1. A fast ($\sim$ 1100 m/s) Na atomic beam emerges from the source and passes through a beam skimmer and two collimation slits, forming a vertical ribbon shaped-beam about 1 mm high. This beam then passes into the "main chamber" where various state selectors and LAO elements manipulate it. The atoms are finally detected by a scanning hot wire detector with 50 micron transverse spatial resolution. We discuss these various elements in the following sections.

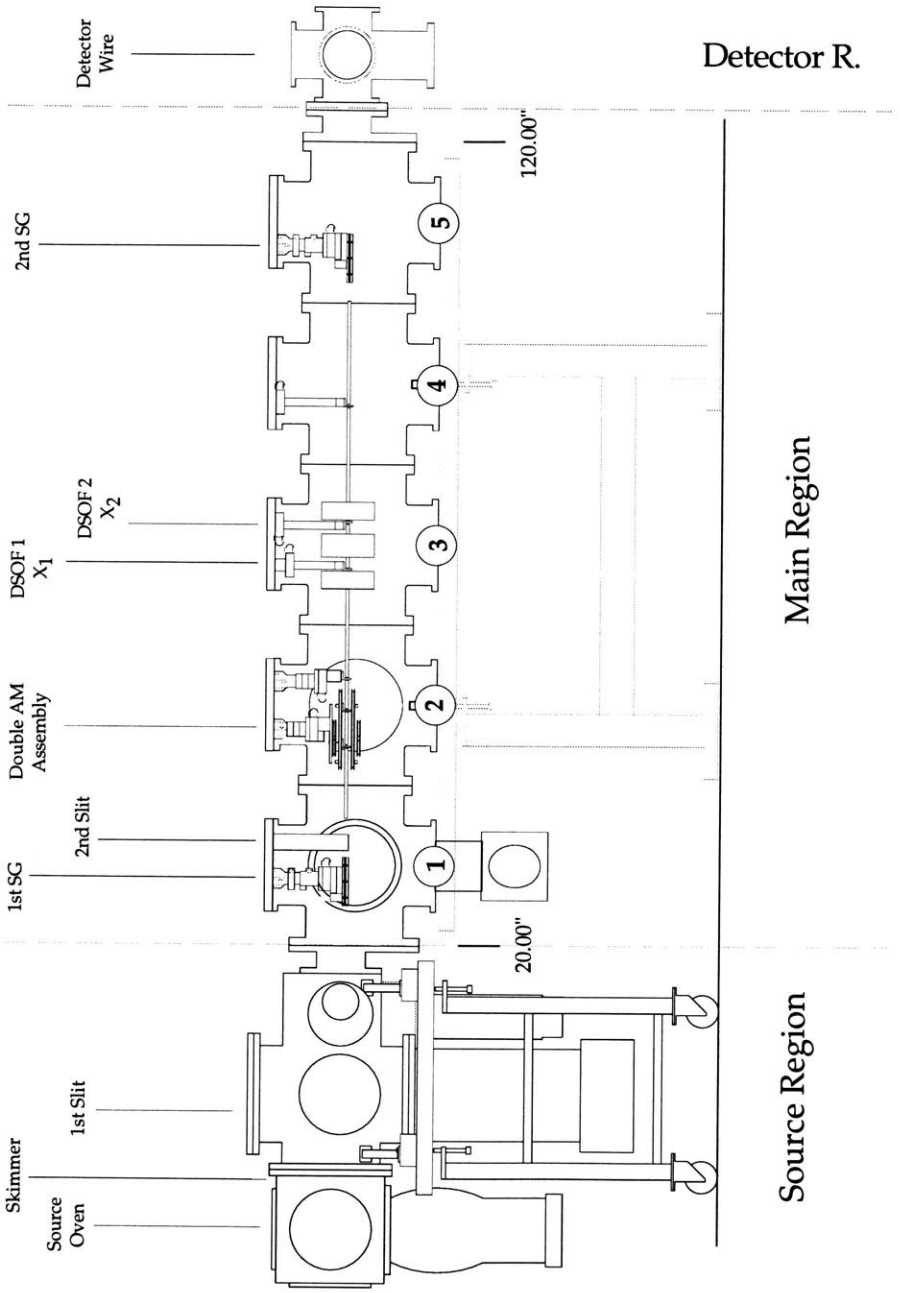

Figure 4-1: Apparatus schematic. The apparatus is composed of three major sections: the source region, main chamber, and detector chamber.

4.1.1 Source

Our atomic source is formed by supersonic expansion of a noble gas (typically Ar) seeded with Na. The resulting atomic beam is extremely bright $\sim 10^{20}$/ (sec strad cm^2) and has a typical mean velocity of 1100 m/s and a velocity width of $\sim 3.5\%$ rms. While the fundamental design of this source [101] has not changed in the last six years or so, during that interval I have been its main caretaker, and so will include here a number of details about its maintenance.

Our recent addition to the source of a larger reservoir has tremendously increased the length of time we can run our experiment without reloading the source with Na metal. Since this reloading procedure is messy and risks damaging the source, this is of great assistance in performing our experiments. In addition, the extra care with which we now wrap the source heaters with copper wire (to prevent heater hot spots and burnout) has resulted in a much more reliable source. We have been able to run it at high temperatures ($>$ 790 C for the nozzle) for extended periods of time without damaging the heaters. In fact, no source heater has burned out (although we blew many fuses in the heater current supplies) in over two years, a great increase in reliability.

Although the source's reliability has been improved, some challenges remain. The most serious maintenance problem with the source over the last two years has been clogging of the 1/8 in. diameter stainless steel gas inlet tube which introduces high pressure ($\sim$ 2 atm) Ar gas into the Na reservoir. This clogging likely arises because the end of the inlet cannot be directly heated, and hence is a cold point in the source, despite the fact that we preheat the incoming gas. At present to fix this problem we open up the source and drill out the gas inlet, a procedure which takes about two days. This process usually necessitates reloading of the reservoir because contact with air oxidizes the Na.

A permanent solution to this problem would involve redesign[1] of the source to

[1]A redesign of the source also ought to include an easier mechanical alignment mechanism. Another important consideration is that our detected atom flux always seemed to increase the further *away* we moved the nozzle from the beam skimmer, up to the current mechanical limit.

incorporate a larger diameter gas inlet, which would be slower to clog. Alternatively, one could dispense with this inlet tube altogether, allowing the gas to issue from the main body of the source ("swage elbow"), which is well heated and presumably less likely to clog. The current gas inlet, which has been damaged by multiple drill-outs, operates in essentially this configuration, and the source seems to operate satisfactorily without any of the feared problems with incomplete mixing of the Na and Ar.

4.1.2 Detector

Our atom detector consists of a 50 micron Re hot wire on which the Na atoms surface ionize. The resulting ions are accelerated by electric fields and are incident upon a channel electron multiplier (CEM), an electron cascade device which enables detection of single ions. As discussed in [71], we have replaced the separate CEM, discriminator electronics box, and biasing voltage supplies with a single integrated package (Amptektron MD-501 from Amptek, Bedford, MA), greatly increasing its reliability.

In order to obtain the necessary detector sensitivity, before each experimental run we oxidize the wire by exposing it to 10^{-4} torr of high purity O_2 for 2 minutes. Procedures for treatment of the detector wire have varied greatly over the last 5-10 years, and obtaining good sensitivity is something of a black art. We have found that the detected atom count rate can vary by a factor of four or more depending on the exact oxidation procedure. If atomic beam counts are anomalously low at the beginning of an experimental run, re-oxidation can sometimes restore the necessary sensitivity and raise the count rate.

A common problem in the past has been the tendency of the detector wire, which is heated by passage of a 200 mA current, to stretch and break over time. This is a limitation because in general the background noise count rate produced by a particular wire decreases over time, a feature which makes long wire lifetimes especially desirable.

Thus, a new design should allow a greater range of longitudinal translation of the source.

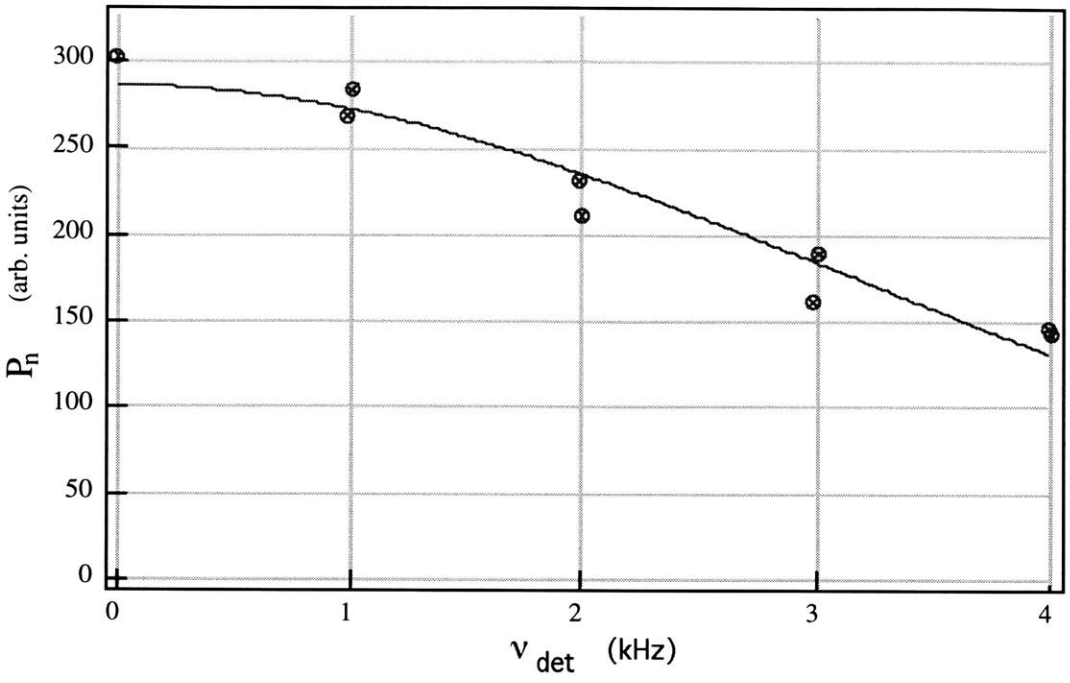

Figure 4-2: Detector frequency response measured by DSOF rephasing of amplitude modulation of the atomic beam. A fixed frequency modulation, $\nu_{det} = 50.008$ kHz was applied to the beam, and the DSOF beat frequency was set to $\delta = 50 \ldots 54$ kHz. The resulting time-dependent atom signal was measured for .6 sec, and the quasi-power spectrum P_n was determined. (See Sec. 5.4.1.) The solid line is a Gaussian fit, and yields $\sigma = 3.16$ kHz.

In the present detector wire, we have moved away from a previous system [102] in which the detector wire was mounted under tension in order to avoid wire curvature. While the removal of this system has led to a slightly curved detector wire, the present wire has survived for almost two years without breaking.

A longstanding question about our atom detection system is its frequency response. We have observed that an atom incident on our Re wire is not instantaneously ionized, an empirical fact that we tentatively attribute to the need for the atom to wander around on the surface until it finds a favorable site for ionization. While several aspects of the detector behavior support this model, we have no theoretical prediction for the mean time the atom should take to ionize.

Our recent implementation of LAO elements (AM region and DSOF interferometer) allowed us to accurately measure the frequency response of our detection system for the first time. To do so, we used the DSOF to rephase time-dependent modula-

tion, produced by an upstream AM, at the position of the detector. We obtained the power spectrum of this time-dependent atom signal and measured the detected signal power as a function of the applied modulation frequency. The data for this study is shown in Fig. 4-2, and the procedure for its acquisition is discussed in Sec. 5.4.1. Figure 4-2 shows that for a wire current of 160 mA, the detector frequency response has a roughly Gaussian falloff with an rms width of $\nu_{det} \sim 3$ kHz, corresponding to a 1/3 msec dwell time for an atom on the wire surface.

4.1.3 Vacuum System

As shown in Fig. 4-1 the vacuum system can be divided into three main parts: the source region, the main chamber, and the detector chamber. Each of these has its own vacuum pumps, and differential pumping is employed to steadily decrease the pressure from the source region (which has high pressure due to the large gas load produced by the source) to the detector region, where very low pressures are necessary to limit noise in the detected atom signal caused by the ionization of background gas. Plexiglass gate valves separate the chambers, permitting any chamber to be raised to atmosphere for repair or modification while the other two remain under vacuum. These gate valves also allow the optical access necessary for precise alignment of our atom optical elements.

The source chamber consists of three successive sub-chambers. The first of these contains the source oven, and is maintained at a pressure of about 2×10^{-4} torr by a NRC VHS-6 belly diffusion pump. The atomic beam then passes into the next chamber (first differential pumping chamber) through a 500 micron diameter skimmer (Beam Dynamics, Inc. Minneapolis, MN) that selects out a portion of the supersonic expansion from the source nozzle. The first DP chamber contains the first atom collimation slit and is pumped by an NRC HS-10 diffusion pump, which yields a pressure in the 10^{-6} torr range. The final source chamber (second differential pumping region), pumped by an NRC 4 inch belly diffusion pump, usually reaches a pressure of about 3×10^{-7} torr.

The diffusion pumps in these chambers formerly employed silicone based DC704

and DC705 fluids, which were susceptible to chemical breakdown through interaction with Na. This chemical change lead to the formation of crystalline deposits of oil in the upper portions of the diffusion pumps. While not a barrier to operating the machine for short times (the crystals could readily be melted down by turning off the diffusion pumps and applying heat to them), long term operation of the pumps resulted in substantial depletion of the oil in the pump reservoirs. This caused the pumps to overheat, scorching the insides and drastically decreasing the lifetime of the pump heaters. The time-consuming clean-ups and repairs resulting from this problem led us to look for alternative solutions, including incorporation of cold baffles to prevent the Na from reaching the oil, and use of heater tapes to raise the temperature of the upper parts of the pumps. The best solution turned out to be changing the pumping fluid. We now use Diffoil 30 (a hydrocarbon based oil obtained from Kurt J. Lesker, Clariton, PA), which does not chemically react with Na and has completely eliminated this problem.

The main vacuum chamber is pumped by a Balzers TPU 510 S turbomolecular pump with a pumping speed of 500 l/s. When combined with the use of a "cold finger" (a cold trap extending into the main chamber which can be filled with liquid nitrogen) pressures in the low 10^{-7} to high 10^{-8} torr range can be obtained.

Finally the detector chamber, which is pumped by a combination of a Varian V80-A turbomolecular pump and liquid nitrogen pumping surface, typically reaches pressures in the low to mid 10^{-8}'s, low enough to limit the background noise count rate to less than 1 kcount/sec. This low pressure was achieved after a rebuild of two flanges for the chamber, which previously contained small leaks that limited the ultimate chamber pressure.

4.2 Experimental Realization of LAO Devices

To motivate a description of the portions of the apparatus we employ for our LAO and density matrix studies, a short introduction to the experimental implementations of the LAO devices described in Ch. 2 is now provided.

As discussed in Chs. 2-3, we used a DSOF interferometer to study the density matrix of a matter wave beam. The DSOF, which operates by driving transitions between two internal states, was implemented for Na by driving the $|F = 1, m_F = 0\rangle \rightarrow |2, 0\rangle$ ($\Delta m = 0$) transition at 1772 MHz (Fig. 4-3). The insensitivity of this transition to external magnetic fields makes it ideal for producing a clean two-state system.

We drove the DSOF in several different configurations, each optimized for a different purpose. For general beam diagnostics (e.g. measuring its velocity distribution) we drove both DSOF coils from a single signal source, a technique that is equivalent to Ramsey's method of separated oscillatory fields [45]. Our experimental search for off-diagonal matrix elements produced by our source required control over the Rabi frequency (and hence the RF power) applied to each DSOF region, but did not require control over the relative phase of the two signals. Hence, in this experiment we used two independent signal sources to drive the DSOF coils. Finally, deconvolution of the density matrix required that we drive the two DSOF coils with two different frequencies while maintaining a coherent beat signal between them as they were swept. To do so, we constructed a single sideband modulator [103], which adds a coherent fixed frequency shift to the signal applied to one DSOF coil, while leaving the signal driving the other coil unchanged. The circuitry for these various DSOF configurations is described in Sec. 4.2.2.

The other major tool that we employ in our experiments is the amplitude modulator, which acts as an LAO beamsplitter. Amplitude modulation of our atomic beam is implemented by driving ($\Delta m = 1$) $|F = 1, m_F = 0\rangle \rightarrow |1, \pm 1\rangle$ Zeeman transitions in the $F = 1$ hyperfine manifold (Fig. 4-3). We applied time-dependent modulation by mixing this RF carrier signal ($\omega_c = 2\pi \times 7.65$ MHz), with a modulation frequency ω_m. For an incident beam $e^{i(k_o x - \Omega_o t)} |1, 0\rangle$, this produces a $|1, 0\rangle$ transmission amplitude

$$T(t) = \cos\left[\frac{\omega_R l}{v_o} \sin(\omega_m t)\right] \tag{4.1}$$

where $\omega_m \ll \omega_R$, the Rabi frequency of the oscillatory field region, and l is this region's length. This transmission amplitude replaces the simpler expression of Eq.

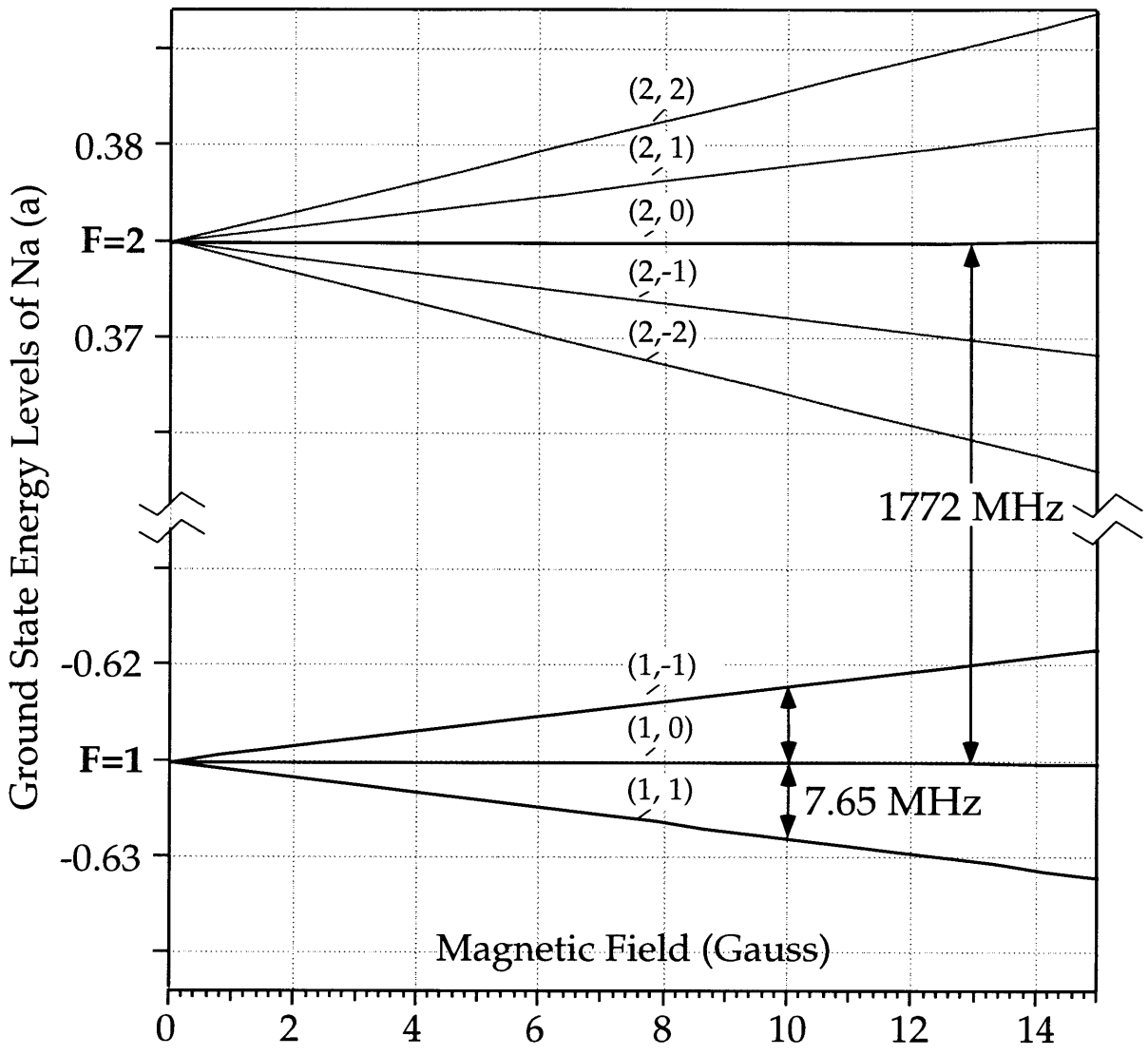

Figure 4-3: Level structure of Na $3S_{\frac{1}{2}}$ state, expressed in units of the hyperfine interval a = 1771.631 MHz. The $|F = 1, m_F = 0\rangle \rightarrow |2, 0\rangle$ DSOF transition and the $|1, 0\rangle \rightarrow |1, \pm 1\rangle$ transitions are shown.

2.15, and produces a wavefunction

$$
\begin{aligned}
|\Psi_{out}(x,t)\rangle &= \cos\left[\frac{\omega_R l}{v_o}\sin(\omega_m t)\right]|\Psi_{in}(x,t)\rangle \\
&= \sum_{-\infty}^{\infty} J_{2n}\left(\frac{\omega_R l}{v_o}\right) e^{i[(k_o+2n\frac{\omega_m}{v_o})x-(\Omega_o+2n\omega_m)t]}\,|1,0\rangle\,. \qquad (4.2)
\end{aligned}
$$

in the $|1,0\rangle$ state. This component is the only one observed by our atom detector (since $|1,\pm 1\rangle$ states are deflected away), and contains multiple kinetic energy components spaced at intervals of $2\omega_m$. We call this LAO element a"multi-sideband AM" beamsplitter.

The final major LAO tool we used is a device which employs two multi-sideband amplitude modulators separated by a distance L_c. Either AM alone would produce off-diagonal density matrix structure, but together they produce velocity (energy) dependent structure parallel to the diagonal as well. This device, which we employed to generate a non-trivial density matrix upon which to test our deconvolution method, is discussed further in Ch. 6.

4.2.1 Beamline

This section briefly describes the apparatus we employed to implement the LAO devices we have just discussed. As shown in Fig. 4-4, this include collimation slits, state preparation Stern-Gerlach magnets, and various oscillatory field regions. Further information about these elements can be found in Ref. [71].

Beam collimation was provided by a pair of slits separated by 72 cm. The slits were microfabricated from silicon and silicon nitride [104], and each slit chip contained five windows with widths varying from $\sim$ 12-60 microns, allowing us to adjust the width of the atomic beam. This was quite valuable, since it allowed us to select an optimum tradeoff between the ability to resolve various transverse beam features and the necessity of maximizing the atom count rate.

Since our LAO elements relied on transitions between internal atomic energy lev-

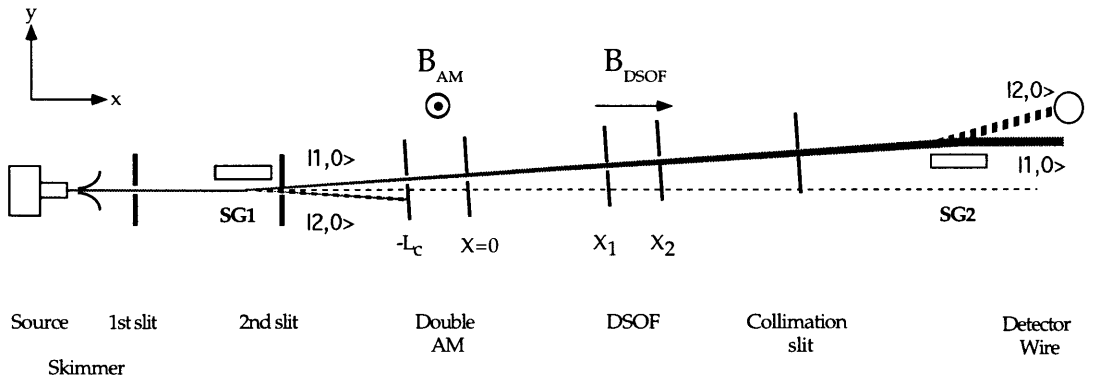

Figure 4-4: Top view of beamline employed for LAO and density matrix experiments. The first Stern-Gerlach magnet and collimation slits select the $|F = 1, m_F = 0\rangle$ (solid line) state. The DSOF regions at $x_{1,2}$ drive hyperfine transitions from $|1,0\rangle \rightarrow |2,0\rangle$, and the $|2,0\rangle$ state (thick striped line) is selected by a second Stern-Gerlach magnet. The double AM regions drive transitions to the $|1,\pm 1\rangle$ states (not shown) which are not observed by the detector.

els, we required a method to state select our Na beam. Two Stern-Gerlach magnets, the first placed between the first and second collimation slits, and the second at the end of the main chamber, were used to transversely separate the various magnetic sublevels. These SG magnets consisted of a two parallel wires (1/8 in. copper tube) carrying anti-parallel currents, which produced a large ($\sim$ 1000 gauss/cm) gradient in the magnetic field magnitude ($\sim$ 200 gauss) at the position of the atomic beam. These fields and gradients were sufficient to provide the necessary deflection of the $|1,0\rangle$ and $|2,0\rangle$ states through the second order Zeeman shift experienced by these levels. The high currents (45 and 160 A respectively) employed in these magnets produced substantial heat, which was removed by cooling water flowing through the centers of the copper tubes.

The sensitivity of the Na sublevels to external magnetic fields (the Na linear Zeeman shift causes interlevel splitting of $2\pi \times 0.77$ MHz/gauss for low fields) necessitated the use of field coils wound on the outside of our vacuum chamber to null out the earth's field, as well as to eliminate zero field regions which otherwise caused depolarization of the atoms (Majorana flops [105]). We also placed magnetic field coils inside the vacuum chamber to provide appropriate quantization axes for our oscillatory field regions. We used a four-wire magnet and small Helmholtz shim coils to apply a *verti-*

cal magnetic field to the two coils used to drive $|1,0\rangle \rightarrow |1,\pm 1\rangle$ ($\Delta m = 1$) transitions which produced AM of the atomic beam. Three solenoidal field coils produced a fairly uniform *longitudinal* magnetic field around the DSOF regions, which operated on the ($\Delta m = 0$) $|1,0\rangle \rightarrow |2,0\rangle$ transition.

The oscillatory field regions (hairpin coils) used to drive transitions in our experiments were constructed of 50 micron copper wire bonded to silicon chips for structural support. The center to center spacing of the two wires was about 170 microns, leading to transit time limited $1/e$ linewidths of $2\pi \times 1.1$ MHz and $2\pi \times 1.5$ MHz for DSOF coils 1 and 2 respectively.

To reduce stray RF radiation (which otherwise interacted with the atom at unwanted locations) we eliminated metallic parts inside the vacuum system wherever possible, substituting machinable ceramic (Macor) and glass-reinforced plastic (G-10). In addition, we surrounded the beamline with 3/8 in. copper tubing, which prevented radiation from reaching the atoms except in the neighborhood of the designated RF regions.

4.2.2 Radiofrequency Electronics

This section describes the frequency synthesizers and electronics which provided the RF signals for the DSOF, the AM, and the double AM systems.

We used two Hewlett-Packard HP8662A frequency synthesizers to generate $2\pi \times$ 1772 GHz. Since these devices were frequency limited to below $2\pi \times 1$ GHz, we first generated $2\pi \times 886$ MHz and employed FK-3000 frequency doublers (purchased, as were almost all our RF electronics, from Mini-Circuits, Brooklyn, NY) to reach $2\pi \times 1772$. To obtain SOF patterns, the output of a single HP8662A was split (ZAPD-2 (0°) splitter) and used to drive the two DSOF coils.

For the source search experiment (Ch. 5) we drove each DSOF coil with a separate HP8662A, allowing individual control over the applied RF powers. We locked together the internal clocks of these synthesizers, so that for any particular pair of frequency settings the two generated a phase coherent signal. However, when the DSOF frequencies were shifted to scan δ and $\tilde{\delta}$ (Eqs. 3.6-3.7), the relative phase between

the two synthesizers received a random shift—a drawback for coherent rephasing techniques, but unimportant for the "incoherent" search method we employed.

The density matrix deconvolution experiment (Ch. 6) required a way to scan $\tilde{\delta}$ while maintaining both a fixed frequency difference δ *and* phase coherence between the two coils. To achieve this we constructed a single sideband (SSB) modulator [103] which shifts the frequency of an incoming signal ω_c by an amount ω_{ssb}. This device, shown in Fig. 4-5, employs one HP8662A synthesizer (which also drives the first DSOF coil) to provide a high frequency carrier. Two low frequency DS345 synthesizers (Stanford Research Systems, Sunnyvale CA) supplied a frequency ω_{ssb} and provided the ability to independently vary the phase of the signal entering the two mixers, a necessity for optimizing the rejection of unwanted frequencies. The output of the SSB modulator at $(\omega_c - \omega_{ssb})$ was doubled and used to drive the second DSOF coil.

To generate RF signals for the AM coils, we use two DS345 synthesizers: the first provided a carrier frequency $\omega_c = 2\pi \times 7.65$ MHz, while second provided a modulation frequency which can range from 0 to $2\pi \times 200$ kHz. These two signals are mixed with a ZAD-1-1 mixer, and the output (which we observed on a digital oscilloscope, using its spectrum analysis function to check spectral purity) is sent to an ENI 350L radiofrequency amplifier. For the calibration step in the source search experiment (see Sec. 5.4.1), the output of this amplifier is first attenuated, and then delivered to a single upstream AM coil. However, for the deconvolution experiment (Sec. 6.4), the AM was split and used to synchronously drive both AM coils with the same frequency, but with different RF powers. The RF circuit that enabled this is shown in Fig. 4-6.

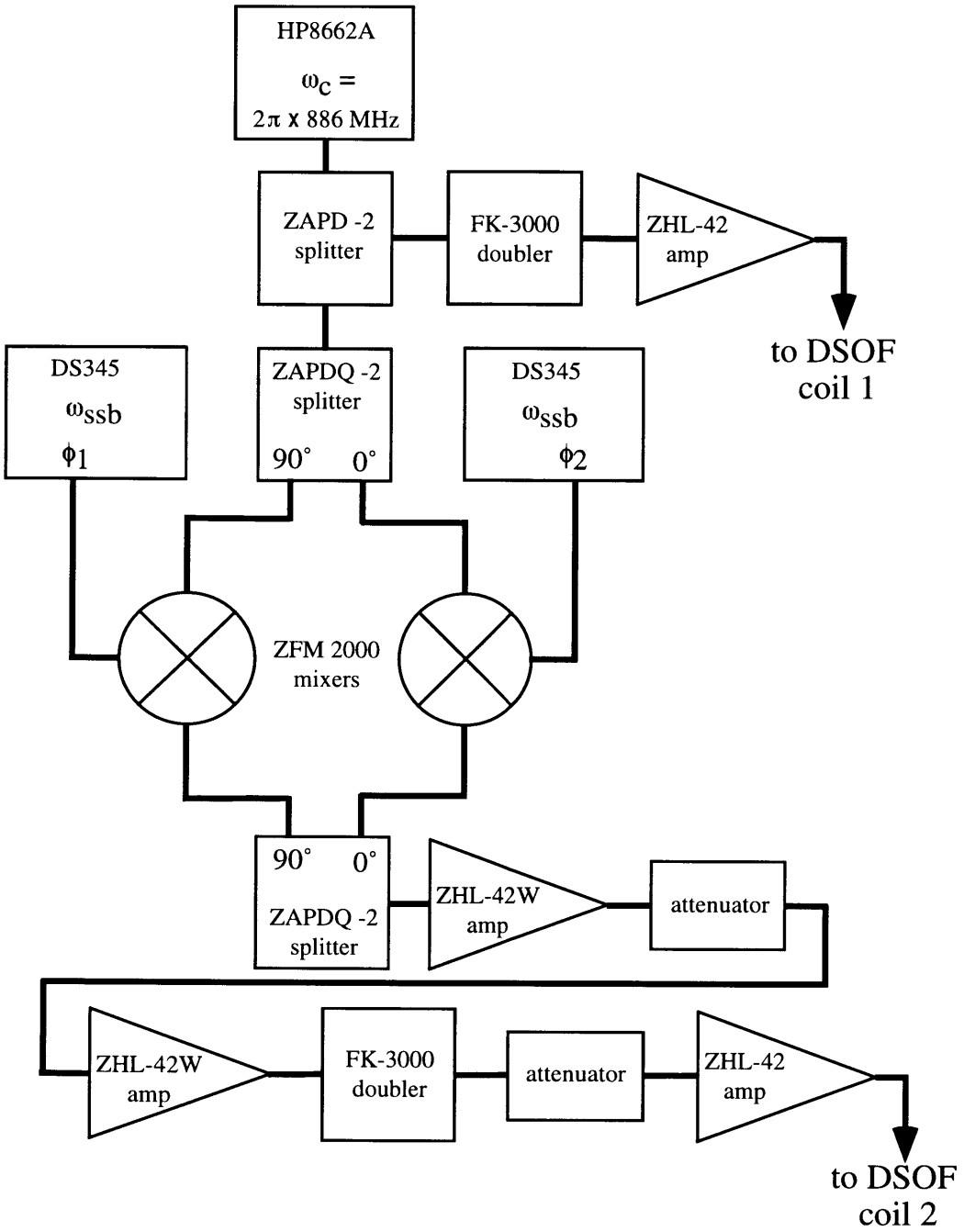

Figure 4-5: Schematic of single sideband modulator. DSOF coil 1 receives a frequency $2\omega_c$, and DSOF coil 2 receives $2(\omega_c - \omega_{ssb})$. In principle the two DS345 synthesizers could be replaced by a single synthesizer and a splitter, but the geometry shown allows independent control of the phase of the two ω_{ssb} signals, allowing greater rejection of unwanted frequencies.

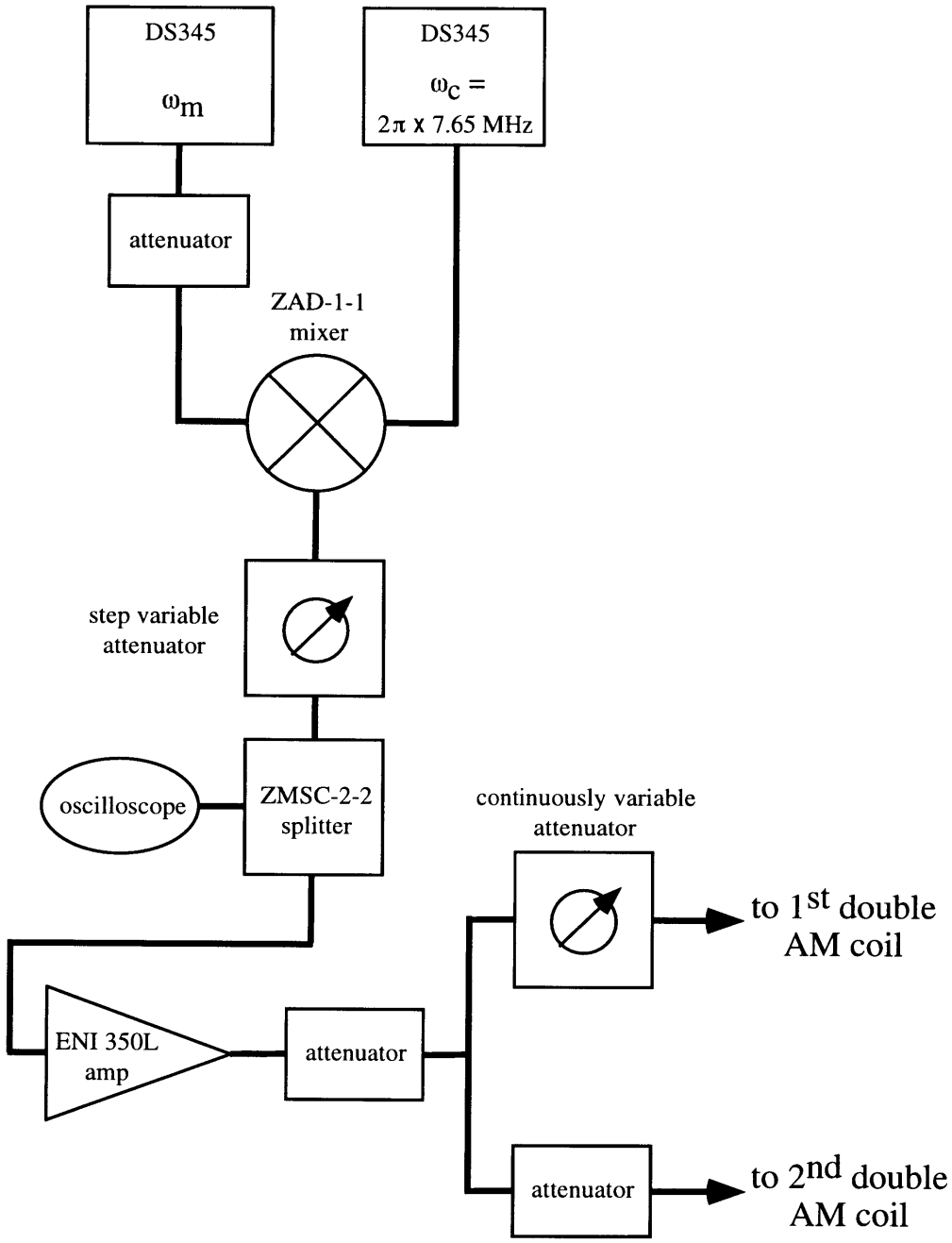

Figure 4-6: Schematic of double AM circuit. Carrier and modulator signals are mixed and the resulting signal is spectrum analyzed by the digital oscilloscope. The signal is then amplified and applied to the two AM coils. Variable RF attenuators allow independent adjustment of the power applied applied to each coil. (The fixed attenuators following the amplifier prevent excess power from reaching the AM coils.) For the source search calibration data (Sec. 5.4.1), a single continuously variable strength AM signal is applied to the beam via the first AM coil, and the second AM coil is disconnected.

4.3 General Data Acquisition Procedures: Aligning the Beam and Optimizing Resonance Regions

This section provides a short discussion of the general operation of the DSOF interferometer. Readers interested in this subject, as well as in further information about the atomic beam machine in general, are referred to several other theses produced by our group [71, 97, 104] that discuss these issues in greater detail.

4.3.1 Beam Alignment

To prepare for our LAO experiments, a collimated beam (with a typical count rate of $> 1.5 \times 10^6$ counts/sec) is first obtained by optimizing the source and the positions of the collimation slits (Fig. 4-4). The first Stern-Gerlach magnet (SG1) is then employed to spatially separate the eight Zeeman sublevels (Fig. 4-3), which, along with Na_2 dimers, are all present in the initially unpolarized beam.

All RF coils, including the double AM assembly and the DSOF coils, are sequentially scanned across the beam and centered on the $|1,0\rangle$ beam component by micromotors located inside the vacuum envelope. The count rate during these scans is monitored by a data acquisition system (Labview) enabling diagnosis of the beam profiles. By careful positioning of various RF oscillatory field coils, which because of their narrow transverse width also function as extra collimation slits, the $|1,0\rangle$ component of the beam can be isolated, yielding a polarized beam from which all other states have been discarded. The mean count rate in this polarized beam is typically between 120-200 kcount/sec.

The second Stern-Gerlach magnet (SG2) is next employed to redeflect (analyze) the $|1,0\rangle$ atoms. A scan of the atom detector wire at this stage usually reveals contamination by unwanted Zeeman states that slip past the RF collimation slits. By re-adjusting the positions of these slits $> 97\%$ of such undesired atoms can be eliminated.

A resonant π pulse is next applied to one of the two DSOF coils. The detector wire is then scanned to insure adequate separation of the $|1,0\rangle$ and $|2,0\rangle$ states by SG2, and then repositioned on the $|2,0\rangle$ peak for the remainder of the experiment. The final counts in the $|2,0\rangle$ are typically 80-150 kcounts/sec. However, drifts in the beam alignment tend to reduce this count rate to 50-80 kcounts/sec as an experimental run progresses.

Once the beamline has been established, the quantization fields applied to the DSOF and the AM regions are optimized. The vertical magnetic fields (which allows the AM coils to drive $\Delta m = \pm 1$ transitions) at the two AM regions are shimmed with small subsidiary pairs of magnetic field coils: successive single coil resonance scans are then taken, and the fields adjusted, until the two resonance frequencies are equal.

To optimize the DSOF magnetic guide fields, single coil resonance scans are taken and the longitudinal magnetic guide fields are adjusted until the resonance frequencies are equal for the two DSOF coils. These coils are then driven by a single HP8662A synthesizer and doubler, implementing a Ramsey SOF configuration. A scan of the Ramsey fringes is a useful diagnostic, allowing us to adjust the guide field in the region between the DSOF coils so that the SOF fringes are centered at the peak of the single coil resonance lines. In addition, a fit to the SOF fringes (see Fig. 4-7) yields the contrast of the SOF, which we can optimize by adding fixed attenuators to the input of one or the other coil so that both apply accurate $\frac{\pi}{2}$ pulses.

4.3.2 Single Coil Linewidth Enhancement

After the magnetic guide fields were set, we collected a series of single coil resonance scans for both the first and second DSOF regions, with a variety of different applied RF power settings. These scans were used to calculate the RF power needed to produce $\pi/2$ pulses over the broadest possible range of detunings, allowing us to determine the necessary power to apply to each DSOF coil for each frequency. Scans of the single coil resonance lines with and without this "power boost" technique are shown in Fig. 4-8. A substantial increase in the effective linewidth of the transition is obtained, which greatly increases the range of off-diagonal matrix elements that can

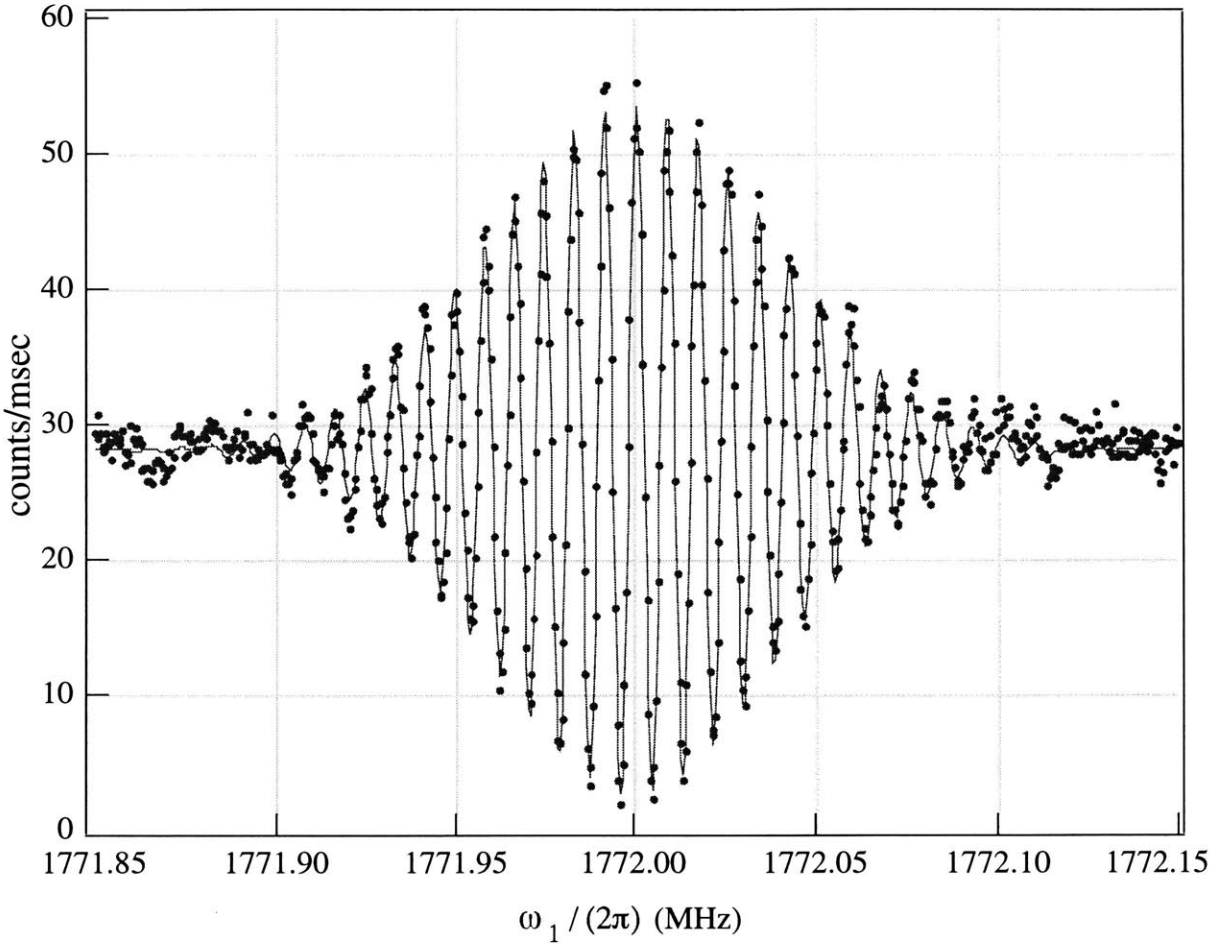

Figure 4-7: Ramsey fringes produced by DSOF with same signal driving both coils. Dots are points, and solid line is a fit, which yields a contrast of 92.7%.

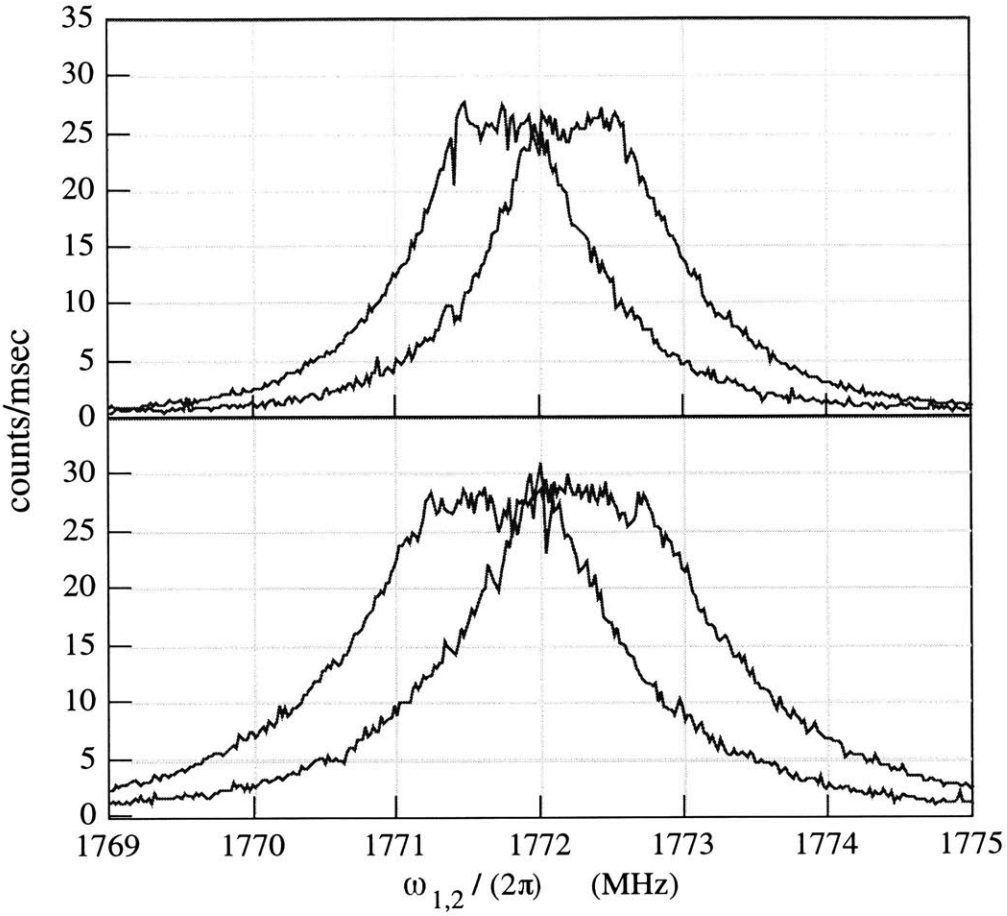

Figure 4-8: Single coil resonance scans with and without power boost. Top: DSOF coil 1. Bottom: DSOF coil 2. The boosted linewidths are more than twice the unboosted $1/e$ linewidths of $2\pi\times$ 1.09 (1.50) MHz.

be probed by the DSOF in our source search experiment (Ch. 5).

While the power boost technique was extremely useful in extending the range of the DSOF in the source search experiment, it could not be employed for the density matrix deconvolution, because the single sideband modulator which coherently drove the DSOF coils could not accommodate computer control of the power applied to the two different DSOF coils. For small detunings, powers equivalent to standard $\frac{\pi}{2}$ pulses were applied to both coils, resulting in satisfactory signal/noise in this range. When large detunings were required, we increased the number of counts in the $|2,0\rangle$ state (and hence the sensitivity of our experiment) by using higher powers corresponding to on-resonance π pulses. Figure 4-9 shows scans of ω_1 for $\frac{\pi}{2}$ and π pulses applied

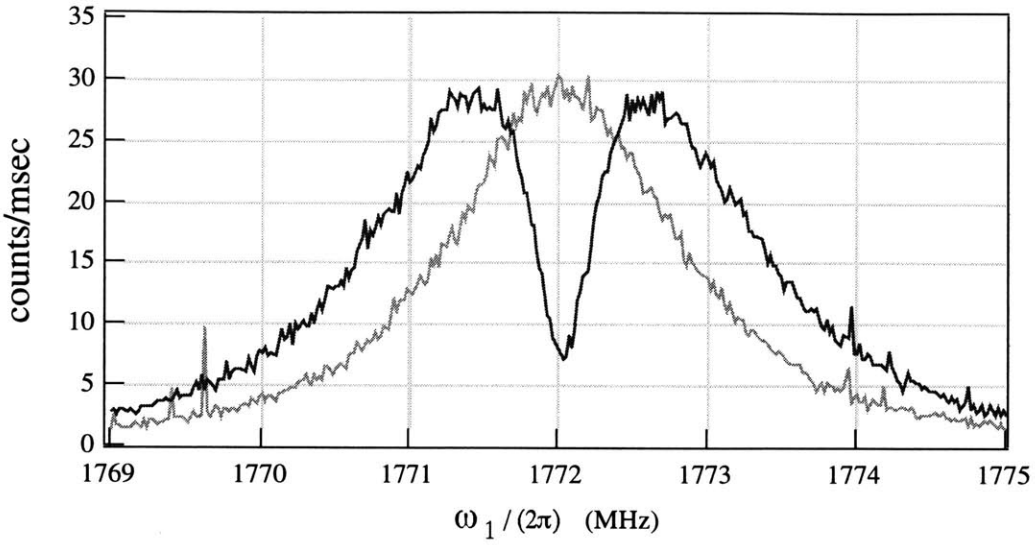

Figure 4-9: Rabi profile measured when driving both DSOF coils with the single sideband modulator, which applies frequency ω_1 to the first DSOF coil and $\omega_2 = \omega_1 - \delta$ to the second. Dark line: $\frac{\pi}{2}$ pulse. Light line: π pulse.

to both DSOF coils through the single sideband modulator circuit with $\delta = 2\pi \times 80$ kHz. For detunings greater than $2\pi \times 300$ kHz, the larger power (π) results in an increase in counts of $\sim 30 - 60\%$ relative to the lower power ($\frac{\pi}{2}$).

Chapter 5

Search for Off-Diagonal Matrix Elements

This chapter describes our experimental search for coherent structure (correlations between different plane wave components) in a matter wave beam's longitudinal energy/momentum state. We placed a strict limit on the size of off-diagonal density matrix elements which could have escaped detection by our experiment, and hence effectively ruled out the presence of coherent wavepackets within the search range. The chapter begins with a short introduction to our search method, followed by a paper, "Search for Off-Diagonal Density Matrix Elements for Atoms in a Supersonic Beam," which has been submitted to Physical Review Letters. Finally, theoretical details relevant to our search technique are presented, as well as a more complete description of the data analysis and sensitivity calibration of the experiment.

5.1 Introduction to Search

The coherence structure of matter wave beams has been the subject of great theoretical interest [60, 85, 96], as well some controversy (see [82, 83, 84] and Sec. 3.1), but until now there have been no experimental tests of this issue. We have performed the first experimental study of the longitudinal quantum state of a real atomic beam. In particular, we searched over a wide range of frequencies (from dc to $2\pi \times 100$ kHz) for

amplitude modulation produced by our supersonic atom source. (We discuss in Sec. 5.3.3 the sensitivity of our search to off-diagonal elements produced by other means.)

As discussed in Ch. 3, the presence of coherent superpositions of energy eigenstates in an atomic beam can lead to oscillatory behavior of the detected atomic probability. The energy separation between different plane wave components, $\hbar\Omega_{coh}$, can lead to high frequency signals that our slow atom detector cannot observe directly, necessitating use of a heterodyne technique to increase the off-diagonal range of the search (Sec. 3.2). The DSOF interferometer can perform this heterodyne function and is thus perfectly suited to this task. In addition, the ability of the DSOF to reverse the dephasing effects of a finite velocity distribution—which otherwise washes out the oscillatory signal caused by the presence of off-diagonal elements—is invaluable in the search for coherent superpositions of energy states.

While the coherent DSOF density matrix deconvolution scheme described in Ch. 3 could in principle be used to measure off-diagonal elements in our supersonic beam, it is vulnerable to fluctuations in the phase of the incoming atom signal or in the relative phase of the two DSOF coils (Sec. 4.2.2). Thus, in our search we opted to employ an "incoherent" technique, which measures the power spectrum of the time-dependent atom signal downstream of the DSOF. This method retains the principal benefit of the coherent deconvolution technique of Ch. 3, the ability to exploit the entire bandwidth of our atom detector, but is insensitive to the phase of the time-dependent oscillations of the detected atom signal. These features allow us to average together multiple power spectra, greatly increasing the sensitivity of our search.

Note that in this paper the DSOF variables δ, $\tilde{\delta}$ are defined in frequency units, rather than in radians/sec, as is the case everywhere else in this thesis.

5.2 Paper: Search for Off-Diagonal Density Matrix Elements for Atoms in a Supersonic Beam

Richard A. Rubenstein, Al-Amin Dhirani, David A. Kokorowski, Tony D. Roberts, Edward T. Smith, Winthrop W. Smith,[1] Herbert J. Bernstein,[2] Jana Lehner, Subhadeep Gupta, and David E. Pritchard

Massachusetts Institute of Technology,

Cambridge, Massachusetts 02139

Abstract

We demonstrate the absence of off-diagonal elements for the density matrix of a supersonic Na atomic beam, thus showing that there are no coherent wavepackets emerging from this source. We used a differentially detuned separated oscillatory field longitudinal interferometer to search for off-diagonal density matrix elements in the longitudinal energy/momentum basis. Our study places a stringent lower bound on their possible size over an off-diagonal energy range from 0 to 100 kHz.

PACS: 03.75.Dg,39.10.+j,03.75.-b

Atomic beam experiments, from early resonance studies [45] to modern work in atom optics and interferometry [14], invariably make assumptions about the correct treatment of atomic longitudinal motion (e.g. classical, wavepacket, plane wave). Despite some theoretical discussion [60, 81, 85, 94, 98], to date no experimental test has been performed which can discriminate between these alternative descriptions. This omission, along with the development of novel atomic sources with interesting coherence properties (cold atom beams, atom lasers [106]) demonstrates the need

[1]Present Address: Physics Department, University of Connecticut U-46, 2152 Hillside Road, Storrs, CT, 06269.

[2]Present Address: Hampshire College and Institute for Science and Interdisciplinary Studies, Amherst, Massachusetts 01002.

for experiments which probe not only the transverse [41], but also the longitudinal quantum state of atomic beams.

In this Letter, we present the first experimental limits on the size of off-diagonal matrix elements (ODEs) in the longitudinal energy/momentum density matrix characterizing a supersonic atomic beam. This demonstration, together with a determination of the beam's energy distribution, constitutes a measurement of the density matrix, the most complete possible description of the longitudinal quantum state of the ensemble of atoms in the atomic beam.

In the energy basis $h\nu = (\hbar k)^2/(2m)$, the time-dependence of any density matrix element is given by

$$\rho(\nu', \nu'', t) = \rho_o(\nu', \nu' + \nu_{coh}) e^{i2\pi\nu_{coh}(t-t_o)}, \tag{5.1}$$

where $\nu_{coh} \equiv \nu'' - \nu'$, t_o is an initial reference time, and $\rho_o = \rho(t_o)$. Here ν_{coh} is the distance off the diagonal of the density matrix, while ν' is the coordinate parallel to the diagonal.

It is tempting to consider an atomic beam source as emitting a stream of wavepackets, each necessarily possessing a coherent superposition of various longitudinal momenta and hence non-zero ODEs. However, the density matrix for an ensemble of such atoms contains an average over the randomly distributed initial time t_o of each wavepacket, causing all ODEs to be zero if the source is temporally stationary (e.g. an effusive atom oven in thermal equilibrium).

For a non-stationary source, the ensemble average need not make all ODEs zero, because the distribution of t_o's can be non-random. Thus non-stationary sources can contain coherent, physically observable wavepackets. Our beam is created via supersonic expansion of Na seeded in ~ 2 atm of Ar, which passes through a sharp-edged beam skimmer with a hole diameter of $d = 0.5$ mm. This arrangement, which yields a sound velocity at the skimmer of $v_s \sim 50$ m/s, may contain non-stationary hydrodynamic instabilities. These could create time-dependent amplitude modulation of the beam, and hence non-zero ODEs, with expected frequencies ν_{coh} up to $v_s/d \simeq$

100 kHz.

The time-dependence of the ODEs implies that a time-dependent experiment is required to observe them, in contrast to previous measurements of angular [107] or transverse [37, 41] correlations, and contrary to assertions elsewhere.[3] In this experiment, we used the differentially detuned separated oscillatory field (DSOF) longitudinal interferometer of Ref. [68] as the time-dependent apparatus necessary to study the relative phases of different energy components and thereby to search for ODEs. We first studied intentionally applied ODEs created via amplitude modulation of the beam [68, 99] for calibration purposes. Our search then employed this calibration to place an upper bound on the magnitude of the ODEs created by our source.

To determine the range of our search, we measured the velocity (and hence the energy) distribution of atoms emitted from our source, using the technique of separated oscillatory fields (SOF), and found a nearly Gaussian distribution with a mean frequency of 3.4×10^{13} Hz (1090 m/s) and an rms width of 2.2×10^{12} Hz (35 m/s). As we expected off-diagonal structure on the scale of 100 kHz, we searched a narrow ribbon in the neighborhood of the diagonal of the density matrix.

5.2.1 Using DSOF to Search for Off-Diagonal Matrix Elements

To illustrate how DSOF can be used to detect non-zero ODEs, we consider an incident beam of ground state two-level atoms in a superposition of plane wave components whose total energies differ by $h\nu_{coh}$ (so $\rho_o(\nu', \nu' + \nu_{coh}) \neq 0$). This beam emerges from a source at $x = 0$ (see Fig. 5-1) and propagates through two differentially detuned radiofrequency oscillatory field regions located at x_1 and $x_2 = x_1 + L$, where RF fields of frequency $f_{1,2}$ drive transitions (with resonance frequency f_{res}) between ground and excited states. This configuration is a longitudinal interferometer in which the

[3]Time-independent experiments, such as studies of off-diagonal elements of the density matrix in the position basis $\rho(x', x'')$ [82, 83, 108, 109] determine only the energy distribution of the ensemble (the diagonal $\rho(\nu', \nu')$ of the density matrix) and cannot detect energy/momentum ODEs [84, 85, 110].

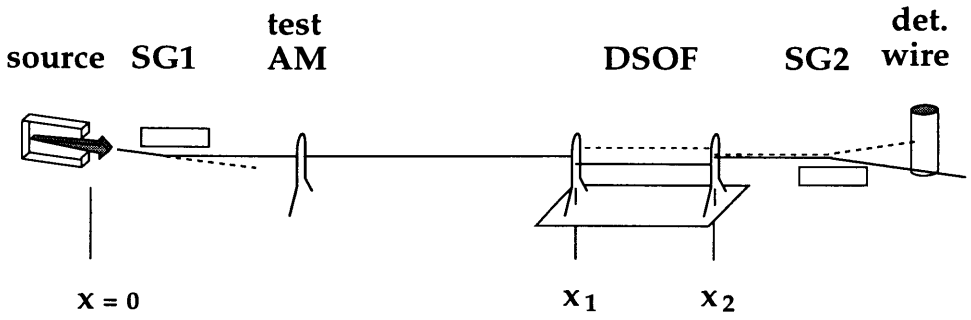

Figure 5-1: A schematic of the apparatus. The atomic beam emerges from the source at $x = 0$. The Na ground state $|F = 1, m_F = 0\rangle$ (solid line) is selected by the Stern-Gerlach magnet SG1. Hairpin coils at longitudinal positions $x_{1,2}$ with oscillatory fields of frequency $f_{1,2}$ drive energy/momentum and state changing transitions, form the DSOF interferometer. The excited $|2, 0\rangle$ (dashed line) state is selected by the second Stern-Gerlach magnet SG2 and detected by a scanning Re hot wire.

incident frequency component ν excited by f_1 and the $\nu + \nu_{coh}$ component excited by f_2 can interfere, producing a time-dependent beat at the detector with frequency

$$\nu_{det} = \delta - \nu_{coh} \tag{5.2}$$

(which may be negative), where

$$\delta = f_1 - f_2. \tag{5.3}$$

Thus, the DSOF can heterodyne down high frequency ODEs, allowing their detection by our Re hot wire ionization detector, whose response falls off rapidly beyond 3 kHz.

In our experiment we measured the time-dependent probability $p_e(\delta, \tilde{\delta}, t)$ of detecting an atom in the excited state after the DSOF, where we have defined the scaled detuning

$$\tilde{\delta} = \frac{f_2 x_2 - f_1 x_1}{L} - f_{res}. \tag{5.4}$$

For the case of our fast atomic beam [81], the double Fourier transform of $p_e(\delta, \tilde{\delta}, t)$ yields the density matrix:

$$\rho_o\left(\nu', \nu' + \delta - \nu_{det}\right) = A \int d\tilde{\delta}\, \tilde{p}_e(\delta, \tilde{\delta}, \nu_{det}) e^{-i\tilde{\delta}b/\sqrt{\nu'}}, \tag{5.5}$$

where δ, ν_{det} are related to ν_{coh} by Eq. 5.2, the constants A and b are defined in Ref. [81], and $\tilde{p}_e$ is the time Fourier transform of p_e. As Eq. 5.5 shows, $\tilde{p}_e(\delta, \tilde{\delta}, \nu_{det})$ contains information about a stripe of the density matrix parallel to the diagonal, and offset from the diagonal by an amount $\nu_{coh} = \delta - \nu_{det}$. Thus a full set of $\tilde{p}_e(\delta, \tilde{\delta}, \nu_{det})$ data provides more than enough information to determine the density matrix.

A general problem in searching for time-dependent coherences is that their phase is neither guaranteed to be stable nor known in advance—hence phase-coherent methods of data acquisition (such as are necessary to determine the full density matrix as in Eq. 5.5) could average a momentarily coherent signal to zero. We circumvented this by studying the power spectrum of the time-dependent data, $|\tilde{p}_e|^2$, which is not sensitive to the phase. As our data will demonstrate, our study found $|\tilde{p}_e| = 0$ for all $(\delta = \nu_{coh} + \nu_{det}, \tilde{\delta}, \nu_{det})$ within our search range. This information alone can rule out the presence of ODEs because, as Eq. 5.5 shows, if $|\tilde{p}_e|$ is equal to zero then all ODEs $\rho_o(\nu', \nu' + \nu_{coh})$ are likewise zero.

We measured $p_e(\delta, \tilde{\delta}, t)$ on a $(\delta,\tilde{\delta})$ grid with δ ranging from 0 to 100 kHz in 1 kHz increments. For each δ we took data at values of $\tilde{\delta}$ between -230 and 234 kHz, in 8 kHz steps. For each $(\delta, \tilde{\delta})$ pair, we collected 6000 samples of counts vs time data, with 75 μsec/sample and approximately 25 μsec intervening dead time. Our DSOF technique (which reduces the signal by a factor of two) and raw count rate of 42 kcounts/sec yielded an average of 1.5 counts/sample. These data were passed through an algorithm (Lomb periodogram [111, 112]) to convert our unevenly time sampled data into a quasi-power spectrum $P(\delta, \tilde{\delta}, \nu_{det})$ which approximates $|\tilde{p}_e|^2$. To increase the sensitivity of our search, we averaged together spectra from four identically obtained data sets. By examining the power spectra, our search scheme employed the full bandwidth of our time-dependent detector to search for ODEs with resolution in ν_{coh} of < 1 Hz (determined by the data acquisition time for the 6000 samples), without requiring us to increment δ in 1 Hz steps.

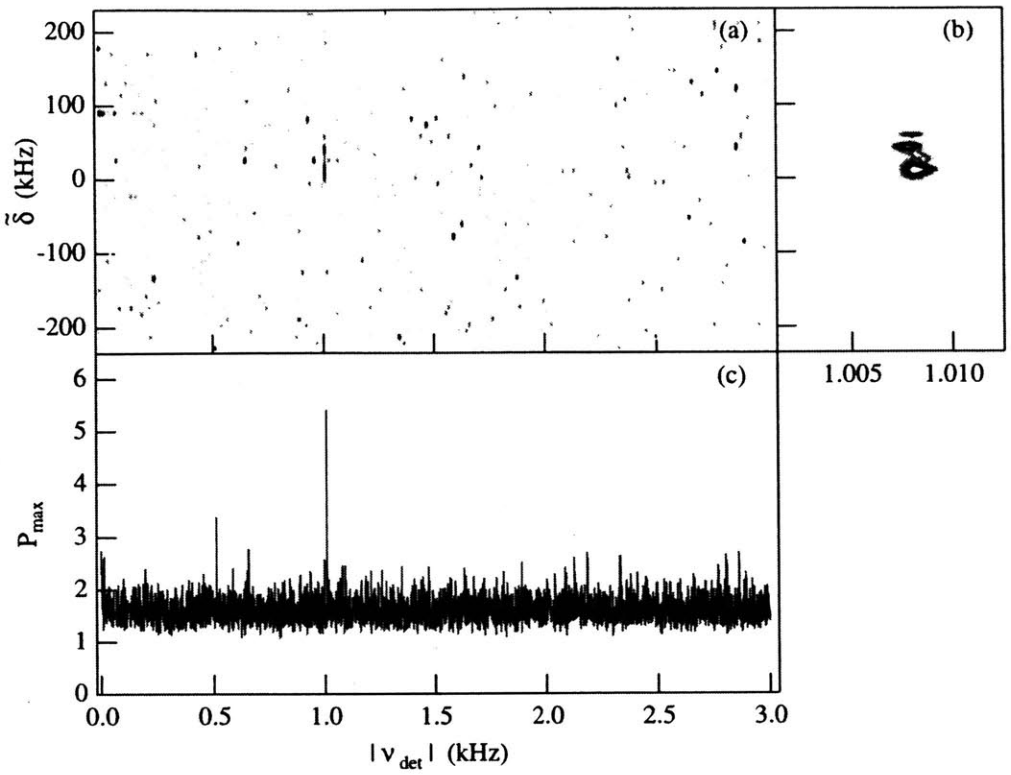

Figure 5-2: (a) Quasi-power spectrum $P(\delta, \tilde{\delta}, \nu_{det})$ with $\delta = 49$ kHz, for 5.3% amplitude modulation applied at $\nu_{coh} = 50.008$ kHz. The $\tilde{\delta}$ position of the peak reveals the location of the modulation source, while its $|\nu_{det}|$ position at 1.008 kHz demonstrates the presence of modulation (and thus of non-zero ODEs) at $\nu_{coh} = \delta - \nu_{det}$. (b) Close up of rephasing peak. (c) $P_{max}(\nu_{det})$ for $\delta = 49$ kHz.

The ODEs we search for appear as amplitude modulation,[4] which dephases downstream of its origin x_o due to the finite energy distribution of atoms in the beam. This dephasing is reversed by the DSOF near [68, 99]

$$\tilde{\delta}_{reph} \simeq (\nu_{coh} - \delta) \frac{(x_d - x_o)}{L} - \delta \frac{x_o}{L}, \tag{5.6}$$

where x_d is the location of the atom detector. This produces a "rephasing peak" in P centered around $\tilde{\delta}_{reph}$, with an rms width of 32 kHz in the variable $\tilde{\delta}$. Figure 5-2a depicts such a rephasing peak, for 5.3% amplitude modulation produced by a modulated oscillatory field region [68, 99] with $\nu_{coh} = 50.008$ kHz.

[4]Phase modulation is not detectable until the beam has propagated kilometers downstream [99].

To take advantage of the $\tilde{\delta}$ width of the rephasing peaks, we averaged $P(\delta, \tilde{\delta}, \nu_{det})$ along $\tilde{\delta}$ with a window size of 40 kHz, increasing our signal/noise by about a factor of two. We summarized our data by considering only the highest value of the averaged $P(\delta, \tilde{\delta}, \nu_{det})$ along the $\tilde{\delta}$ axis, $P_{max}(\delta, \nu_{det})$, as shown in Fig. 5-2c.

If amplitude modulation at some ν_{coh} is present, it appears as peaks in the $P_{max}(\delta, \nu_{det})$ curves for which δ differs from ν_{coh} by less than the maximum detector response frequency. Because our detector cannot distinguish between positive and negative frequencies ν_{det}, a particular peak indicates coherence at either $\nu_{coh} = \delta + \nu_{det}$ or $\delta - \nu_{det}$. Therefore, for each δ we mapped each $P_{max}(\delta, \nu_{det})$ to its two possible ν_{coh} positions. When we averaged together curves from five[5] neighboring values of δ to obtain P_{ave}, real time-dependent signals added together at ν_{coh}, increasing our signal/noise by a further factor of two. This averaging process also produced spurious peaks, or images, at other values of ν_{coh}, but these did not average constructively and hence were of reduced height. Figure 5-3 shows $P_{ave}(\nu_{coh})$ for the case of our intentionally applied amplitude modulation. The large peak visible at $\nu_{coh} = 50.008$ kHz shows the presence of the modulation (and its image at $\nu_{coh} = 51.992$) demonstrating the effectiveness and calibrating the sensitivity of our search technique.

We next employed the DSOF to search for ODEs created by amplitude modulation arising from our atomic beam source. Figure 5-4b shows $P_{ave}(\nu_{coh})$ for the 0 to 100 kHz range of our source search. We have removed large time-dependent signals caused by the presence of the DSOF itself (which creates detectable amplitude modulation when $\delta = 1, 2$, and 3 kHz) as well as noise at $\nu_{det} = 60, 120$ Hz and low frequency noise below $\nu_{det} = 15$ Hz. Our data sampling rate of about 10 kHz created the large spurious peak at this frequency and subsidiary image peaks at $\nu_{coh} \simeq 6$ and 8 kHz.

The smallest amplitude modulation which our search could detect with $> 99\%$ confidence (the "threshold") was calculated from the mean count rate in the atomic beam and the contrast of the DSOF interferometer, and is shown in Fig. 5-4a. This threshold rises for large ν_{coh}, where the frequencies $f_{1,2}$ fell outside the linewidths of the oscillating field regions (even when enhanced by increasing the applied field

[5]For this calibration, we averaged three δ values, while for the source search we used five.

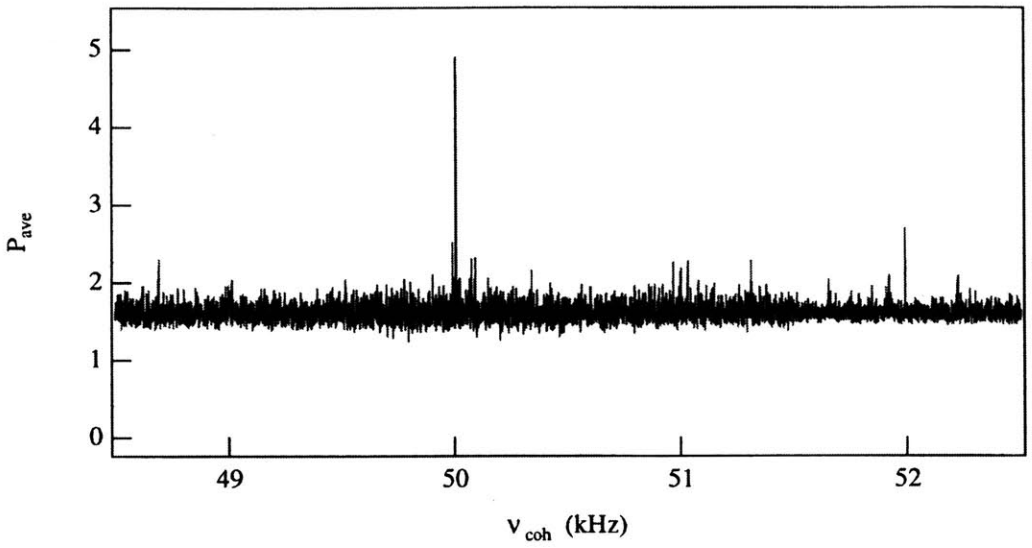

Figure 5-3: $P_{ave}(\nu_{coh})$ reveals the presence of 5.3% amplitude modulation at $\nu_{coh} = 50.008$ kHz.

strength) preventing the application of full $\pi/2$ pulses (assumed in [81]).

Our data limits the possible size of ODEs to less than those in a 4.0% amplitude modulated[6] atomic beam for $\nu_{coh} < 50$ kHz, with the threshold gradually rising to $\sim 7\%$ at $\nu_{coh} = 100$ kHz. The search covered a range of 0 to 100 kHz in ν_{coh} with < 1 Hz resolution, corresponding to an examination of the density matrix with a resolution of ~ 3 parts in 10^{14} perpendicular to the diagonal. Our resolution in ν' (determined by our $\tilde{\delta}$ range) was $\sim 5.1 \times 10^{11}$ Hz, or about 1.5 parts in 100 parallel to the diagonal of the density matrix.

5.2.2 Conclusion

We employed a longitudinal atom interferometer to put strict limits on the size of possible off-diagonal elements of the longitudinal energy/momentum density matrix of our supersonic Na atomic beam, thus ruling out the presence of coherent wavepackets within the range of our search. By measuring the beam's energy distribution, we obtained the density matrix for this system, a result which extends previous theo-

[6]Amplitude modulation is defined as multiplication of the incoming plane wave by $[1 + m\cos(\omega_m t)]$, where m is the modulation index [103].

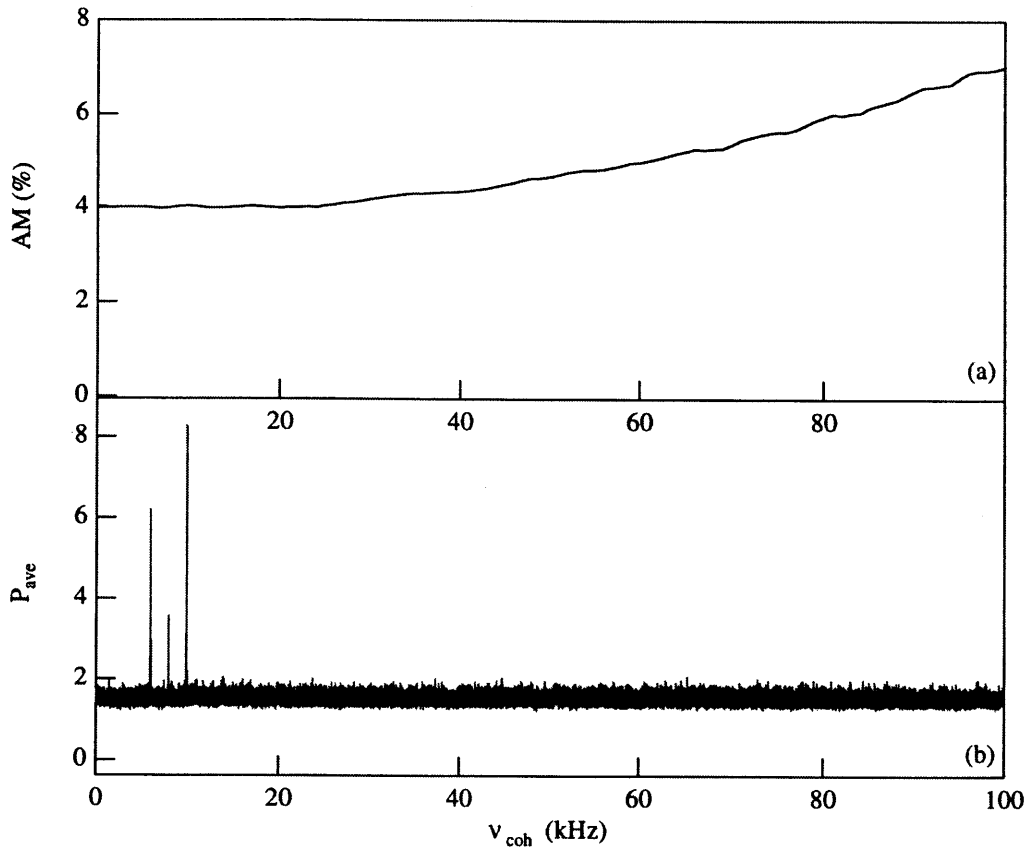

Figure 5-4: (a) Amplitude modulation our search could detect with $> 99\%$ confidence. (b) $P_{ave}(\nu_{coh})$ for the entire search. Detector sampling rate at $\nu_{coh} \simeq 10$ kHz as well as its subsidiary images can be seen.

retical [37, 39, 98] and experimental [41, 107] work for transverse coherences to the longitudinal [81, 94, 98] case.

In an upcoming publication we will describe an experiment in which we use the DSOF technique to measure the density matrix of a more complex system, possessing non-trivial structure both along and off the diagonal. In future experiments, the DSOF could be employed to apply large kinetic energy shifts to beams of cold atoms or Bose-Einstein condensates (which can have narrow energy distributions and large coherence lengths), reaching further into the quantum regime [50, 99] and providing a new tool for studying the longitudinal quantum state of such systems.

We thank R. Lutwak and W. Phillips of NIST and D. Fried, T. Killian, and D. Kleppner of MIT for the loan of frequency synthesizers, as well as D. Stamper-Kurn for comments on the manuscript. This work was supported by Army Research Office contracts DAAH04-94-G-0170, DAAH04-95-1-0533, DAAG55-97-1-0236, and DAAG55-98-1-0429, Office of Naval Research contract N000014-96-1-0432, Joint Services Electronics Program contracts DAAH04-95-1-0038 and DAAG55-98-1-0080, and National Science Foundation grant PHY-9514795. J. Lehner was supported by the Otto Hahn Award of the Max Planck Society, and H. Bernstein acknowledges the support of National Science Foundation grant PHY-9722614.

Note that we now return to units of radians/sec for all quantities, including δ, $\tilde{\delta}$.

5.3 Theoretical Issues for the Source Search

This section discusses some of the theoretical aspects of our search for ODE's produced by the source.

5.3.1 Search Resolution and Range

Our search technique is a variant of the density matrix deconvolution scheme described in Sec. 3.2, and measures the power spectrum (rather than the Fourier transform) of the time-dependent signal after the DSOF. This phase insensitive method has the same resolution limits as the complete deconvolution technique. The $\sim$ 600 msec observation time per $\delta, \tilde{\delta}$ point in our search leads to an Ω_{coh} resolution (perpendicular to the diagonal) of about $2\pi \times 1$ Hz (see Eq. 3.11). To determine the resolution of our search parallel to the diagonal of the density matrix, we employ Eq. 3.12 and the $2\pi \times 460$ kHz $\tilde{\delta}$ range of our search, finding a resolution of $2\pi \times 5.1 \times 10^{11}$ Hz in Ω'.

The limited $\tilde{\delta}$ range of our search can also be interpreted as a limitation of the longitudinal region in which we can observe AM applied to the atomic beam. This region is centered around $x = 0$ (the nominal position of our atom source and the origin of our coordinate system) can be calculated from Eq. 5.6, and extends over a range

$$\Delta x_o = \frac{\Delta\tilde{\delta}}{\Omega_{coh}} L + \frac{\Delta\omega_{det}}{\Omega_{coh}} x_d, \tag{5.7}$$

where $\Delta\tilde{\delta}$ and $\Delta\omega_{det}$ are the ranges of $\tilde{\delta}$ and ω_{det} observed in the search, and $L = .1294$ m and $x_d = 2.2$ m are the separation between the DSOF coils and the nozzle-detector distance respectively. In our experiment $\Delta\tilde{\delta}$ is set by the width of the Rabi plateaus described in Sec. 4.3.2, which limit the detunings we can achieve, while $\Delta\omega_{det}$ is determined by the finite frequency response of our hot wire detector.

As Eqs. 5.6, 5.7 show, the range of positions at which we can see AM is a function of Ω_{coh}. Hence, for fixed $\Delta\tilde{\delta}$, $\Delta\omega_{det}$, at low frequencies we can observe a wide range of modulation positions, while at higher frequencies this range is narrowed. An example of this phenomenon is our observation of the detector sampling rate (see Sec. 5.2.1), which acts like AM applied at the position of the detector wire. This modulation occurs at a frequency $\Omega_{coh} = 2\pi \times 10$ kHz, and at a position $x_o = 2.2$ meters away from the origin (source nozzle), but remains within our search range. At higher modulation frequencies, this signal would have fallen outside Δx_o.

5.3.2 Amplitude Modulation Index and Signal Contrast

The "simple amplitude modulator" of Sec. 2.2.4 can be employed to determine the percentage AM which our search could detect. An amplitude modulated wave can be written $|\psi_{out}(t)\rangle = [1 + m\cos(\omega'_m t)]\,|\psi_{in}(t)\rangle$ [103], and leads to a downstream detection probability

$$\begin{aligned}
\langle P_{TOT}\rangle_{time} &= \langle P_{AM} \times P_{DSOF}\rangle_{time} \\
&\simeq \left\langle [1 + 2m\cos(\omega'_m t)] \times \frac{1}{2}[1 + C_{DSOF}\cos(\frac{\tilde{\delta}L}{v} + \delta\frac{x_d}{v} - \delta t)]\right\rangle_{time} \\
&\simeq \frac{1}{2}\left[1 + mC_{DSOF}\cos\left((\omega'_m - \delta)t + \frac{\tilde{\delta}L}{v} + \delta\frac{x_d}{v}\right)\right], \qquad (5.8)
\end{aligned}$$

where the $\langle\rangle_{time}$ denotes an average over times of order $\frac{2\pi}{\omega'_m}$, C_{DSOF} is the contrast of the DSOF interferometer, and we have assumed[7] $m \ll 1.$, where m is the amplitude modulation index (which we will express as a percentage)

To relate this theoretical expression for the modulated atomic beam to the measured atomic signal, we note that Eq. 5.8 can generally be written

$$P_e = \overline{n}\,[1 + C_{signal}\cos(\omega_{det}t)], \qquad (5.9)$$

[7]This assumption is well justified for the very small amplitude modulation signals for which we search.

where C_{signal} is the contrast of the detected time-dependent excited state atom signal and $\overline{n}$ is the mean number of counts per sample of data and $\omega_{det} = \omega'_m - \delta$. Comparison of these two expressions yields

$$m = \frac{C_{signal}}{C_{DSOF}}. \tag{5.10}$$

Hence, determination of the contrast of the observed time-dependent atom signal downstream of the DSOF provides a direct measurement of the amount of amplitude modulation present in the beam.

5.3.3 Sensitivity to Non-AM ODEs

Our discussion of this experiment has implicitly assumed that the ODEs for which we search arise from amplitude modulation of the atomic beam originating in the neighborhood of the atom source—the most physically likely model for production of ODEs in our beam. It is useful, however, to discuss the sensitivity of our experiment to ODEs produced by less likely means. For example, as discussed in Sec. 5.3.1, AM originating from positions $x_o \neq 0$ can be detected by our search, subject to the restriction of the range given in Eq. 5.7. In addition, the presence of multiple sources of amplitude modulation (as described in Ch. 6) can create complicated density matrices exhibiting multiple, rather than single rephasing peaks. The altered widths of these peaks could, because of the average over $\tilde{\delta}$, change the sensitivity of our search. Finally, we note that a atomic beam which is phase modulated at the frequencies for which we search (Sec. 2.2.7) is not detectable unless the DSOF is positioned an appreciable fraction of the longitudinal Talbot length (1000's of meters for our experiment) downstream of the origin of the phase modulation.

5.4 Data Analysis

This section presents a detailed description of the data analysis procedures we employed for our ODE search, focusing in particular on the calibration of the sensitivity

of our search technique and the statistical analysis of the data. Together, these determine the limit on the amount of amplitude modulation which could have escaped our search.

5.4.1 Calibration

We employed a Lomb periodogram algorithm [100, 111, 112], to obtain a quasi-power spectrum of our time-dependent atom signal. This technique is superior to a standard FFT for finding small signals in the data, which is unevenly spaced in time because our data acquisition electronics caused an unpredictable delay (average of 0.025 msec) between the 0.075 msec long samples. To calculate the sensitivity of the periodogram to a known amplitude modulation of the beam, we must determine how the periodogram peak height P depends on the signal contrast. For a time-dependent signal composed of a single sinusoidal frequency and Gaussian noise with variance $\sigma_{noise} = \sqrt{\overline{n}}$, the periodogram peak height is [112]

$$P(C, \overline{n}) = \frac{N_o}{2}\left(1 + \frac{2}{C^2\overline{n}}\right)^{-1} \tag{5.11}$$

where N_o is the number of samples of data, C is the signal contrast, and $\overline{n}$ is the mean number of counts per sample.

This simple theoretical prediction, however, provides only limited agreement with the measured periodogram peak heights, because for small $\overline{n}$ the noise in our data is Poissonian (shot noise) rather than Gaussian, and because the numerical algorithm used to compute the periodogram is not identical to a true Lomb periodogram in all respects. We therefore opted to empirically verify the form of $P(C, \overline{n})$ by generating simulated data at a wide variety of values of C and $\overline{n}$ and calculating $P(C, \overline{n})$ in each case. The results of this simulation are shown in Fig. 5-5. This figure also shows the results of a two dimensional fit to the function

$$P'(C, \overline{n}) = A + BC^2\overline{n}, \tag{5.12}$$

(equivalent to Eq. 5.11 for small $C^2\overline{n}$) where A, B are constants, for which we found

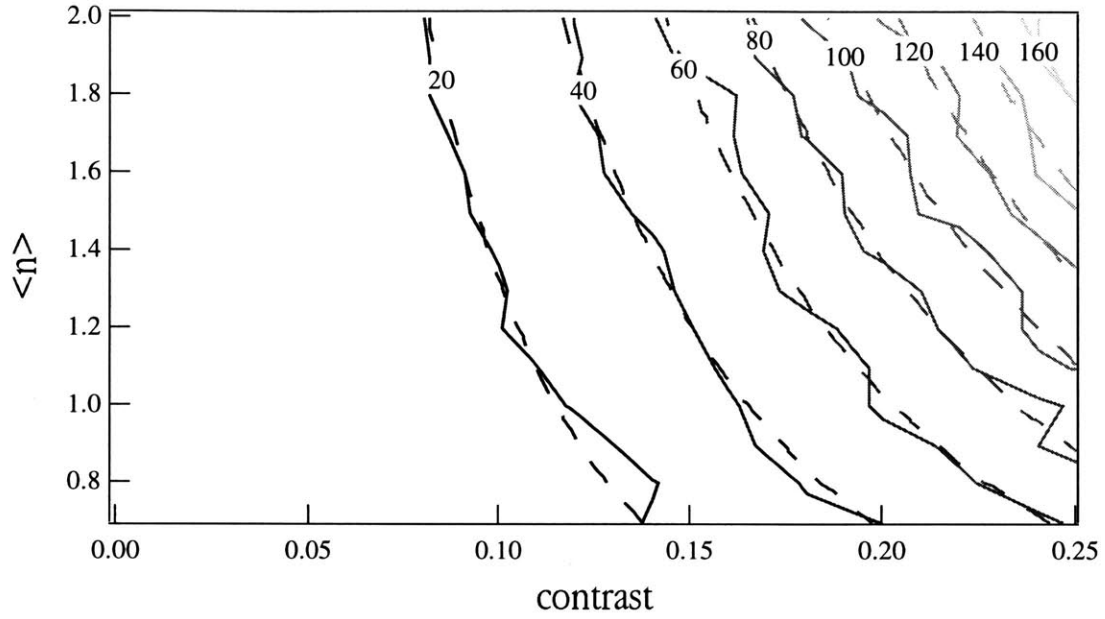

Figure 5-5: Contour plot of periodogram peak height vs contrast and mean counts/sample. Solid lines: simulated data. Dashed lines: fit to Eq. 5.12.

$A = 1.08 \pm .29$, $B = 1426.2 \pm 6.5$.

To determine $P(C, \overline{n})$ for true (rather than simulated) time-dependent data—which had slightly reduced P's due to the presence of extra noise in our measured signal—we took a set of calibration data to relate the measured signal contrast to the peak height of the periodogram. A resonant π pulse was applied to one of the two DSOF coils, transferring population from the $|1,0\rangle$ to the $|2,0\rangle$ state. A variable amplitude modulation was then applied to the incoming $|1,0\rangle$ state by an upstream AM coil (see Fig. 4-4) driven by the modulator circuit shown in Fig. 4-6, producing a downstream time-dependent atom signal given by the square of the wavefunction of Eq. 4.2 [68]. The modulation frequency was first set to a relatively low value ($\omega_m = 2\pi \times 300$ Hz) and time resolved data were acquired (see Fig. 5-6). A fit to this time-dependent data determined the parameter $\theta_o = \frac{\omega_R l}{v}$, which in turn was used to determine the contrast of the rephased fringes [68].

The modulation frequency was then increased (*without* changing the power applied to the AM region, and hence without changing the expected contrast of the rephased atom signal) producing a high frequency signal at $2\omega_m = 2\pi \times 50.008$

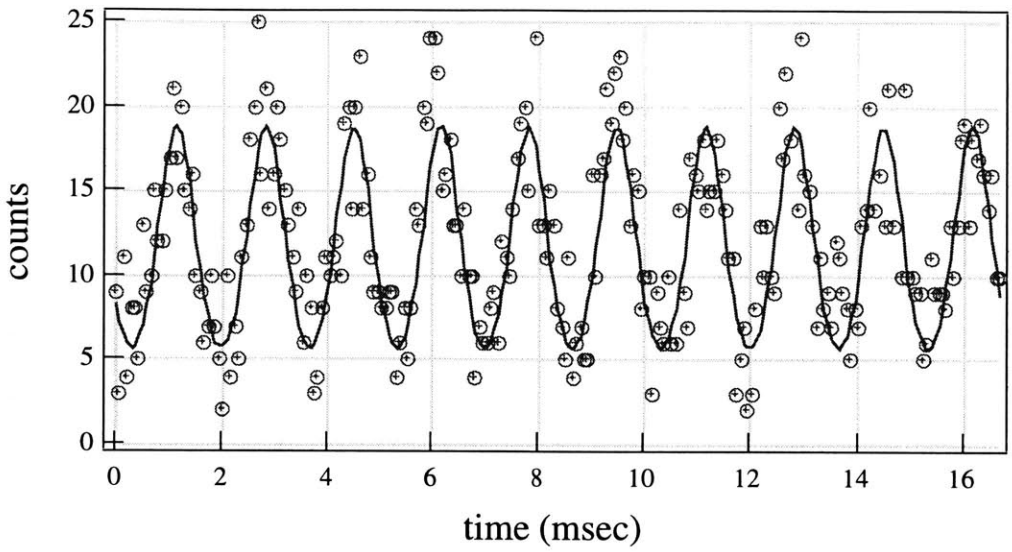

Figure 5-6: Time-dependent data for determining the contrast of the calibration amplitude modulation. Markers: data. Solid line: fit to absolute value squared of Eq. 4.2. The fit yields $\theta_o = \frac{\omega_R l}{v_o} = 1.01 \pm 0.02$, and a corresponding contrast [68] of $0.29 \pm .02$ for the rephased signal downstream of the DSOF.

kHz. The DSOF interferometer heterodyned and rephased this signal, generating time-dependent Ramsey fringes (Sec. 2.2.5) which were processed with the Lomb periodogram algorithm. This procedure was repeated for five different values of the AM coil power, and hence for five different values of C and $\overline{n}$. To achieve the best possible agreement with the calibration points, the peak height predicted by Eq. 5.12 was rescaled

$$\begin{aligned} P(C,\overline{n}) &= \alpha \times P'(C,\overline{n}) \\ &= \alpha\left(A + BC^2\overline{n}\right), \end{aligned} \tag{5.13}$$

where $\alpha = 0.658 \pm .002$ is a scale factor obtained from a fit of Eq. 5.13 to the experimentally measured calibration points.

To determine the dependence of the measured atom signal contrast on the periodogram peak height P and mean count rate $\overline{n}$, we invert Eq. 5.13 and write

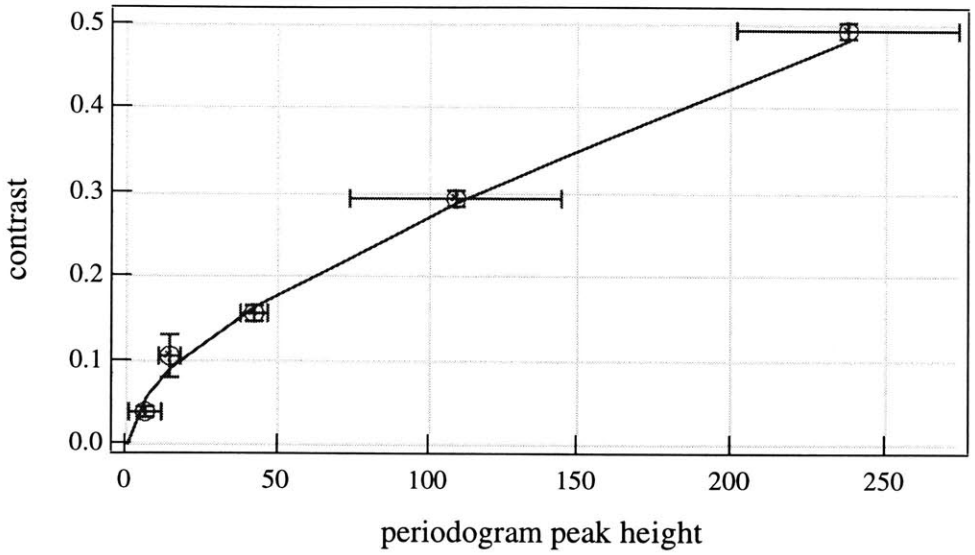

Figure 5-7: Periodogram peak height as a function of contrast and mean counts/sample. Markers are data, with error bars obtained from the statistics of the measured periodogram peak heights and contrasts. Solid line: prediction of Eq. 5.14.

$$C(P,\overline{n}) = \sqrt{\frac{1}{B\overline{n}}\left(\frac{P}{\alpha} - A\right)}. \tag{5.14}$$

Figure 5-7 shows a comparison of Eq. 5.14 with the calibration data.

5.4.2 Data Acquisition

As discussed in Sec. 5.2 we collected ~ 0.6 sec of data for each δ, $\tilde{\delta}$ value in our search range. We first obtained the periodogram for each of these δ, $\tilde{\delta}$ points, and then averaged together spectra from four identically collected data sets. A contour plot of a planar slice of the resulting distribution $P(\delta, \tilde{\delta}, \omega_{det})$ for a single value of δ is shown in Fig. 5-2 for the case of $\delta = 2\pi \times 49$ kHz for a known 5.3% amplitude modulation of the beam.

The existence of ODEs produced by amplitude modulation is revealed by the presence of rephasing peaks in the $\tilde{\delta}$, ω_{det} planes. The $\tilde{\delta}$ positions of these peak are determined by Eq. 5.6, and their average width of $2\pi \times 32$ kHz (governed by the velocity width of the atomic beam) was measured by fitting a Gaussian to "slices" of $P(\delta, \tilde{\delta}, \omega_{det})$ with fixed δ and ω_{det} (see Fig. 5-8). To take advantage of this $\tilde{\delta}$

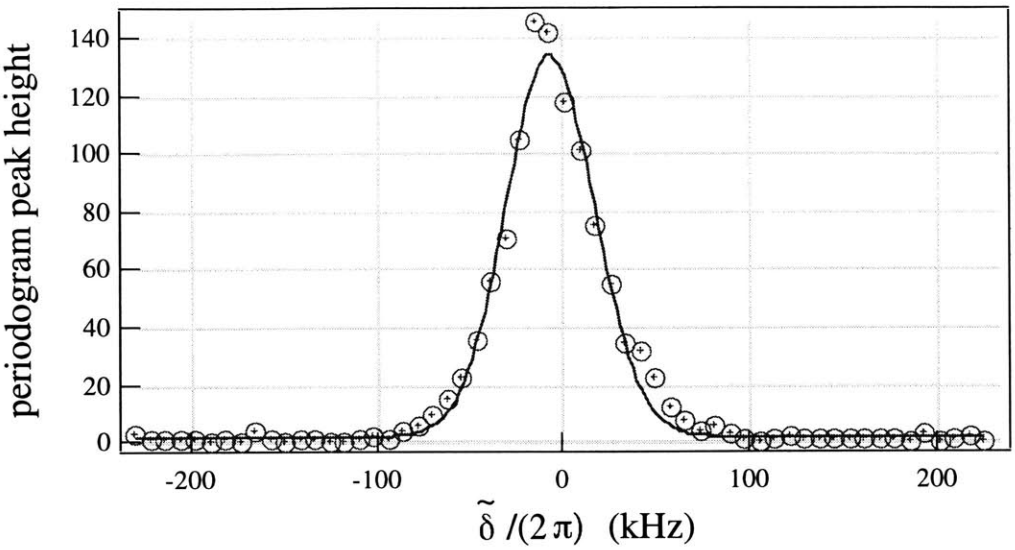

Figure 5-8: Rephasing peak plotted as a function of $\tilde{\delta}$. Markers: data. Solid line: fit. The fit determined that the rms of this peak is $2\pi \times 33.8 \pm .8$ kHz. The average width determined from many such fits is $2\pi \times 32.4$ kHz.

width, we boxcar averaged $P(\delta, \tilde{\delta}, \omega_{det})$ along $\tilde{\delta}$ with a window size of $2\pi \times 40$ kHz. This averaging process, while it reduced the peak height to 0.88 of its original value, reduced the noise by $\sqrt{6}$, doubling the signal/noise.

To simplify our analysis, as well as to provide a compact representation of our search data over the entire Ω_{coh} range, we selected the *highest* value of $P(\delta, \tilde{\delta}, \omega_{det})$ along the $\tilde{\delta}$ axis, obtaining $P_{max}(\delta, \omega_{det})$. This analysis step has an important statistical implication: if P happened to fluctuate low (a possible consequence of the Gaussian distribution of the measured peak height about its average value) the selection of the highest value of P for a given δ, ω_{det} means that this low peak was replaced by a value that is *at least as high.* This process can only increase the value of P we retain and decrease its variance, hence it did not cause us to miss or underestimate the size of any small peaks.[8]

In our final analysis step, we exploited the fact that any real signal with a particular value of Ω_{coh} would produce rephasing peaks in $P_{max}(\delta, \omega_{det})$ curves for which $|\delta - \Omega_{coh}| < 2\pi \times 3$ kHz, the maximum detector response frequency. Since our detector

[8]The price we pay for performing our subsequent analysis on $P_{max}(\delta, \omega_{det})$ rather than on $P(\delta, \tilde{\delta}, \omega_{det})$ is an increase in the final noise level of the data.

cannot distinguish between positive and negative frequencies, there is an ambiguity about whether a particular peak arises from AM at either $\Omega_{coh} = \delta + \omega_{det}$ or $\delta - \omega_{det}$. We resolved this ambiguity by mapping each $P_{max}(\delta, \omega_{det})$ to both of its possible Ω_{coh} values, $\delta \pm \omega_{det}$. We then averaged together the resulting curves for five neighboring values of δ, producing a final distribution $P_{ave}(\Omega_{coh})$ (Fig. 5-4b). We note that while the falloff in detector frequency response (Sec. 4.1.2) reduces the average peak height by a factor of 0.89, our signal/noise is approximately doubled by this process.[9]

The signal/noise increases derived in this section assume a Gaussian distribution of individual P points about their mean value. A statistical analysis of the P's obtained for 20 identical data files with a known applied AM found P to be roughly Gaussian distributed and verified that the rms width of the distribution obeyed

$$\sigma_P = \frac{\sigma_{Po}}{\sqrt{N}}, \tag{5.15}$$

where σ_{Po} is the variance of a single P measurement and σ_P the variance of P determined by an average of N P measurements—consistent with standard Gaussian statistics [113]. In the calculation of our instrument response function (Sec. 5.4.4), where we required an exact value of σ_{Po} to determine the confidence level of the search, we employed $\sigma_{Po} = 2.47$, the value obtained for the smallest visible AM signal.[10]

5.4.3 Establishing a Confidence Level

The noise level of P_{ave} determines the smallest amplitude modulation m that our search data can conclusively demonstrate is *not* present in the beam. We increased our search sensitivity by removing all possible noise.

The principal noise in our experiment occurred at $\omega_{det} = 2\pi \times 60$, 120 Hz, and can be attributed to fluctuations in the current supplied to the second Stern-Gerlach magnet, which caused time-dependent deflection of the beam and hence modulation

[9]The large peak at $\Omega_{coh} = 2\pi \times 10$ kHz, as well as its images at $2\pi\times$ 6, 8 kHz, are caused by the spurious time-dependence imposed by the sampling rate of our data acquisition electronics (as discussed in Sec. 5.2).

[10]Since we found that σ_{Po} was approximately linear in P, this is a conservative (i.e. slightly high) estimate of the variance, so our true confidence level may be fractionally higher.

of the beam intensity measured by the detector wire. The beat frequency of the DSOF itself produced large time-dependent signals at $\omega_{det} = 2\pi\times$ 1, 2, and 3 kHz for data with $\delta = 2\pi\times$ 1, 2, and 3 kHz respectively, as well as sidebands (produced by the interaction of the beat signals with the SG magnet noise) spaced $2\pi\times$ 60, 120 Hz away from these frequencies. Finally the power spectra contained low frequency fluctuations, with $\omega_{det} = 0$ to $\sim 2\pi \times 15$ Hz, which we attributed to $\frac{1}{f}$ noise.

We removed all noise peaks from $P_{max}(\delta, \omega_{det})$, replacing them with $\overline{P_{max}}$, the average level of P_{max}. Over a typical ω_{det} range, only $\sim 0.5\%$ of the data were replaced in this fashion. Moreover, since each $P_{ave}(\Omega_{coh})$ point arises from averaging together multiple $P_{max}(\delta, \omega_{det})$ values, this noise elimination process results in a reduction of the signal/noise of our search at values of Ω_{coh} to which noise peaks contribute, rather than complete "blindness" at these frequencies.

After performing the preliminary noise elimination and averaging $P_{max}(\delta, \omega_{det})$ curves to produce $P_{ave}(\Omega_{coh})$, we continued the noise reduction process by creating a histogram of the values of P_{max}. Study of this histogram allowed us to identify and remove several noise peaks caused by extra $\frac{1}{f}$ noise at frequencies from $2\pi \times$ 15-20 Hz that were not removed by our earlier analysis. The righthand edge of the resulting histogram (Figs. 5-9, 5-10) defines P_{cutoff}, the smallest value of P_{ave} at which our source search could discern the presence of a true AM coherence, and hence sets the limit to the sensitivity of our search.

The "confidence level" of our search is the percentage chance that a particular value of P_{ave} is measured to be greater than P_{cutoff}, and hence was detectable by our search, despite the possibility of Gaussian distributed fluctuations of this quantity about its average value. For example, the confidence level for $P_{ave} = P_{cutoff}$ is 50%—that is, there is a 50% chance that a signal with an average value of P_{cutoff} will, when measured, fall above P_{cutoff}.

To indicate the thoroughness of our search, we calculated a P_{ave} corresponding to a 99% confidence level: the value P_{conf} such that there is only a 1% chance that a statistical fluctuation could have lead to a measurement of P_{ave} less than P_{cutoff}. We determined this quantity by employing the estimated variance $\sigma_P = 0.247$ of

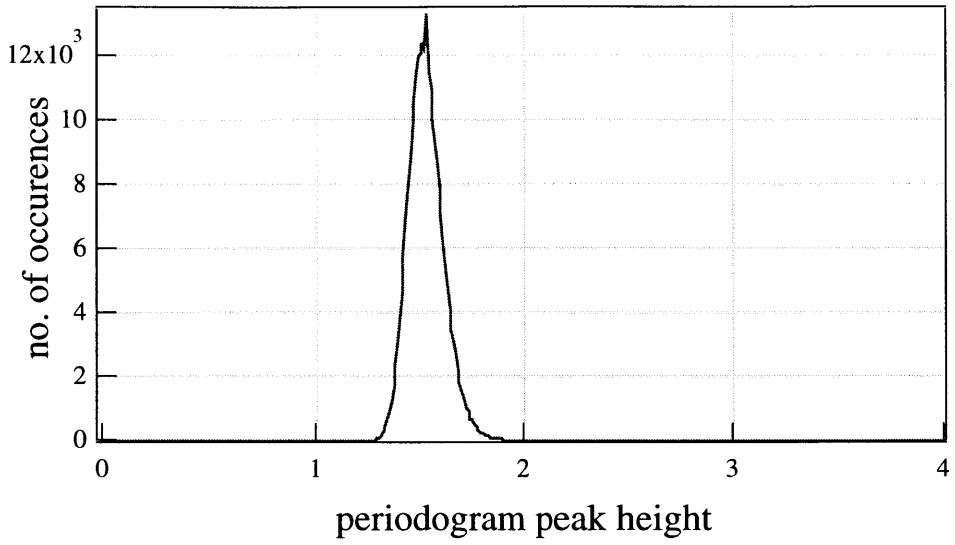

Figure 5-9: Histogram of periodogram peak heights for the search data, $P_{ave}(\Omega_{coh})$.

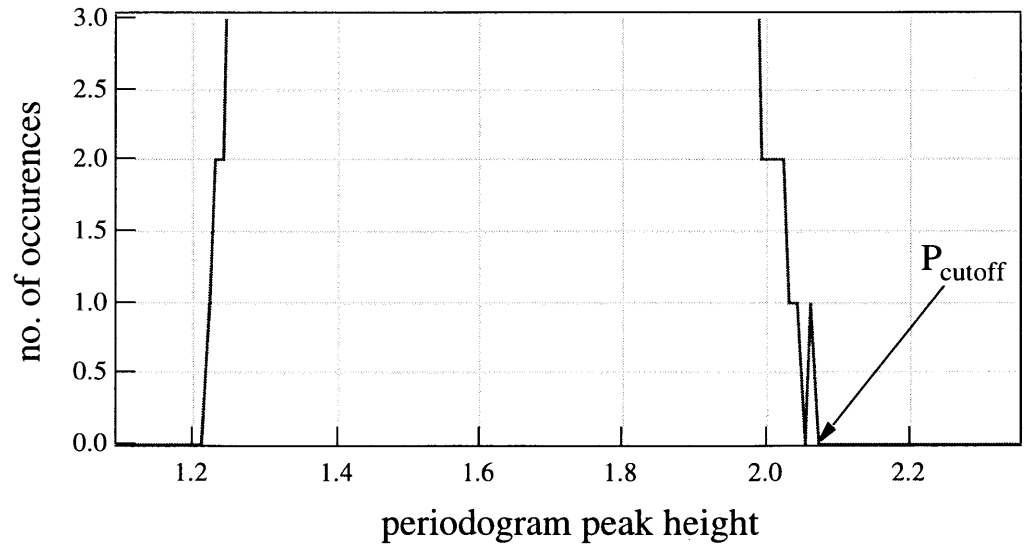

Figure 5-10: Close-up of histogram of periodogram peak heights for the search data, $P_{ave}(\Omega_{coh})$. P_{cutoff}, the level below which our search cannot detect a peak, is found at $P_{ave} = 2.07$. For clarity, the peaks due to the detector sampling rate are not shown.

P_{ave}, which is given by Eq. 5.15 with $N = 100$ (see footnote[11]). The Gaussian statistics of the periodogram peak height [113] lead to the result that for $P_{conf} = P_{cutoff} + 2.5 \times \sigma_P = 2.69$, the confidence level is greater than 99%.

5.4.4 Instrument Response

The amplitude modulation index m is related to the measured signal contrast C_{signal} (Eq. 5.10), which is in turn related to the periodogram peak height (Eq. 5.14). To determine the final sensitivity of our experiment we calculated the instrument response function $m(\Omega_{coh})$, the minimum amplitude modulation which our search could detect. However, the parameters C_{DSOF} and $\overline{n}$ are not constant over the range of the search because for large δ, $\tilde{\delta}$ the DSOF coil detunings $\delta_{1,2}$ fall outside the region over which the "power boost" technique (see Sec. 4.3.2) can maintain perfect $\frac{\pi}{2}$ pulse conditions, leading to a decrease in $|2,0\rangle$ atoms.

We accounted for the effect of the power boost on the mean count rate per sample by directly determining $\overline{n}$ for all the data samples obtained in the search. We inferred the expected DSOF interferometer contrast as a function of δ, $\tilde{\delta}$ from the measured Rabi profiles of Sec. 4.3.2. Contour plots of $C_{DSOF}(\delta, \tilde{\delta})$ and $\overline{n}(\delta, \tilde{\delta})$ are shown in Figs. 5-12, 5-11 respectively.

We used the least sensitive regions of these quantities to calculate $C(\Omega_{coh})$, $\overline{n}(\Omega_{coh})$ (the dependence of the contrast and mean counts/sample on the modulation frequency) from $C_{DSOF}(\delta, \tilde{\delta}_{max})$ and $\overline{n}(\delta, \tilde{\delta}_{max})$, where $\tilde{\delta}_{max}$ is the largest value value of $\tilde{\delta}$. Averaging the resulting expressions over neighboring δ points to model the dependence of each P_{ave} point on multiple $P_{max}(\delta, \omega_{det})$ values, we calculated the $C(\Omega_{coh})$, $\overline{n}(\Omega_{coh})$, displayed in Fig. 5-13.

Employing $C(\Omega_{coh})$, $\overline{n}(\Omega_{coh})$ in Eqs. 5.10 and 5.14 we obtained the instrument response function of our search

[11] We note that $N = 100$ because each P_{ave} point consists of an average of 4 initial periodograms scans, a boxcar average over 5 $\tilde{\delta}$ values, and an average of 5 $P_{max}(\delta, \omega_{det})$ points.

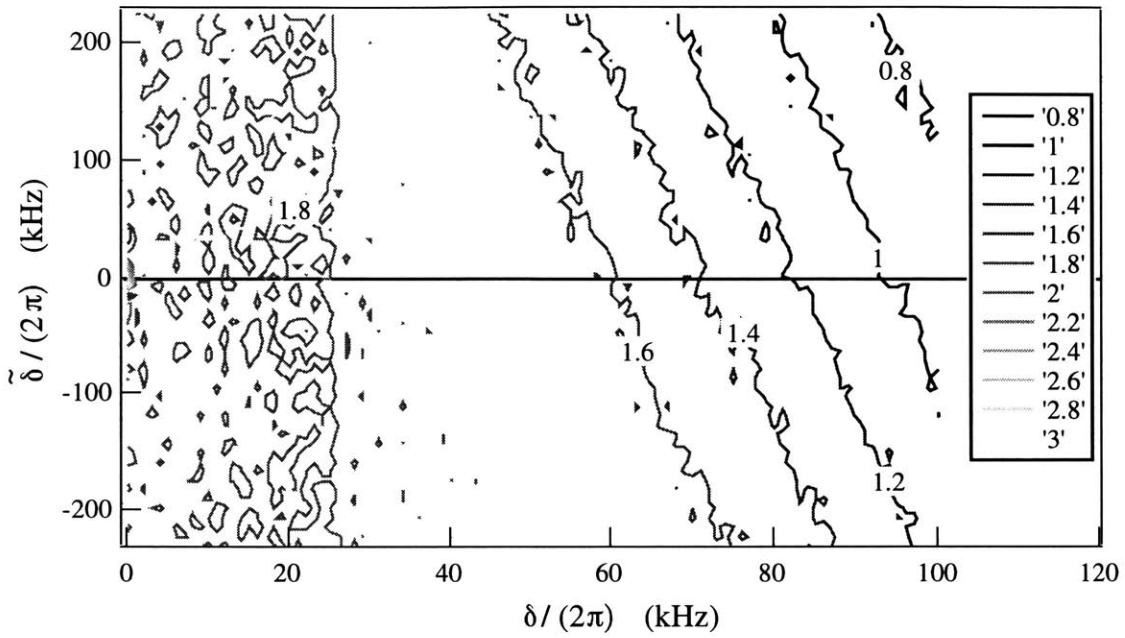

Figure 5-11: Contour plot of mean counts/sample (determined directly from data samples) over the full δ, $\tilde{\delta}$ range of the search.

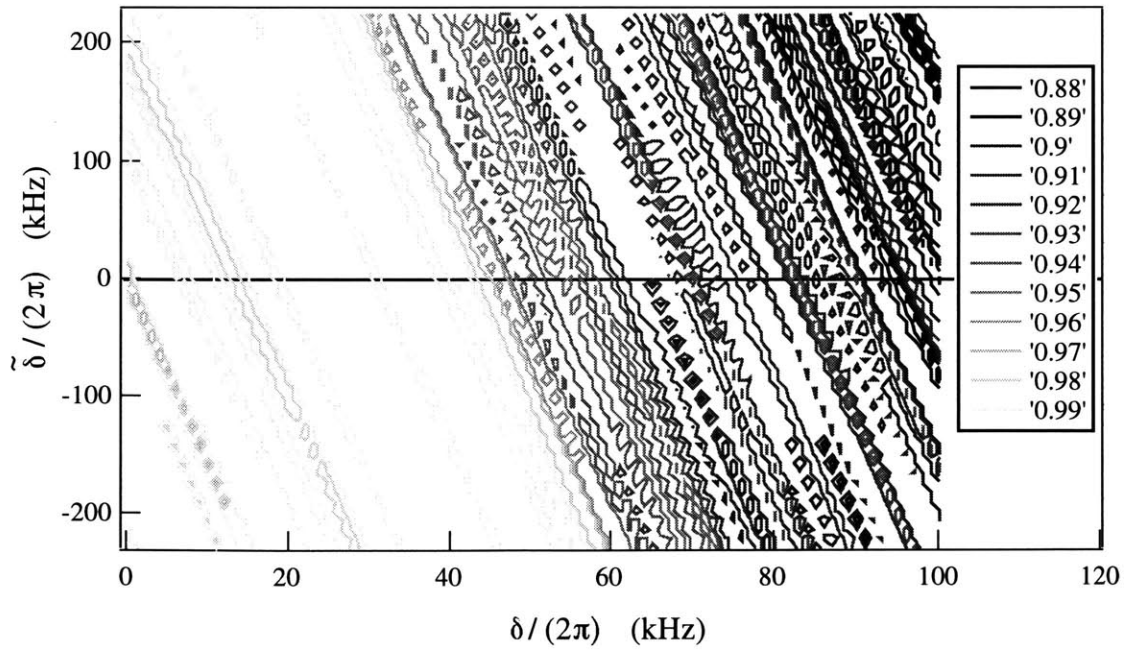

Figure 5-12: Contour plot of contrast (inferred from Rabi plateaus) over the full δ, $\tilde{\delta}$ range of the search.

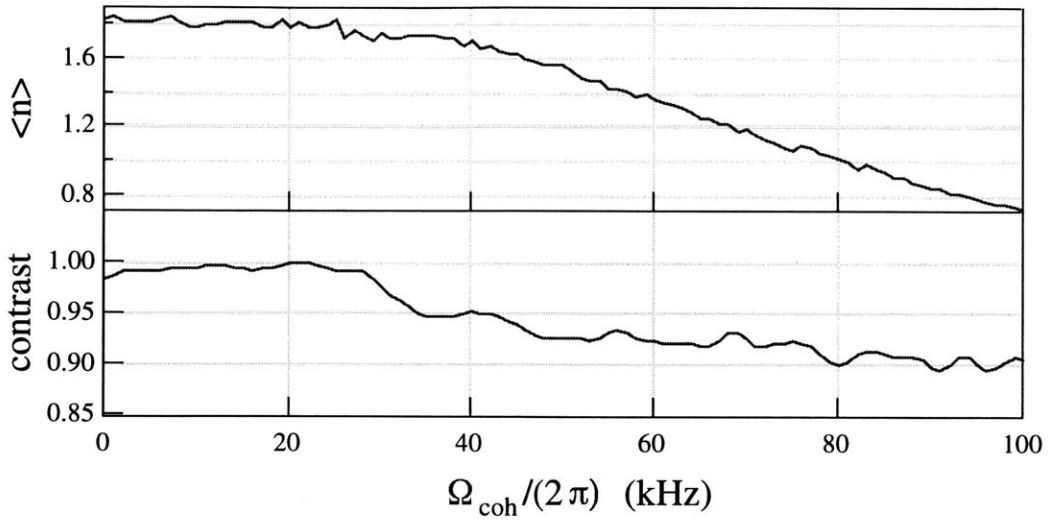

Figure 5-13: Mean counts/sample and contrast as a function of Ω_{coh} over the range of the search. Mean counts and contrast are highest for low Ω_{coh}, where the DSOF coils can apply perfect $\frac{\pi}{2}$ pulses, but fall off for higher frequencies.

$$m(\Omega_{coh}) = \frac{1}{C_{DSOF}(\Omega_{coh})} \times \sqrt{\frac{1}{B\overline{n}(\Omega_{coh})}\left(\frac{P'_{conf}}{\alpha} - A\right)}, \tag{5.16}$$

where $P'_{conf} = \frac{P_{conf}}{.88\times.89}$ is the P_{ave} value (rescaled to take into account the reduction in peak height caused by averaging over both $\tilde{\delta}$ and the detector frequency response as discussed in Sec. 5.4.2) associated with 99% confidence level.

The instrument response function for 99% confidence is displayed in Fig. 5-14 along with the analogous result for the 50% confidence level, in which P_{conf} is replaced by P_{cutoff}. Our search is most sensitive ($m = 4\%$) for low Ω_{coh}'s, where the power boost technique allowed the application of perfect $\frac{\pi}{2}$ pulses to the two DSOF coils. For higher frequencies, the falloff in $\overline{n}$ and C_{DSOF} lead to reduced sensitivity, reaching $m = 7\%$ at $\Omega_{coh} = 2\pi \times 100$ kHz.

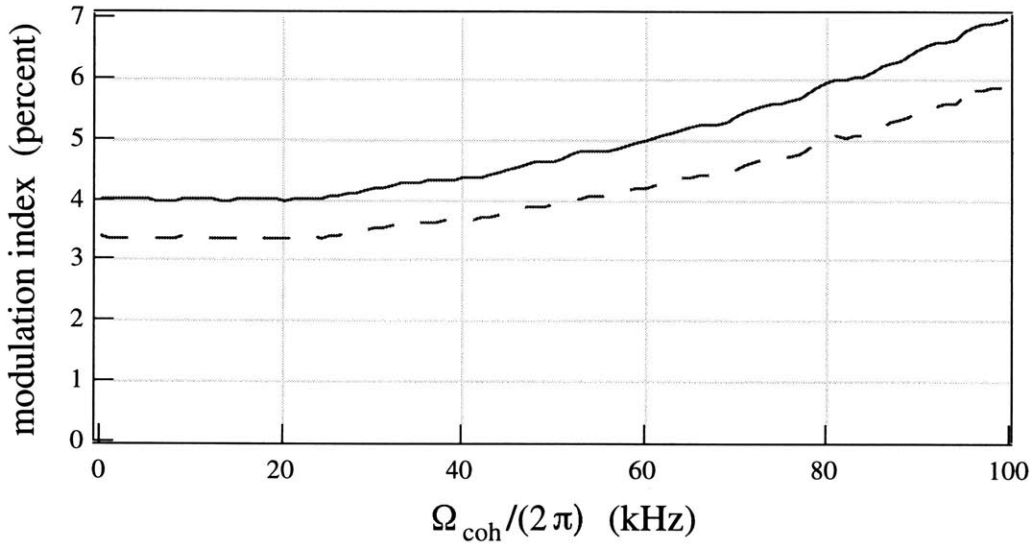

Figure 5-14: Amplitude modulation index m which our search technique could detect. Solid line: 99% confidence. Dashed line: 50% confidence.

Chapter 6

Deconvolving the Density Matrix of a Longitudinally Modulated Atomic Beam

This chapter discusses the first experimental measurement of the longitudinal energy/momentum density matrix of a matter wave beam with non-trivial structure both along and off the diagonal. A brief introduction to the experiment is provided, followed by a draft of a paper, "Measurement of the Density Matrix of a Longitudinally Modulated Atomic Beam," to be submitted to Physical Review Letters. The final sections of the chapter present theoretical and experimental details relevant to this work, focusing on the novel "double AM" density matrix studied in our experiment.

6.1 Introduction to Deconvolution Experiment

The field of quantum state measurement has made impressive advances over the last five years, as evidenced by the demonstration of optical homodyne tomography for measuring the density matrix of a light mode [34], as well other experiments concerning the quantum states of molecular vibration [35] and trapped ions [36]. A number of theoretical papers have proposed ways to measure the quantum state of

both the transverse [37, 38, 39, 40, 114], and longitudinal [81, 94, 98] degrees of freedom of atoms in an atomic beam. In a recent experiment Mlynek *et al.* [41] demonstrated a tomographic reconstruction of the Wigner function of the transverse degree of freedom of an atomic beam. However, until now no experiment has measured an atomic beam's longitudinal quantum state.

Building upon our recently demonstrated search for longitudinal coherence (Ch. 5), we present the first experimental determination of the longitudinal energy density matrix of an atomic beam possessing complicated structure both along and off the diagonal. Our experiment employs the DSOF interferometer described in Ch. 2 (which can overlap initially different plane wave components, allowing study of their amplitude and relative phase), along with the coherent deconvolution technique of Ch. 3, which uses Fourier transforms of sets of rephased Ramsey fringes to measure the density matrix.

The density matrix we study in this experiment is produced by the application of two successive amplitude modulation (AM) regions (see Sec. 2.2.4), whose time-dependent modulation of the beam generated the off-diagonal density matrix structure. The two synchronously driven AM regions also act as velocity or energy selectors, and therefore produce structure parallel to the diagonal of the density matrix.

To test the accuracy of our deconvolution experiment, we compared the amplitude and phase of the experimentally determined density matrix with theoretical predictions for these quantities calculated for our experimental conditions.

6.2 Paper: Measurement of the Density Matrix of a Longitudinally Modulated Atomic Beam

Richard A. Rubenstein, David A. Kokorowski, Al-Amin Dhirani, Tony D. Roberts, Subhadeep Gupta, Jana Lehner, Winthrop W. Smith,[1] Edward T. Smith, Herbert J. Bernstein,[2] and David E. Pritchard

Massachusetts Institute of Technology,

Cambridge, Massachusetts 02139

Abstract

We demonstrate the first experimental measurement of the longitudinal energy/momentum density matrix of an atomic beam with complex structure along and off the diagonal. We produced this novel density matrix with two amplitude modulators and detected it with a longitudinal atom interferometer. We compare our experimentally determined density matrix with a theoretical prediction.

PACS: 03.75.Bc,03.75.Dg,39.20.q

The determination of the density matrix, or equivalently the Wigner function, of an ensemble of identically prepared particles has long been a subject of interest in quantum measurement theory [30, 31, 33], because such distributions contain the most complete possible description of the quantum state of the system. Recent experiments in this rapidly advancing field have measured the density matrix and/or Wigner function of photon states [34], the vibrational mode of a diatomic molecule [35], and trapped ions [36], as well as the Wigner function for the transverse degree of freedom for atoms in a beam [41]. In a previous paper [69], we searched for non-zero off-diagonal density matrix elements (in the longitudinal energy/momentum basis) produced by a supersonic atomic beam source, placing an upper bound on their possible size. In this Letter, we present the first experimental measurement of the longitudinal energy density matrix of a matter wave beam possessing complicated

[1]Present Address: Physics Department, University of Connecticut U-46, 2152 Hillside Road, Storrs, CT, 06269.

[2]Present Address: Hampshire College and Institute for Science and Interdisciplinary Studies, Amherst, Massachusetts 01002.

energy dependence both along and off the diagonal.

Study of the longitudinal density matrix presents several challenges. The intrinsic time-dependence of off-diagonal matrix elements [69] requires a time-dependent technique to measure them. In addition, the vacuum dispersion relation $\hbar\Omega = (\hbar k)^2/(2m)$ for matter waves, along with the finite energy spread of available beams, leads to dephasing which washes out the amplitude modulated atomic probability caused by the presence of off-diagonal matrix elements [68, 99]. Our deconvolution technique [81] is based on a longitudinal interferometer employing two differentially detuned oscillatory field regions (DSOF [68]). It can heterodyne down high frequency off-diagonal density matrix elements to more easily detectable low frequencies and can impart a momentum dependent phase shift [81, 94, 98] to reverse the effect of energy/momentum dephasing.

In this paper we demonstrate this deconvolution scheme for the first time, using it to measure a novel density matrix created by placing two successive amplitude modulated (AM) oscillatory field regions in the beam path, as shown in Fig. 6-1.

In our experiment an incident Na beam [68, 69] was first state selected by a two-wire Stern-Gerlach magnet, which transmitted only the $|F = 1, m_F = 0\rangle$ state. Two narrow longitudinal oscillatory magnetic field regions separated by $L_c = 11.4$ cm were synchronously driven by an amplitude modulated radiofrequency signal with a modulation frequency $\omega_m = 2\pi \times 60.9$ kHz and carrier frequency $\omega_c = 2\pi \times 7.65$ MHz. These regions transferred population from the initial $|1,0\rangle$ state to (and from) the $|1,1\rangle$ and $|1,-1\rangle$ states.

Solving the three-state resonance problem for the initial plane wave $e^{i(k_o x - \Omega_o t)}\,|1,0\rangle$ propagating through the two AM regions,[3] we find the amplitude modulated $|1,0\rangle$ state wavefunction downstream of the second AM region,

[3]The applied transverse guide field ($\sim$ 10 Gauss) was sufficiently small that we could neglect the quadratic term in Zeeman energy, so the $|1,0\rangle \rightarrow |1,1\rangle$ and $|1,0\rangle \rightarrow |1,-1\rangle$ transitions had equal resonance frequencies.

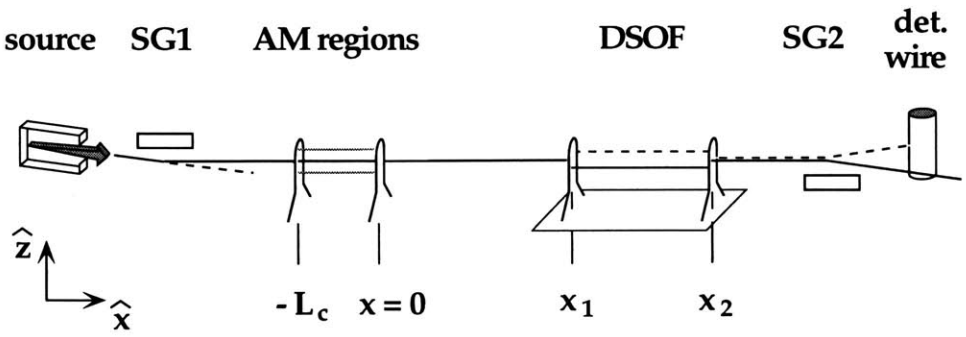

Figure 6-1: A schematic of the apparatus. The atomic beam emerges from the source and is state selected by Stern-Gerlach magnet SG1. The resulting $|1,0\rangle$ state beam (solid line) travels through AM regions at $x = -L_c$ and $x = 0$, which drive transitions to the undetected $|1,\pm1\rangle$ states (dotted lines). Oscillatory field regions at $x_{1,2}$ with frequencies $\omega_{1,2}$ drive energy and hyperfine state changing transitions, forming the DSOF interferometer. The $|2,0\rangle$ state (dashed line) is selected by a second Stern-Gerlach magnet SG2 and detected by a scanning Re hot wire.

$$
\begin{aligned}
|\psi(x,t)\rangle \;=\; & \Big\{\cos\Big[\theta_1 \sin\left(\omega_m\left[x/v-(t-L_c/v)\right]\right)\Big]\;\cos\Big[\theta_2 \sin\left(\omega_m\left[x/v-t\right]\right)\Big] \\
& -\cos\phi_B\;\sin\Big[\theta_1 \sin\left(\omega_m\left[x/v-(t-L_c/v)\right]\right)\Big] \\
& \times \sin\Big[\theta_2 \sin\left(\omega_m\left[x/v-t\right]\right)\Big]\Big\}\, e^{i(k_o x-\Omega_o t)}\;\;|1,0\rangle\,,
\end{aligned}
\tag{6.1}
$$

where v is the atomic velocity, $\theta_i = \left(\frac{\omega_{Ri} l_i}{v}\right)$, ω_{Ri} is the Rabi frequency, and l_i the length of the ith AM region, and

$$
\pm\,\phi_B(z) = \pm\left(\frac{\mu_o}{2\hbar v}\int_0^{L_c} B(x,z)\,dx - \frac{\omega_c\, L_c}{v}\right). \tag{6.2}
$$

The first term in Eq. 6.2 denotes the relative phase evolved between the $|1,0\rangle$ and the $|1,\pm1\rangle$ components in traveling between the AM regions, while the second denotes the phase acquired by the oscillatory field during this interval.

The amplitude modulated wavefunction of Eq. 6.1 possesses an infinite ladder of energy/momentum sidebands [68], and leads to an energy basis density matrix

$$\begin{aligned}\rho(\Omega', \Omega' + \Omega_{coh}, t) &= \overline{\langle \Omega' + \Omega_{coh} | \psi \rangle \langle \psi | \Omega' \rangle} \\ &= \rho_o(\Omega', \Omega' + \Omega_{coh}) e^{i\Omega_{coh}(t-t_o)} \end{aligned} \tag{6.3}$$

which has non-zero elements at $\Omega_{coh} = 2n\omega_m$ for integer n, where Ω_{coh} is the off-diagonal coordinate. The overbar in Eq. 6.3 denotes an ensemble average over the atoms in the beam, which must take into account both an average over all atomic velocities and over all possible trajectories through the two AM regions. Variations in magnetic field B with the vertical coordinate z between the two AM regions caused the phase ϕ_B in Eqs. 6.1, 6.2 to vary over more than 2π, destroying the internal state coherence between the $|1,0\rangle$ and $|1,\pm 1\rangle$ levels.

6.2.1 Measuring the Density Matrix

To explain our DSOF interferometer [68] deconvolution scheme, we consider a density matrix of the form of Eq. 6.3, which contains two plane wave components with energy difference $\hbar\Omega_{coh}$ in the $|1,0\rangle$ internal state. This beam emerges from the second AM region at $x = 0$ (see Fig. 6-1) and propagates through two differentially detuned radiofrequency separated oscillatory field (DSOF) regions located at x_1 and $x_2 = x_1 + L$, where RF magnetic fields of frequency $\omega_{1,2}$ drive $|1,0\rangle \rightarrow |2,0\rangle$ hyperfine transitions with resonance frequency $\omega_{hf} = 2\pi \times 1772$ MHz. The beam then propagates through a state selecting magnet, and the $|2,0\rangle$ state is detected at x_d. This configuration is a longitudinal interferometer, in which the frequency component Ω' excited by ω_1 and the $\Omega' + \Omega_{coh}$ component excited by ω_2 can interfere, producing a time-dependent beat at the detector with frequency $\Omega_{det} = \delta - \Omega_{coh}$, where

$$\delta = \omega_1 - \omega_2. \tag{6.4}$$

We obtain the density matrix by measuring $P_2(\delta, \tilde{\delta}, t)$, the total probability that an atom will reach the detector in the $|2,0\rangle$ state after passing through the double AM

and the DSOF (which includes ensemble averages over trajectories and over the initial energy distribution of the atomic beam) where we have defined the scaled detuning

$$\tilde{\delta} = \frac{\omega_2 x_2 - \omega_1 x_1}{L} - \omega_{hf}. \tag{6.5}$$

For the case of our fast atomic beam [81], the double Fourier transform of $P_2(\delta, \tilde{\delta}, t)$ (once with respect to time and once with respect to $\tilde{\delta}$) determines the complete density matrix:

$$\rho_o\left(\Omega', \Omega' + \Omega_{coh}\right) = A \int d\tilde{\delta}\, e^{-i\tilde{\delta}b/\sqrt{\Omega'}} \int dt\; P_2(\delta, \tilde{\delta}, t)\, e^{-i(\delta - \Omega_{coh})t}, \tag{6.6}$$

where the constants A and b are defined in Ref. [81]. Since a full set of $P_2(\delta, \tilde{\delta}, t)$ data overdetermines the density matrix, we choose for convenience to set $\delta = \Omega_{coh}$ for each non-zero $\rho(\Omega', \Omega' + \Omega_{coh})$ in our experiment.

The extremely large kinetic energy of our beam relative to the energy shifts applied by the AM regions and the DSOF ($\Omega_o \gg \omega_m, \delta$) means that a semiclassical approximation provides a physically intuitive picture of our deconvolution scheme. In this limit, which corresponds to a wave mechanical near field approximation [99], the quantum wave equation leads to solutions in which atoms follow ray-like classical trajectories, but with quantum evolution of the internal states. Thus, the detection probability $P_2(\delta, \tilde{\delta}, t)$ is the ensemble averaged product of the double AM transmission probability P_{AM} (absolute value squared of Eq. 6.1 averaged over ϕ_B) and the DSOF transmission probability P_{DSOF} (calculated in Ref. [99]):

$$\begin{aligned} P_2(\delta, \tilde{\delta}, t) &= \langle P_{AM} \times P_{DSOF} \rangle \\ &= \left\langle \left[\sum_{n=-\infty}^{\infty} \left(C_n(\theta_1, \theta_2, \Omega') e^{i[2n\omega_m(t-T)]} \right) \right] \times \frac{1}{2} \left[1 + \cos\left(\frac{\tilde{\delta} L}{v} + \frac{\delta x_d}{v} - \delta t \right) \right] \right\rangle \end{aligned} \tag{6.7}$$

where the $\langle\rangle$ denotes an average over the initial energy distribution of the atomic beam (approximately Gaussian with a mean of 35.7 THz and an rms width of 2.2 THz), $T = x_d/v'$ is the transit time of an atom from the second AM coil to the

detector, and the coefficients C_n, arise from Bessel function expansions [91] of the sine and cosine terms in Eq. 6.1.

To study a stripe of the density matrix a distance $\Omega_{coh} = 2N\omega_m$ off the diagonal (or equivalently a particular $n = N$ component of $P_{AM}(t)$), we set $\delta = 2N\omega_m$, heterodyning its time-dependence down to dc. A sweep of the scaled detuning $\tilde{\delta}$ (with fixed δ) produces rephased Ramsey fringes [68], whose Fourier transform with respect to $\tilde{\delta}$ yields the desired stripe of the density matrix. In the semiclassical picture, the amplitude of this stripe is the velocity distribution of the atoms in the beam with $2N\omega_m t$ time-dependence, while the phase reveals whether atoms at a given velocity arrived in or out of phase with the "clock" set by the heterodyne signal $\cos(\delta t)$.

6.2.2 Experiment

We first probed the diagonal of the double AM density matrix by setting $\delta = 0$, making the DSOF equivalent to a standard separated oscillatory field experiment [45]. This configuration yields Ramsey fringes (Fig. 6-2) as a function of $\tilde{\delta}$, whose Fourier transform represents the energy distribution of the AM modified atomic beam, or equivalently the diagonal of the density matrix (Fig. 6-3a).

To probe off-diagonal elements of the density matrix, we used a single sideband modulator [115] to generate a phase coherent signal at $\omega_2 = \omega_1 - \delta$ from ω_1 and a local oscillator, enabling us to scan ω_1, and hence $\tilde{\delta}$, while maintaining phase coherence between the two DSOF coils. We first set $\delta = 2\omega_m$ and observed rephased Ramsey fringes, which were displaced $2\pi \times 0.6$ MHz from the center of the resonance line due to the relative phase evolved by plane wave components propagating from the double AM to the DSOF [68]. A Fourier transform of these fringes determined a stripe of the density matrix a distance $\Omega_{coh} = 2\omega_m$ away from the diagonal (as well as its Hermitian conjugate at $\Omega_{coh} = -2\omega_m$).

We repeated this process to measure other non-zero off-diagonal stripes of the density matrix, setting $\delta = 4\omega_m$ and $6\omega_m$, and measuring fringes centered $\sim 2\pi \times 1.2$, 1.8 MHz away from the center of the resonance line respectively. At these large detunings the DSOF regions produced less than the $\pi/2$ pulses assumed in Eq. 6.7,

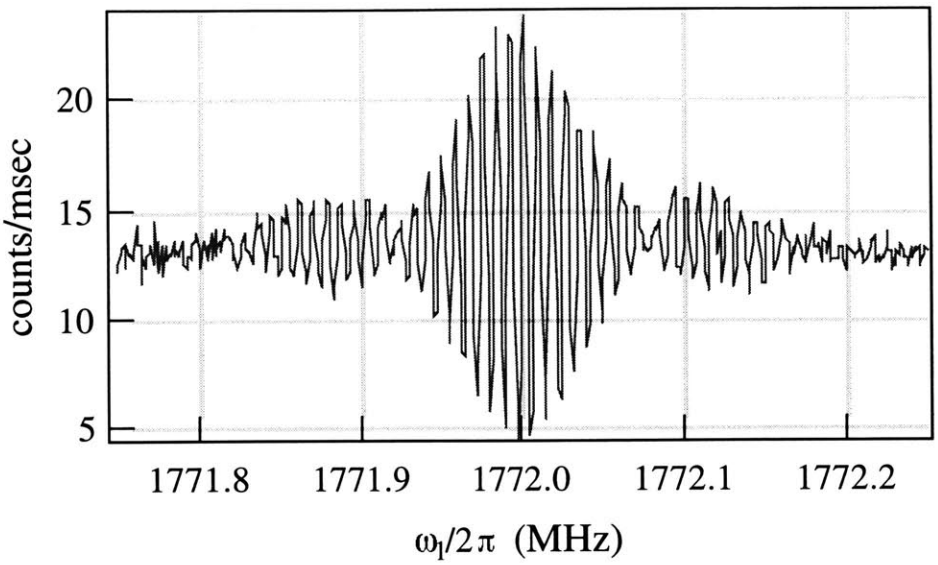

Figure 6-2: Ramsey fringes obtained by DSOF with $\delta = 0$. The envelope of the fringes reflects the modified atomic energy distribution produced by the AM regions, which had modulation frequency $\omega_m = 2\pi \times 60.9$ kHz.

limiting the signal/noise for these measurements and preventing us from measuring the weak off-diagonal stripes at higher multiples of ω_m.

The amplitude of the density matrix, calculated from an average of two data sets (about 2 hr of data with a mean count rate of 8 to 10 kcounts/sec) is shown in Fig. 6-3a. Quantum mechanically, the multiple peaks along Ω' (parallel to the diagonal) arise from the interference of plane wave components that accrue relative phase shifts (by multiples of $2\omega_m L_c/v$) while propagating from the first to the second AM region. In the semiclassical picture, these peaks reflect the velocity selection of the two AM regions, which transmit only atoms which have a transit time $\tau = L_c/v$ that are near multiples of the modulation periods $T_{mod} = 2\pi/(2n\omega_m)$.

The phase of the density matrix is displayed in Fig. 6-3b. The positive and negative phase regions correspond to velocities in and out of phase with the DSOF heterodyne signal. The overall slopes of the phases reflect their dependence on the transit time between the AM coils, $\tau = L_c/v$. The relative phases between elements within each constant Ω_{coh} stripe were measured, but the relative phase between stripes with different Ω_{coh} values could not be directly determined, because the phase of our

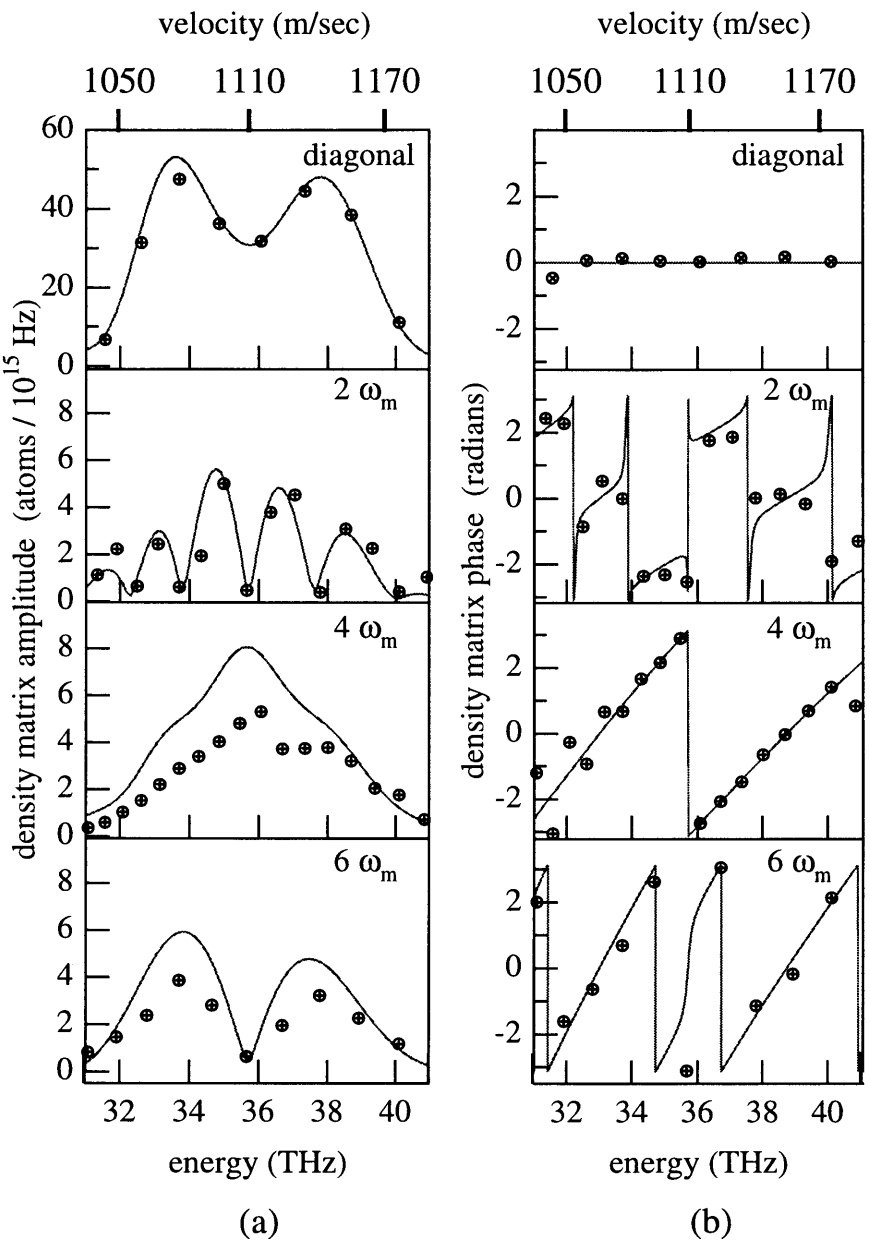

Figure 6-3: Amplitude (a) and phase (b) of the density matrix produced by the double AM system with $\omega_m = 2\pi \times 60.9$ kHz. Solid lines represent the theoretical model, and the markers the density matrix measured via Fourier transforms of rephased Ramsey fringes. The amplitudes are normalized to one for the unmodulated atomic beam. Overall phase factors have been subtracted from the phase data to compensate for the random phase between sidebands.

single sideband mixer jumped when the heterodyne frequency δ was changed.

To infer this relative phase and to compare our measurement of the density matrix with our theoretical prediction, we calculated the C_n of Eq. 6.7 corresponding to each off-diagonal stripe (i.e. for each $2n\omega_m$ term). The product of C_n and the initial energy distribution (obtained from an SOF scan of the unmodified beam) then provided a prediction for each stripe of the density matrix. The parameters $\theta_{1,2}$ were adjusted to obtain the best possible agreement between the theoretical model and the amplitude data. By comparing the measured phase of each density matrix stripe with that of our prediction, we determined the unknown phase offset of each stripe, which we subtracted to obtain the comparison of phases displayed in Fig. 6-3b.

Our theoretical prediction agrees with the experimentally measured density matrix (Fig. 6-3), as witnessed by the fact that variations in the model density matrix produced by slightly altering the initial velocity and mean count rate of our beam (within the measurement error of these quantities) generate larger changes than the discrepancy between the best fitting model and the experimental measurement.

6.2.3 Conclusion

We have employed a longitudinal DSOF interferometer [68] to measure the density matrix of a doubly amplitude modulated atomic beam in the longitudinal energy/momentum basis, showing that this density matrix possesses theoretically predicted structure both along and off the diagonal. This work is the first experimental demonstration of a such a measurement (the subject of several theoretical proposals [81, 94, 98]), and it extends previous measurements of the density matrix and Wigner function [34, 35, 36, 41] to longitudinally coherent matter waves.

Possible future experimental improvements include improving the phase control of our single sideband mixer, which would allow direct determination of the relative phase between off-diagonal stripes of the density matrix. The extension of this work to cold atom or Bose-Einstein condensate beams [116, 117], which possess low energies and narrow energy widths, would allow the study of density matrices of these highly coherent quantum systems.

We thank R. Lutwak, K. Helmerson, and W. Phillips of NIST and D. Fried, T. Killian, and D. Kleppner of MIT for the loan of frequency synthesizers. This work was supported by Army Research Office contracts DAAH04-94-G-0170, DAAH04-95-1-0533, DAAG55-97-1-0236, and DAAG55-98-1-0429, Office of Naval Research contract N000014-96-1-0432, Joint Services Electronics Program contracts DAAH04-95-1-0038 and DAAG55-98-1-0080, and National Science Foundation grant PHY-9514795. J. Lehner was supported by the Otto Hahn Award of the Max Planck Society, and H. Bernstein acknowledges the support of National Science Foundation grant PHY-9722614.

6.3 Theoretical Issues

This section provides a more detailed discussion of the "double AM" density matrix studied in the deconvolution experiment, as well as further discussion about the data acquisition, analysis, and modeling.

6.3.1 Three-State Double AM

In our deconvolution experiment, we measured a density matrix produced by two successive synchronously driven amplitude modulation regions. We now provide a theoretical treatment of this system, which we used to model our experimental results. To do so, we generalize the presentation of Sec. 2.2.4 (which discussed AM produced by applying an amplitude modulated oscillatory field to a two-state atom) to our actual experimental configuration, in which a three-level system (the $F = 1$ hyperfine manifold) was employed.

We consider an atomic wavefunction $|\Psi(x,t)\rangle = e^{i(k_o x - \Omega_o t)}\,|1,0\rangle$ that passes through successive AM regions located at $x = -L_c$ and $x = 0$ (see Fig. 4-4) which resonantly couple the $|1,0\rangle$ to both of the $|1,\pm 1\rangle$ states. Assuming as usual $\frac{\omega_m}{\Omega_o} \ll 1$, we can solve the time-dependent Schrödinger equation inside the AM regions and match boundary conditions at their edges to find the downstream wavefunction[4]

$$\begin{aligned} |\psi(x,t)\rangle \;=\; & \Big\{\cos\Big[\theta_1 \sin\left(\omega_m\left[x/v - (t - L_c/v)\right]\right)\Big]\;\cos\Big[\theta_2 \sin\left(\omega_m\left[x/v - t\right]\right)\Big] \\ & - \cos\phi_B\;\sin\Big[\theta_1 \sin\left(\omega_m\left[x/v - (t - L_c/v)\right]\right)\Big] \\ & \times \sin\Big[\theta_2 \sin\left(\omega_m\left[x/v - t\right]\right)\Big]\Big\}\, e^{i(k_o x - \Omega_o t)}\;\;|1,0\rangle\,, \end{aligned} \tag{6.8}$$

where we have assumed that the carrier frequency $\omega_c = 2\pi \times 7.65$ MHz, of the transition (identical for both AM regions) is very nearly tuned to resonance, ω_m is the modulation frequency, $\theta_{1,2} = \frac{\omega_{R1,2} l_{1,2}}{v}$, and

[4]Many thanks to Prof. Winn Smith of the University of Connecticut for his work on verifying this calculation.

$$\pm\,\phi_B(z) = \pm\left(\frac{\mu_o}{2\hbar v}\int_0^{L_c} B(x,z)\,dx - \frac{\omega_c\,L_c}{v}\right). \tag{6.9}$$

The first term in Eq. 6.9 denotes the relative phase evolved between the $|1,0\rangle$ and the $|1,\pm1\rangle$ components in traveling between the AM regions, while the second denotes the phase acquired by the oscillatory field during this interval. [5]

In Eq. 6.8, the first term in brackets is the amplitude for an atom to pass through both AM coils without changing state. The second term is the amplitude for an atom to be transferred to the $|1,\pm1\rangle$ or $|1,\pm-1\rangle$ state by the first AM region and then be transferred back into the $|1,0\rangle$ state by the second AM. Amplitudes following the latter path experience an energy/momentum shift in the region between the coils, and receive a phase shift ϕ_B relative to the non-excited amplitudes.

The probability of detecting an atom in the $|1,0\rangle$ state at any point downstream of the second AM region is the absolute value squared of Eq. 6.8

$$\begin{aligned}
P_{AM}(x,t) \;=\; & \cos^2\!\left[\theta_1 \sin\left(\omega_m\left[\frac{x}{v}-(t-\tau)\right]\right)\right]\cos^2\!\left[\theta_2\sin\left(\omega_m\left[\frac{x}{v}-t\right]\right)\right] \\
& + \cos^2\phi_B \sin^2\!\left[\theta_1 \sin\left(\omega_m\left[\frac{x}{v}-(t-\tau)\right]\right)\right]\sin^2\!\left[\theta_2\sin\left(\omega_m\left[\frac{x}{v}-t\right]\right)\right] \\
& + \cos\phi_B \cos\!\left[\theta_1 \sin\left(\omega_m\left[\frac{x}{v}-(t-\tau)\right]\right)\right]\cos\!\left[\theta_2\sin\left(\omega_m\left[\frac{x}{v}-t\right]\right)\right] \\
& \times \sin\!\left[\theta_1 \sin\left(\omega_m\left[\frac{x}{v}-(t-\tau)\right]\right)\right]\sin\!\left[\theta_2\sin\left(\omega_m\left[\frac{x}{v}-t\right]\right)\right]
\end{aligned} \tag{6.10}$$

Equation 6.10 demonstrates that the successive application of two three-state resonance regions can produce three-state Ramsey fringes [118]. Like the interference pattern from three slits, these fringes are narrowed relative to the usual two-state fringes when measured as a function of ϕ_B.

Such fringes, however, were not visible in our apparatus because of the presence of uncontrolled magnetic field gradients. To demonstrate the fragility of these fringes, we define $\overline{B}$, the average value of the magnetic field experienced by an atom following

[5] Equations 6.8, 6.9 are equivalent to Eqs. 6.1, 6.2 in reference Sec. 6.2, and are included again here for clarity.

a particular trajectory between the AM coils. The criterion for the observability of three-state fringes is then $\Delta\phi_B = \frac{\mu_o}{2\hbar}\frac{\overline{B}}{v}\frac{\Delta\overline{B}}{\overline{B}} < \pi$, which yields the result that $\frac{\Delta\overline{B}}{\overline{B}}$ must be less than about 5 parts in 10^{-4} over the 1 mm height of the atomic beam. Our lack of magnetic field uniformity means that when we perform an ensemble over the atom trajectories, ϕ_B varies over more than π, eliminating the third term in Eq. 6.10, destroying the internal atomic coherence, and leading to a probability

$$\begin{aligned}\langle P_{AM}(x,t)\rangle_{traj} = \cos^2\Big[\theta_1 \sin\Big(\omega_m\Big[\frac{x}{v}-(t-\tau)\Big]\Big)\Big]\cos^2\Big[\theta_2\sin\Big(\omega_m\Big[\frac{x}{v}-t\Big]\Big)\Big] \\ +\frac{1}{2}\sin^2\Big[\theta_1 \sin\Big(\omega_m\Big[\frac{x}{v}-(t-\tau)\Big]\Big)\Big]\sin^2\Big[\theta_2\sin\Big(\omega_m\Big[\frac{x}{v}-t\Big]\Big)\Big],\end{aligned} \tag{6.11}$$

where the $\langle\rangle_{traj}$ denotes the ensemble average over all possible atomic trajectories. We note that the ensemble average which eliminates the internal state coherence leaves the coherence of the *external* (i.e. longitudinal) quantum state unchanged.

We tested the applicability of Eq. 6.11 to our experiment by driving the double AM system with a low modulation frequency ω_m and observing the time-dependent atom signal at the detector, as shown in Fig. 6-4. We note that averaging away the ϕ_B terms means that the time- and space-dependent transmission probability of Eq. 6.11 can be obtained via an alternate method, by calculating the *population* (rather than amplitude) transfer caused by each AM coil, and ignoring the internal state evolution in the region between the coils.

6.3.2 Double AM Density Matrix

To calculate the density matrix produced by the double AM system, we can use Eq. 6.8 to calculate the density operator $\widehat{\rho} = \overline{|\psi(x,t)\rangle\langle\psi(x,t)|}$, where the overbar denotes an ensemble average over all the trajectories and all initial energies (or velocities) present in the atomic beam. Equivalently, we can take Eq. 6.11, integrate it over the initial energy distribution $f(\Omega')$ and extract the coefficients of the time and space-dependent terms. The resulting density matrix is

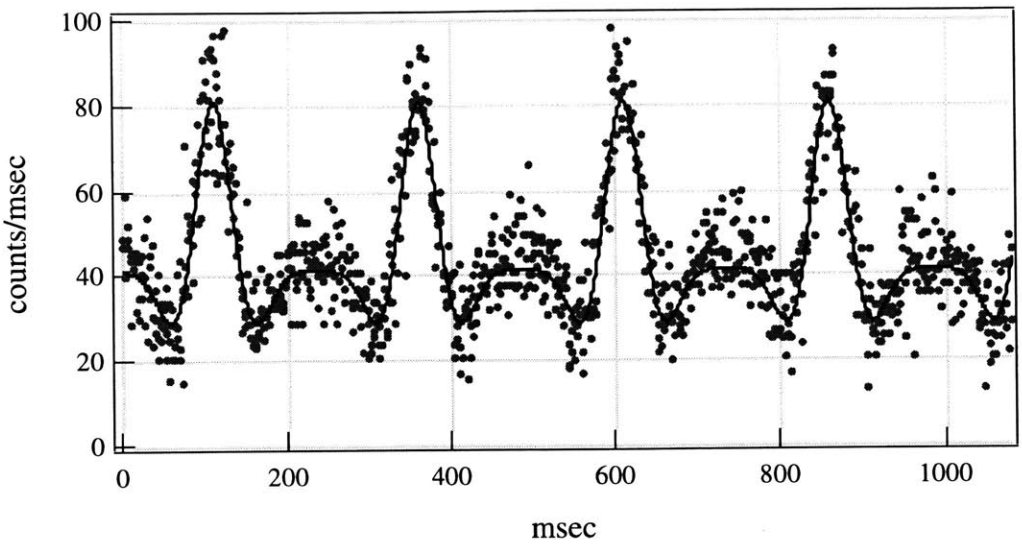

Figure 6-4: Time-dependent atom signal produced by transmission through two synchronously driven AM coils for $\omega_m = 2\pi \times 2$ Hz. The points represent the data, while the solid line represents a fit to Eq. 6.11. This fit allows us to determine the parameters $\theta_1 = 1.72 \pm .03$ and $\theta_2 = 1.43 \pm .02$.

$$\rho(\Omega', \Omega'') = f(\Omega') \sum_{n=-\infty}^{\infty} C_n(\Omega', \theta_1, \theta_2, L_c)\ \delta(\Omega_{coh} - 2n\omega_m) \tag{6.12}$$

where we have employed the Bessel function expansions[91]

$$\cos(\theta \sin\phi) = J_0(\theta) + 2\sum_{n=1}^{\infty} J_{2n} \cos[2n\phi] \tag{6.13}$$

$$\sin(\theta \sin\phi) = 2\sum_{n=1}^{\infty} J_{2n-1}(\theta) \cos[(2n-1)\phi] \tag{6.14}$$

to obtain the coefficients

$$C_{n\geq 0}(\Omega', \theta_1, \theta_2, L_c) = \frac{1}{8}\left[3\delta(n,0) + J_{2n}(2\theta_1)e^{-i2n\omega_m \frac{L_c}{v'}} + J_{2n}(2\theta_2) + 3\sum_{m=-\infty}^{\infty} J_{2|m|}(2\theta_1) J_{2|n+m|}(2\theta_2) e^{i2m\omega_m \frac{L_c}{v'}}\right], \tag{6.15}$$

and

$$C_{n<0}(\Omega', \theta_1, \theta_2, L_c) = C^*_{n>0}(\Omega', \theta_1, \theta_2, L_c). \tag{6.16}$$

The time-dependent atom signal produced by this density matrix, which likewise contains frequency components at multiples of $2\omega_m$ is

$$P_{AM(x,t)} = \int d\Omega' f(\Omega') \sum_{n=-\infty}^{\infty} C_n(\Omega', \theta_1, \theta_2, L_c) e^{i2n\omega_m(\frac{x}{v}-t)}. \tag{6.17}$$

To obtain a quantum mechanical interpretation of the double AM density matrix we consider an expansion (using Eqs. 6.13, 6.14) of Eq. 6.8, which reveals that an incident plane wave is split at the first AM region into an infinite ladder of energy/momentum sidebands (see Eq. 4.2), spaced at $2\hbar\omega_m$ in energy and $\frac{2\hbar\omega_m}{v}$ in momentum. These sidebands all propagate a distance L_c downstream to the second AM region, where each is separated into a second infinite ladder of sidebands. The wavefunction downstream of the second AM thus contains energy components differing by $2n\hbar\omega_m$ for integer n, a result which leads to the off-diagonal structure of the double AM density matrix seen in Eq. 6.12.

While traversing the region between the AM coils the plane wave components produced by the first AM acquire relative phase shifts which are multiples of $2\omega_m \frac{L_c}{v}$. For certain velocities v, some of these components cancel each other out, and hence atoms with those particular time-dependences and velocities are not transmitted—a fact which leads to the creation of structure along Ω', parallel to the diagonal of the density matrix. A simplified depiction of this process, portraying just two sets of interfering paths, is shown in Fig. 6-5. The plane wave picture of the density matrix also sheds light on the behavior of the rephased fringes produced by passing the double AM density matrix through the DSOF interferometer: the various relative phases cause the presence of additional rephasing peaks spaced at $\tilde{\delta} = 2n\omega_m \frac{L_c}{L}$.

In addition to the quantum description of the density matrix, our semiclassical approximation ($\frac{\omega_m}{\Omega'} \ll 1$) provides an alternative interpretation. In this picture, the two AM regions act like velocity selectors ("choppers") [119], whose total transmission probability is the product of the transmission probabilities of the first and sec-

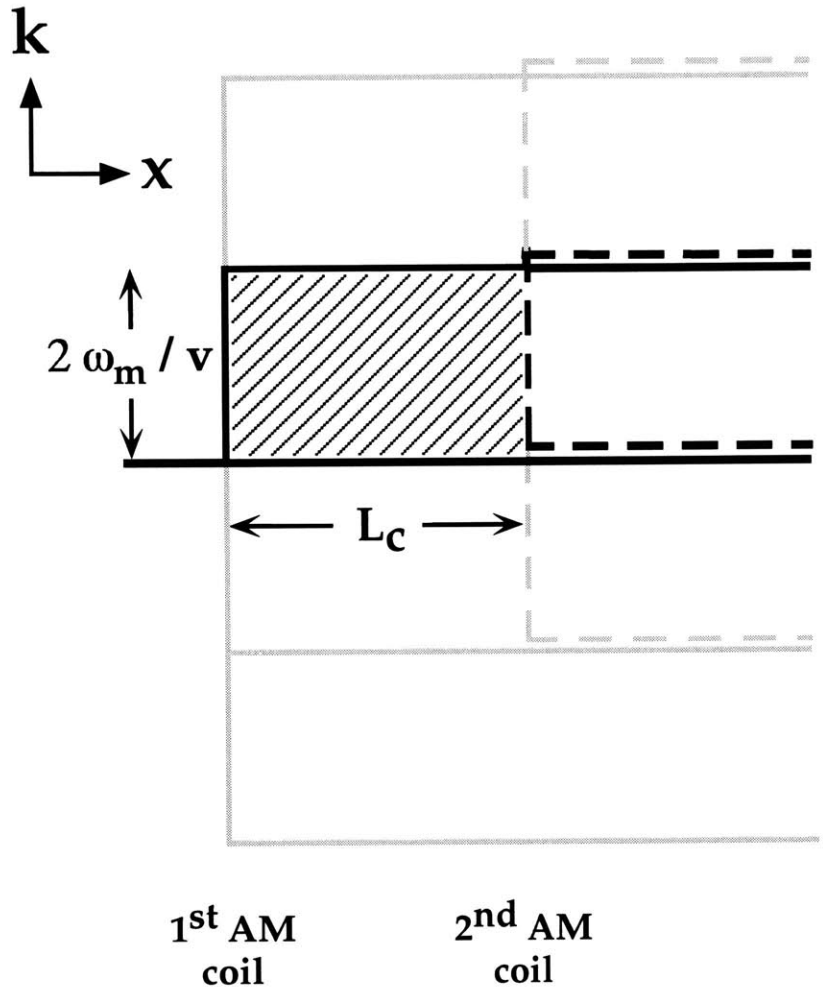

Figure 6-5: Graphical representation of two of the sets of interfering plane wave components contributing to the density matrix stripe with $\Omega_{coh} = 2\omega_m$. The dark solid and dark dashed lines both represent pairs of paths separated by $2\omega_m$ in frequency and $2\frac{\omega_m}{v}$ in wavevector, which contribute to the $\Omega_{coh} = 2\omega_m$ off-diagonal stripe of the density matrix. However the solid paths (produced at the first AM coil) travel an extra distance L_c, and hence accumulate an extra relative phase $2\omega_m \frac{L_c}{v}$ (hatched area) compared to the paths produced at the second AM coil (dashed lines). The light lines represent some of the other paths in the infinite ladder of sidebands produced by the two AM regions.

ond choppers, each of which contains oscillating components with frequencies $2N\omega_m$ ($2M\omega_m$). This product contains sum and difference frequencies $2(N \pm M)\omega_m = 2n\omega_m$, providing the classical equivalent of the off-diagonal structure of the density matrix (where $\Omega_{coh} = 2n\omega_m$) produced by consideration of coherent sums of amplitudes.[6] In addition, the first chopper transmits pulses of atoms containing all possible velocities, while the second chopper transmits only atoms whose transit time between the AM coils is $\tau = \frac{L_c}{v} = NT_{chop}$, (where $T_{chop} = \frac{2\pi}{2n\omega_m}$ is the chopper period), creating maxima and minima in the amplitude of the density matrix parallel to the diagonal.

6.4 Deconvolution Data Acquisition

To acquire data for the deconvolution of the double AM density matrix, we first aligned the atomic beam, as discussed in Ch. 4. We employed our double AM driver circuit (Fig. 4-6) to adjust the strength of the signals applied to the two AM regions, and hence the parameters $\theta_{1,2}$. By collecting time-dependent data with $\omega_m = 2\pi \times 2$ Hz and fitting the resulting signal to Eq. 6.11, we were able to roughly determine these values (Sec. 6.3.1). We adjusted $\theta_{1,2}$ until they were nearly equal, since this lead to the clearest density matrix structure.

We took SOF scans (see Sec. 4.3.1) of the atomic beam with the AM regions turned off to obtain the original velocity distribution of the atomic beam, which we found to be nearly Gaussian with a mean velocity of $v_o = 1110$ m/sec and an rms width of $\sigma_v = 36$ m/sec. Turning on the AM regions, we then acquired a series of SOF scans (see Fig. 6-7), whose Fourier transform yielded real-time pictures of the diagonal of the double AM density matrix.

The modulation frequency ω_m was adjusted to obtain maximally visible structure in the amplitude of the density matrix. We found that low frequencies ($\omega_m < 2\pi \times 40$ kHz) did not significantly alter the shape of the diagonal. High frequencies ($\omega_m > 2\pi \times 80$ kHz) produced a great deal of structure, but lead to poor visibility of the

[6] As discussed in Sec. 3.3, the phase of the time-dependent atom signal relative to a clock oscillating at $2n\omega_m$ is equivalent to phase of the corresponding density matrix element.

off-diagonal stripes, because for these values of ω_m the rephasing peaks produced by the DSOF fell outside the DSOF single coil linewidths. We picked $\omega_m = 2\pi \times 60.9$, which positioned a "cut" produced by the double AM modulation in the center of the original Gaussian velocity distribution, and lead to substantial structure along both the diagonal and the off-diagonal stripes (Fig. 6-3). We found that changing the modulation frequency by only $2\pi \times 100$ Hz or the mean velocity by only 0.5% clearly modified the shape of the density matrix.

Drifts in the mean velocity of our atomic beam limited our ability to average together deconvolution data acquired over long times. We observed drifts in v_o on the order of 0.5-1% over tens of minutes, which we attributed to thermal shifts in the alignment of the atomic beam, causing relative displacement of the beam center and the detector wire. Since the state selecting Stern-Gerlach magnets spread out different atomic velocities over a transverse distance greater than the width of our detector wire, the transverse position of the detector effects the velocity distribution of the atoms it measures.

We measured the size of this effect by translating the detector wire across the atomic beam profile, collecting SOF scans at each point. The mean velocity and velocity width obtained from these are shown in Fig. 6-6, which revealed that the mean velocity of the beam shifted by 1.5 m/sec per micron of detector wire displacement. Thus, only 3 microns of drift in the relative transverse positions of the detector wire and the atomic collimation slits (2.5 m away) could account for the observed shifts in the mean velocity.

We observed that drifts in v_o seemed to be somewhat more severe immediately after the liquid nitrogen reservoirs used to cryopump the detector and main chambers were refilled. Therefore, to minimize drifts, we filled the reservoirs to their maximum levels, waited several minutes for the apparatus to reach thermal equilibrium, and took all necessary data for the density matrix produced by a particular ω_m value in one continuous chunk (refilling the main chamber reservoir during this interval only as absolutely necessary). This process limited the amount of data we could acquire, but minimized the drift in the mean velocity.

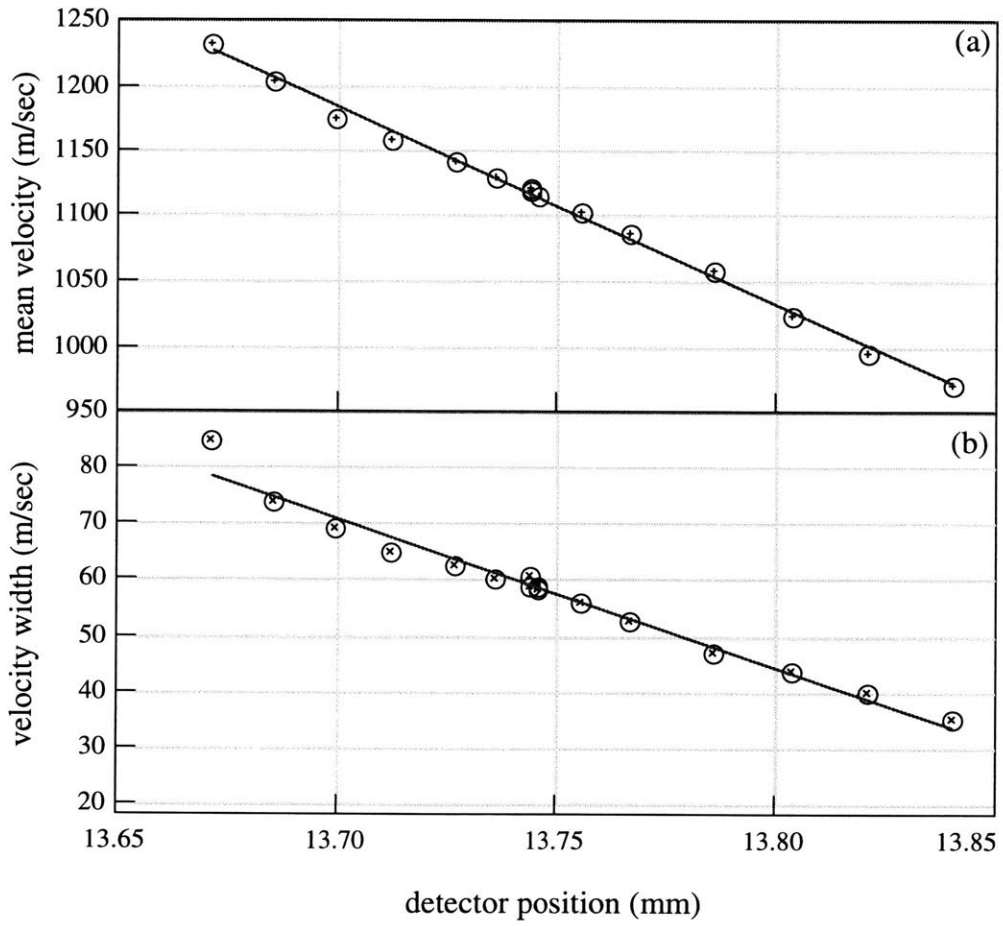

Figure 6-6: Mean velocity (a) and velocity width (b) as a function of detector position. The markers are data (from Fourier transforms of SOF fringes) and the solid lines are fits, which yield slopes of $-1.5 \pm 0.03 \frac{\text{m/sec}}{\text{micron}}$ for mean velocity and $-0.27 \pm 0.01 \frac{\text{m/sec}}{\text{micron}}$ for the velocity width.

To collect data for a particular value of ω_m, we first took several SOF scans with the AM regions on and off, allowing us to ascertain the mean counts in the unmodulated beam as well as the diagonal of the density matrix. We then employed the DSOF interferometer, with its coils driven by the single sideband (SSB) modulator described in Sec. 4.2.2, to determine the off-diagonal stripes of the density matrix.

By setting $\delta = 2n\omega_m$, we heterodyned each off-diagonal stripe of the density matrix down to dc. We then swept ω_1 (which in turn sweeps $\tilde{\delta}$, as shown in Eq. 3.7). The DSOF, as discussed in Sec. 2.2.5, applied a velocity dependent phase shift that reversed the velocity dephasing of the AM modulation imposed on the beam by the double AM system, leading to rephased Ramsey fringes as $\tilde{\delta}$ was scanned (Fig. 6-7). The presence of interfering plane wave components with phase shifts at multiples of $2n\omega_m \frac{L_c}{v}$ caused the multiple sets of rephased fringes, whose centers were spaced at intervals of $2\omega_m \frac{L_c}{L}$.

A numerical model of the signal produced by the AM and DSOF (see Sec. 6.5) was employed to predict the location of these fringes, allowing us to bracket the range of ω_1 where the signal was expected. For small detunings (i.e. $\delta = 2\omega_m, 4\omega_m$) we employed $\frac{\pi}{2}$ pulses on the SSB, while for large detunings higher power (π on resonance) pulses were used, a technique which resulted in maximal signal/noise, as discussed in Sec. 4.3.1.

While the SSB modulator allowed us to apply two different frequencies $\omega_{1,2}$ to the two DSOF coils while maintaining a stable "clock" or reference oscillator at frequency δ, the phase of this clock was reset whenever δ was changed. This loss of the phase reference of our local oscillator signal prevented us from directly observing the relative phase between stripes of the density matrix at different Ω_{coh}. We emphasize that our measurement of the amplitude of the density matrix is not affected by this phase reset, and that there is only *one* overall phase for each stripe that could not be determined. As we discuss in Sec. 6.5, by matching the measured density matrix phase to our theoretical model, we were able to infer these unknown phases.

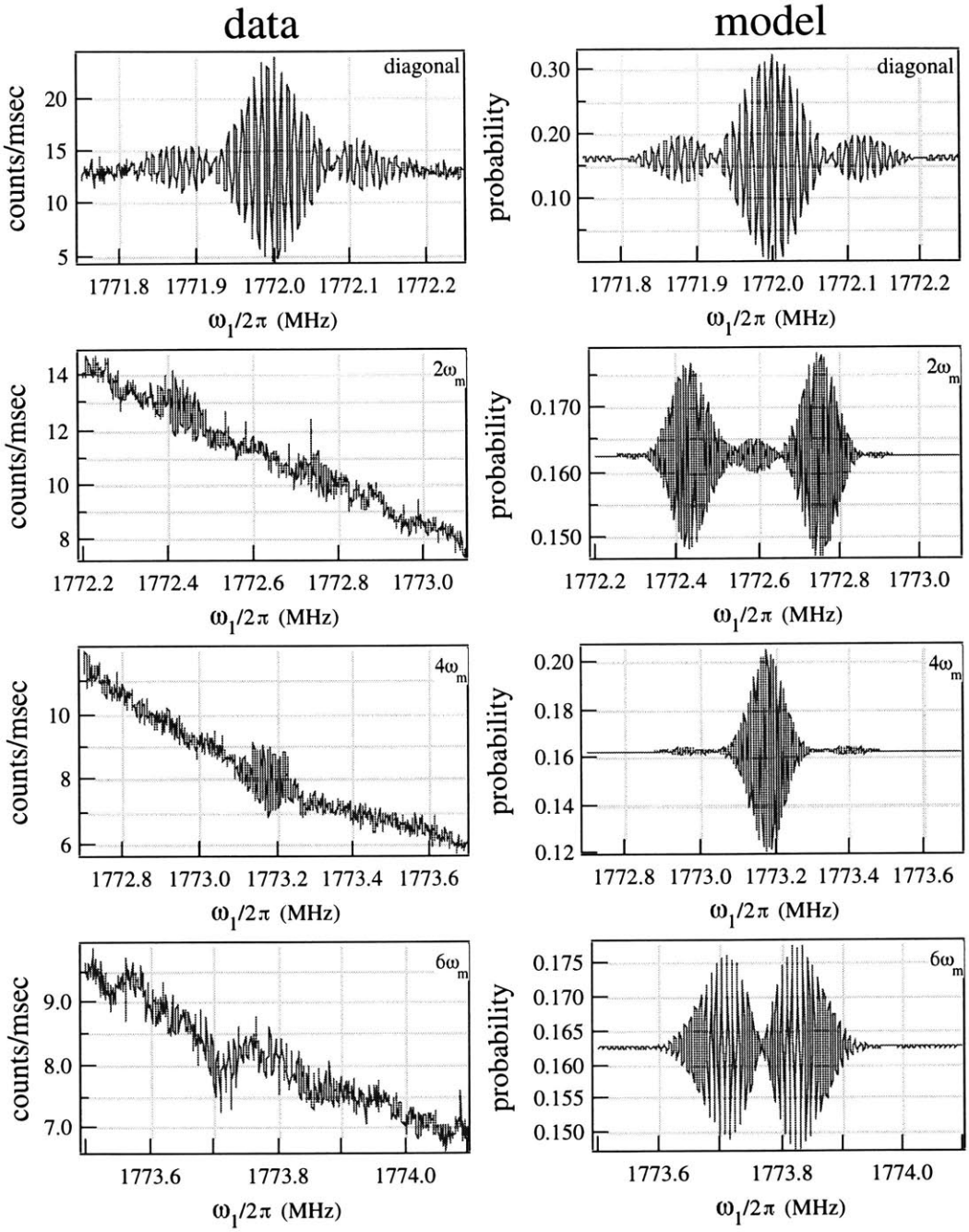

Figure 6-7: Data (left) and model (right) rephased Ramsey fringes produced by the DSOF in our study of the double AM density matrix. The linear slope data for the off-diagonal rephased fringes arises from the reduced ability of the DSOF coils to maintain $\frac{\pi}{2}$ pulse conditions on the edge of the Rabi pedestal (see Sec. 4.3.2). The model fringes were produced by a technique discussed in Sec. 6.5.

6.5 Analysis and Modeling

To determine the density matrix of the double AM system, we re-expressed the rephased Ramsey fringes shown in Fig. 6-7 (acquired as a function of ω_1) as a function of

$$\tilde{\delta} = (\omega_1 - \omega_{hf}) - \delta\frac{x_2}{L}, \tag{6.18}$$

where $\omega_{hf} = 2\pi \times 1772$ MHz is the center of the resonance line, x_2 is distance from the second AM coil to the first DSOF coil, and $L = .1294$ m is the separation of the two DSOF coils. This change of variables is necessary because (as shown in Eq. 3.15) we obtain the density matrix stripes from the Fourier transform, with respect to $\tilde{\delta}$, of the rephased Ramsey fringes.

To normalize the experimentally measured density matrix we consider the effect of the finite linewidths of the DSOF coils, which lead to a decrease in the mean count rate as ω_1 was increased. Rewriting Eq. 3.15, the predicted expression for the rephased Ramsey fringe signal we find

$$S(2n\omega_m, \tilde{\delta}) = \overline{N}_{2n} + \overline{N}_{2n} C \int_{-\infty}^{\infty} d\Omega' \, |\rho(\Omega', \Omega' - 2n\omega_m)| \times \cos\left(\frac{\delta L}{v'} - \phi(\Omega', \Omega' - 2n\omega_m)\right), \tag{6.19}$$

where $S(\tilde{\delta}, 2n\omega_m)$ is the atom signal (see Fig. 6-7), C is the contrast of the DSOF interferometer (which we assume to be constant) and $\overline{N}_{2n}$ is the mean count rate for a set of data corresponding to a particular stripe of the density matrix. Because of the decreasing ability of the DSOF coils to excite atoms at frequencies far from resonance (Fig. 4-9), $\overline{N}_{2n}$ decreases for higher sidebands. The Fourier transform of Eq. 6.19 yields the non-normalized density matrix.

The properly normalized density matrix, which has $\mathrm{tr}(\hat{\rho}) = 1$ for an unmodulated beam, is given for each stripe of the density matrix by

$$|\rho(\Omega', \Omega' + 2n\omega_m)| = \frac{1}{N_{raw}} \frac{\overline{N}_0}{\overline{N}_{2n}} \tilde{S}(2n\omega_m, \Omega'), \tag{6.20}$$

where $\tilde{S}(2n\omega_m, \Omega')$ is the raw Fourier transform of the atom signal and N_{raw} is the mean counts/sample in the unmodulated beam.

To test the accuracy of our measurement of the density matrix we first modeled the atomic signal observed in our experiment, by calculating the rephased Ramsey fringe pattern expected for each setting of δ (i.e. the data used to obtain each stripe of the density matrix). This model numerically evaluated the atomic detection probability for passage of the beam through the double AM and DSOF, calculated by explicitly performing the integral over the initial velocity distribution $f(v)$ in Eq. 6.7

$$\begin{aligned} S_{TOT}(\delta, \tilde{\delta}) &= \left\langle \int dv f(v) P_{AM}(v,x,t) \times P_{DSOF}(v,x,t) \right\rangle \\ &= \left\langle \int dv f(v) \left[\cos^2\phi_1 \cos^2\phi_2 + \frac{1}{2}\sin^2\phi_1 \sin^2\phi_2 \right] \right. \\ &\quad \left. \times \frac{1}{2}\left[1 + \cos\left(\frac{\tilde{\delta}L}{v} + \frac{\delta x_d}{v} - \delta t \right) \right] \right\rangle_{time}, \end{aligned} \tag{6.21}$$

where $\phi_1 = \theta_1 \sin\left(\omega_m \left[\frac{x_d}{v} - (t - \frac{L_c}{v})\right]\right)$ and $\phi_2 = \theta_2 \sin\left(\omega_m \left[\frac{x_d}{v} - t\right]\right)$, and $\langle\rangle_{time}$ denotes an average over times longer than $\frac{2\pi}{\omega_m}$. Fourier transforms of the rephased fringes obtained from these calculated signals provided a prediction for the amplitude and phase of the density matrix. A second model of the density matrix (shown in Fig. 6-3) was obtained directly from the theoretical prediction of Eq. 6.12.

These models, which were in complete agreement with each other, required several input parameters to match the experimentally measured density matrix. The velocity distribution $f(v)$ (or equivalently the energy distribution $f(\Omega')$) of the unmodulated atomic beam was obtained from a Fourier transform of SOF fringes with the double AM modulator turned off. We employed the values $v_o = 1110.0$ m/sec and $\sigma_v = 35.6$ m/sec for all of our modeling. Despite the possibility of velocity drift (Sec. 6.4) we found that these values did not need to be changed to obtain good agreement between the models and the data.

Our models also required the distance L_c, the separation of the two AM coils, and x_2, the distance from the second AM coil to the second DSOF coil. We measured

these distances with a precision meter stick, obtaining $L_c = 11.28 \pm 0.15$ cm, and $x_2 = 57.54 \pm 0.15$ cm.[7] The values that gave the best fit between the models and the data $L_c = 11.39$ cm and $x_2 = 57.70$ cm were both within our measured uncertainty.

The final parameters employed in modeling our data, the strength of the applied AM oscillatory fields ($\theta_{1,2}$) were measured to be $\theta_1 = 1.72 \pm 0.03$, $\theta_2 = 1.43 \pm 0.2$ (see Sec. 6.4) about eight hours before the final density matrix data was acquired. The best fit values for our data, $\theta_1 = 1.65$, $\theta_2 = 1.60$ fell outside the errors for this previous determination. However, in the interim we had adjusted the overall attenuation to the coils (leaving the relative attenuation unchanged), and measured $\theta_1 \simeq \theta_2 = 2.10$, showing that it is reasonable that the power to the AM coils was much closer together than we had first measured. We therefore attribute the discrepancy between the measured and best fit values of $\theta_{1,2}$ to poor reliability of AM driver circuit, which typically exhibited substantial hysteresis when the attenuator settings were changed. A comparison of the model and the data for *both* the originally measured and best fit values of $\theta_{1,2}$, shown in Fig. 6-8 for the case of $2\omega_m$, demonstrates the increased agreement achieved by using $\theta_1 = 1.65$, $\theta_2 = 1.60$.

The amplitude and phase of the measured and predicted stripes of the density matrix are shown in Fig. 6-3. To account for the random phase imparted to the data by the fact that we had to "reset" the heterodyne signal clock when the frequency δ was changed, overall phases were subtracted from each data determined phase plot to achieve optimal agreement with the predicted density matrix phase.

[7]Here and elsewhere in our calculations, we employ $L = 12.94$ cm, obtained in [71], as the distance between the DSOF coils.

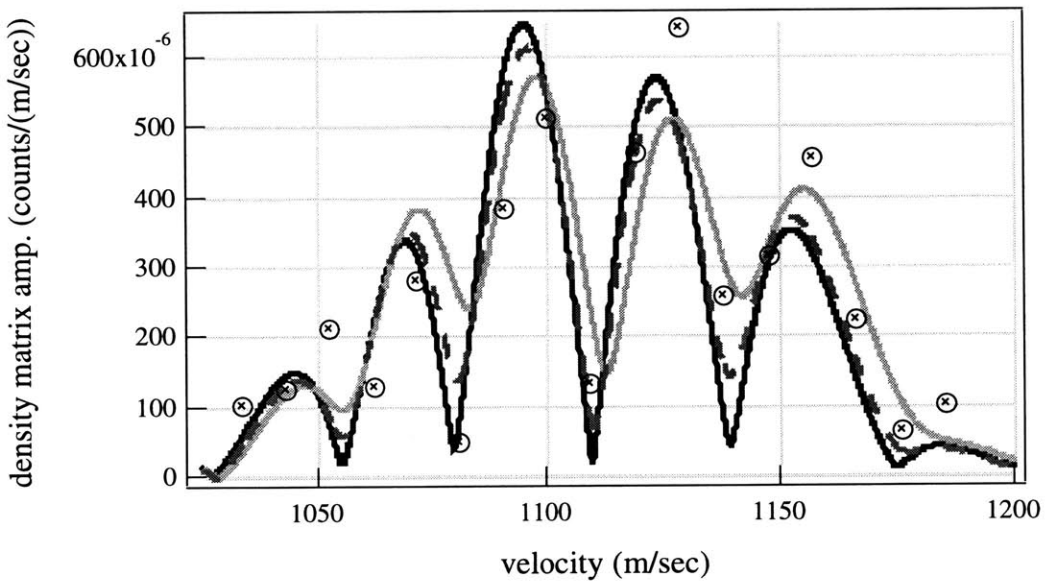

Figure 6-8: Modeled amplitude of the density matrix for $\Omega_{coh} = 2\omega_m$, demonstrating the variation in shape as a function of $\theta_{1,2}$. The thin solid line is for $\theta_1 = 1.65$, $\theta_2 = 1.60$, the values that best fit the data (see Fig. 6-3). The thick dashed line is for $\theta_1 = 1.69$, $\theta_2 = 1.52$, and the thick solid line corresponds to $\theta_1 = 1.72$, $\theta_2 = 1.43$, the values obtained from the fit in Fig. 6-4.

Appendix A

Paper: Determining the Density Matrix of a Molecular Beam Using a Longitudinal Matter Wave Interferometer

JOURNAL OF MODERN OPTICS, 1997, VOL. 44, NO. 11/12, 2583–2589

Determining the density matrix of a molecular beam using a longitudinal matter wave interferometer

AL-AMIN DHIRANI, DAVID A. KOKOROWSKI, RICHARD A. RUBENSTEIN, TROY D. HAMMOND, BERND ROHWEDDER†, EDWARD T. SMITH, ANTHONY D. ROBERTS and DAVID E. PRITCHARD

Department of Physics, Massachusetts Institute of Technology, 77 Massachusetts Avenue, Cambridge, Massachusetts 02139, USA

(*Received 14 March 1997; revision received 23 June 1997*)

Abstract. Two separated oscillatory fields, if tuned to different frequencies, can generate or interrogate longitudinal momentum coherences in a beam of two-state particles. We demonstrate that use of differentially detuned separated oscillatory fields is an efficient method to determine the longitudinal density matrix of a particle beam.

1. Introduction

Although theories describing atomic beam experiments have historically dealt with the centre-of-mass motion of particles classically, a fully quantum treatment of this motion is the essential formalism for the new fields of atom optics and atom interferometry [1]. Consequently, significant interest has arisen in fully characterizing a particle beam's quantum-mechanical and statistical properties, in turn leading to various schemes for determining the density matrix (or equivalently the Wigner function) of an atomic beam.

Position and momentum coherences along an axis perpendicular to the direction of beam propagation are well known, with myriad examples ranging from Young's two-slit experiment to Mach–Zehnder de Broglie wave interferometers. Techniques based on tomographic reconstruction of the Wigner function [2–4] and complex wave fields [5] have recently been proposed for mapping the transverse coherences in an arbitrary atomic beam, and at least one experiment [3] has been successfully carried out. Several theoretical papers [6–10] have also discussed the possibility of coherently manipulating [11, 12] the longitudinal momentum of particles in an atomic beam, including the creation of quantum superpositions of different momentum components [8, 13, 14]. However, the promising tomographic techniques useful for studying transverse coherences are difficult to apply in the longitudinal case; superpositions of states with different kinetic energies are intrinsically time dependent, leaving few methods for generally characterizing longitudinal coherences in these systems [13, 15].

† Present address: Facultad de Física Pontificia Universidad Católica de Chile, Casilla 306, Santiago 22, Chile.

0950–0340/97 $12·00

To fill the gap, we propose a novel method for measuring the density matrix representing the longitudinal centre-of-mass motion of an atomic beam. The method is based on a generalization of Ramsey's [16] classic separated oscillatory fields (SOF) technique and the observation that an atom's longitudinal momentum can be coherently shifted via interaction with off-resonance radiation. In the standard SOF experiment, a Fourier transform of the measured interference pattern gives the velocity distribution of an atomic beam (the diagonal elements $\langle\Omega|\hat{\rho}|\Omega\rangle$ of the longitudinal density matrix where $\hbar\Omega$ is the total energy). By applying different frequencies to the two oscillatory fields, we show that a similar Fourier transform approach yields the off-diagonal elements $\langle\Omega'|\hat{\rho}|\Omega''\rangle$, enabling a complete deconvolution of the longitudinal density matrix.

2. Differentially detuned separated oscillatory fields

The geometry of a particle traversing two differentially detuned separated oscillatory fields (DSOFs) is shown in figure 1. Continuous, monochromatic radiation of frequencies ω_1 and ω_2 is applied in regions 1 and 2 respectively. A fully quantum-mechanical treatment of the one- or two-oscillating-field problem [10] requires solving Schrödinger's equation, with quantized longitudinal centre-of-mass motion of the matter waves. An essential feature of this treatment is its ability to describe particles which exist in a coherent superposition of different longitudinal momentum eigenstates, each of the form

$$|\psi_\alpha(\Omega_\alpha, x, t)\rangle = \exp\left[i(k_\alpha x - \Omega_\alpha t)\right]|\alpha\rangle, \tag{1}$$

where $\alpha = e(g)$ labels the internal excited (ground) state of the particle with corresponding *total* energy $\hbar\Omega_\alpha$ and *potential* energy U_α (internal energy plus

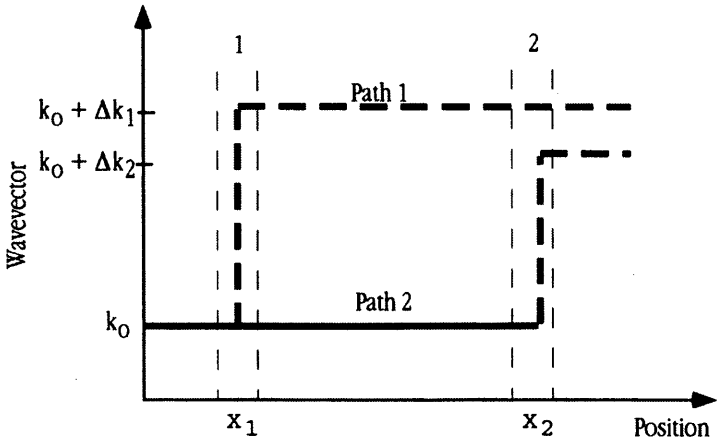

Schematic diagram of the DSOF interferometer. A plane wave with momentum $\hbar k_0$ in the ground state (——) is split into ground-state and excited-state (– – –) components by the oscillatory field at x_1. The excited-state component receives a momentum shift $\hbar\Delta k_1$. The remaining ground-state component is split again at x_2, where the excited-state component is this time momentum shifted by $\hbar\Delta k_2$. The ground-state output port is not shown.

interaction with any external fields). Since these states satisfy the free-particle Schrödinger equation, the k_α are given by

$$k_\alpha = \frac{[2m(\hbar\Omega_\alpha - U_\alpha)]^{1/2}}{\hbar}, \tag{2}$$

where m is the particle mass. For simplicity, we have ignored $k_\alpha^{-1/2}$ pre-factors which assure constant flux when U varies with x, an omission which has negligible effect if this variation is much less than the kinetic energy.

The inclusion of a quantum-mechanical description of the centre-of-mass motion provides important insights into the interactions of a particle beam with time-dependent potentials, such as rf resonance regions, and gyrating fields [16, 17]. For example, energy conservation (or equivalently arguments based on temporal Fourier decomposition of the potential) demands that $\Omega_e - \Omega_g = \omega$, where ω is a frequency component present in the time-dependent potential. As a result, whenever the energy difference between the internal states is not equal to the energy of the applied radiation (i.e. $U_e - U_g \neq \hbar\omega$), the kinetic energy must change. The corresponding change in the longitudinal wave-vector ($\Delta k \equiv k_e - k_g$) is given by

$$\Delta k = \frac{(2m)^{1/2}}{\hbar}[(\hbar\Omega_g + \hbar\omega - U_e)^{1/2} - (\hbar\Omega_g - U_g)^{1/2}]. \tag{3}$$

If the kinetic energy is much larger than $\hbar\delta$, where $\delta \equiv \omega - (U_e - U_g)/\hbar$ is the detuning of the applied radiation from resonance, then

$$\Delta k \approx \frac{\delta}{v}, \tag{4}$$

$v(\approx v_e \approx v_g)$ being the longitudinal velocity of the beam. Note that this change in wave-vector is *not* equal to the wave-vector ω/c of the corresponding photon. Rather, it arises from the spatial variation in the potential and is limited only by the inverse of the oscillatory field coil length along the beam [10]. Inclusion of this differential momentum is important, for example for extremely slow atoms for which a classical treatment of the longitudinal motion fails qualitatively [7, 18].

The view that a single detuned oscillatory region can place a particle into a superposition of ground and excited states, each with a different longitudinal momentum, suggests that both the original SOF experiment and the extension to the DSOF technique can be interpreted as longitudinal interferometers. In each case, an incident particle in the state $|\Psi(x,t)\rangle = \exp[\mathrm{i}(k_0 x - \Omega_0 t)]|g\rangle$ has two paths by which to reach state $|e\rangle$ at the interferometer output, namely excitation in either the first or the second oscillatory field region (figure). For a DSOF experiment in which both field regions have detunings which are small compared with the Rabi frequency and produce $\pi/2$ pulses (50–50 superposition of ground and excited states), the amplitude for detecting the particle in the excited state is given, up to an overall phase, by

$$\begin{aligned}\langle e|\Psi(x,t)\rangle \propto \tfrac{1}{2}\exp[\mathrm{i}(k_0 x - \Omega_0 t)]\,(&\exp\{\mathrm{i}[\Delta k_1\,(x - x_1) - \omega_1 t]\} \\ &+ \exp\{\mathrm{i}[\Delta k_2\,(x - x_2) - \omega_2 t]\}).\end{aligned} \tag{5}$$

The probability of detecting a particle in this state at location x is then determined by squaring the amplitude:

$$P_e(\omega_1,\omega_2,t) = \cos^2\{\tfrac{1}{2}[(\Delta k_1 - \Delta k_2)(x - x_2) + \Delta k_1 (x_2 - x_1) - (\omega_1 - \omega_2)t]\}. \quad (6)$$

In the SOF method, $\omega_1 = \omega_2$ and the momentum shifts $\hbar\Delta k_i$ are the same for both oscillatory fields. The additional phase accrued by path 1 relative to path 2 in the region between the oscillatory fields is $\phi = \Delta k\,(x_2 - x_1)$ and results in time-independent interference ('Ramsey fringes') as a function of detuning.

A modified interference occurs in the DSOF case, where the two paths produce excited states that are energy shifted relative to each other. The excited state now contains a coherent superposition of two distinct energy components, each with a different corresponding longitudinal momentum. The coherence is observed as a time-dependent oscillation of P_e at frequency $\omega_1 - \omega_2\,(= \delta_1 - \delta_2)$. In addition, the spatial contribution to the interference includes terms representing phases accumulated both between the two field regions, $\Delta k_1\,(x_2 - x_1)$, and beyond the second region, $(\Delta k_1 - \Delta k_2)(x - x_2)$.

3. Studying momentum coherences with differentially detuned separated oscillatory fields

A quantum treatment of the centre-of-mass motion demonstrates that time-dependent potentials such as DSOFs can create coherences in a particle's longitudinal momentum state. We now show that the DSOF method can also be used to detect initially existing longitudinal momentum coherences, a subject of significant discussion in the literature [13, 15, 19–21]. In particular, we show that this method can be used to measure the density matrix of the beam [22], and thereby to determine the most general possible statistical description of the beam's quantum state.

Suppose that a beam of particles, in a pure superposition of momentum states and in the ground internal state, is incident onto a DSOF interferometer. Its wavefunction if given initially by

$$|\Psi(x,t)\rangle = \int \mathrm{d}\Omega_0\, A(\Omega_0) \exp[\mathrm{i}(k_0 x - \Omega_0 t)]\,|g\rangle. \quad (7)$$

The linearity of Schrödinger's equation allows us to use our previous results to obtain the wavefunction after the DSOF region for this more general initial state; we simply multiply equation (5) by $A(\Omega_0)$ and integrate over Ω_0. The ensemble-averaged probability of finding the particle in the excited state at position x and time t is then given by

$$\begin{aligned} P_e(\omega_1,\omega_2,t) = \tfrac{1}{4}\int \mathrm{d}\Omega'\,\mathrm{d}\Omega''\,\rho_0(\Omega',\Omega'')\exp\{\mathrm{i}[(k' - k'')x - (\Omega' - \Omega'')t]\} \\ \times(\exp\{\mathrm{i}[\Delta k_1'\,(x - x_1) - \omega_1 t]\} + \exp\{\mathrm{i}[\Delta k_2'\,(x - x_2) - \omega_2 t]\}) \\ \times(\exp\{-\mathrm{i}[\Delta k_1''\,(x - x_1) - \omega_1 t]\} + \exp\{-\mathrm{i}[\Delta k_2''\,(x - x_2) - \omega_2 t]\}), \quad (8) \end{aligned}$$

where $\rho_0(\Omega',\Omega'') \equiv \{A(\Omega')A^*(\Omega'')\}_{\text{ens.avg.}}$ is the ensemble-averaged longitudinal density matrix in the energy representation at $x = 0$ and $t = 0$. In the limit that the density matrix elements are appreciable only for $\Omega' - \Omega'' \ll \Omega', \Omega''$, as presumably would be the case for an effusive or supersonic source, equation (8) may be

simplified by keeping only terms that are first order in δ_1, δ_2 and $\Omega' - \Omega''$:

$$P_e(\delta_1, \delta_2, t) = \int d\Omega'\, d\Omega''\, \rho_0(\Omega', \Omega'') \exp\left[- i(\Omega' - \Omega'')\left(t - \frac{x}{v'}\right)\right] \times \cos^2\{\tfrac{1}{2}[(\delta_1 - \delta_2)t - \Delta k_1'(x - x_1) + \Delta k_2'(x - x_2)]\}. \quad (9)$$

Equation (9) indicates that the probability of finding a particle in the excited state is obtained by convolving the density matrix with two factors. The cosine squared describes the influence of the oscillatory fields, and its argument reflects the phase difference accumulated between the two paths of the DSOF interferometer, as described previously. The complex exponential factor describes the free evolution of the density matrix. If the density matrix is diagonal, as would be the case for a system in an incoherent superposition of energy eigenstates, the exponential becomes unity, and the density matrix is time independent. In this limit, equation (9) reduces to Ramsey's original result when $\omega_1 = \omega_2$. On the other hand, if there are non-zero off-diagonal elements, the system exhibits coherences between different energy eigenstates, and the exponential oscillates in time at the difference frequency $\Omega' - \Omega''$.

Since the excited-state probability is given by a convolution of two *sinusoidally oscillating* factors, we can isolate elements of the density matrix by Fourier transforming twice with respect to judiciously chosen variables. First, expanding the cosine-squared factor and subtracting from P_e the term that is independent of δ_1 and δ_2, we define a new quantity $\Delta P_e(\delta_1, \delta_2, t)$:

$$\Delta P_e(\delta_1, \delta_2, t) = P_e(\delta_1, \delta_2, t) - \tfrac{1}{2}\int d\Omega'\, d\Omega''\, \rho_0(\Omega', \Omega'') \exp\left[- i(\Omega' - \Omega'')\left(t - \frac{x}{v'}\right)\right]. \quad (10)$$

Fourier transforming $\Delta P_e(\delta_1, \delta_2, t)$ with respect to time with ω_d as the conjugate variable, we find that

$$\Delta \mathcal{P}_e(\tilde{\delta}_1, \tilde{\delta}_2, \omega_d) = \frac{\pi}{2}\int d\Omega' \exp\left(i\frac{\omega_d x}{v'}\right)\left[\exp\left(\frac{i\tilde{\delta}_2(x_2 - x_1)}{v'}\right)\rho_0(\Omega', \Omega' - \omega_d + \tilde{\delta}_1) + \exp\left(\frac{-i\tilde{\delta}_2(x_2 - x_1)}{v'}\right)\rho_0(\Omega', \Omega' - \omega_d - \tilde{\delta}_1)\right]. \quad (11)$$

In equation (11), we have made the following definitions: $\tilde{\delta}_1 \equiv \delta_1 - \delta_2$ is the differential detuning or the angular frequency at which the DSOF phase evolves; $\tilde{\delta}_2 \equiv (\delta_2 x_2 - \delta_1 x_1)/(x_2 - x_1)$ is the weighted differential detuning which plays a role in the phase difference $\tilde{\delta}_2(x_2 - x_1)/v$ evolved between components of the density matrix that are overlapped by the DSOF, and $v' \equiv (2\hbar\Omega'/m)^{1/2}$ is the velocity. Finally, Fourier transforming equation (11) with respect to $\tilde{\delta}_2$, we determine $\rho_0(\Omega', \Omega' - \omega_d + \tilde{\delta}_1)$:

$$\rho_0(\Omega', \Omega' - \omega_d + \tilde{\delta}_1) = \frac{x_2 - x_1}{2\pi^2}\left(\frac{m}{2\hbar}\right)^{1/2}\frac{\exp[-i\omega_d(mx^2/2\hbar\Omega')^{1/2}]}{\Omega'^{3/2}} \times \int d\tilde{\delta}_2\, \Delta\mathcal{P}_e(\tilde{\delta}_1, \tilde{\delta}_2, \omega_d) \exp\left[- i\tilde{\delta}_2\left(\frac{m(x_2 - x_1)^2}{2\hbar\Omega'}\right)^{1/2}\right]. \quad (12)$$

Thus we can reconstruct the density matrix by measuring the dependence of the excited-state probability on the differential and weighted differential detunings, with the ω_d dependence providing information that is complementary to $\tilde{\delta}_1$.

Fundamentally, the scheme described involves detecting a signal at a frequency ω_d resulting from beating the differential frequency $\pm\tilde{\delta}_1$ of the DSOF with coherent frequency components in the beam. Since the latter are represented by density matrix elements oscillating at $\Omega'' - \Omega'$, only those elements in slices a distance $-\omega_d \pm \tilde{\delta}_1$ from the diagonal can contribute. Keeping ω_d and $\tilde{\delta}_1$ fixed, the phase difference between the two interfering arms of a DSOF can be changed by varying $\tilde{\delta}_2$; therefore, Fourier transforming the excited-state probability with respect to $\tilde{\delta}_2$ determines the elements in these slices of the density matrix. Formally, this approach resembles that described by Golub and Lamoreaux [13] who proposed reflecting neutrons from a mirror vibrating at two frequencies, sweeping the difference frequency and interpreting changes in the time-independent excited-state probability as a measure of the matter wave autorcorrelation function. The approach described here, however, is more general since it takes advantage of the two independent frequencies to determine the density matrix elements themselves rather than convolutions of density matrix elements.

An important feature of our deconvolution scheme is that we take the Fourier transform of the time-dependent detector signal instead of the time-averaged dc component. This takes advantage of the finite bandwidth of our detector, effectively measuring a range of off-diagonal density matrix slices simultaneously. As a result, $\tilde{\delta}_1$ can be stepped by half the bandwidth of our detector rather than the smaller steps desired in the final deconvolution, greatly speeding up the overall measurement of the density matrix.

Experimental considerations limit the region of the density matrix that can be investigated. Most importantly, the size of the detunings is limited by the conditions necessary for $\pi/2$ pulses and by the assumption that the detuning are small compared with the Rabi frequency. For example, for a beam with an average particle velocity of $1000\,\mathrm{m\,s^{-1}}$ and an rf region with length of $300\,\mu\mathrm{m}$, the Rabi frequency is $5 \times 10^6\,\mathrm{rad\,s^{-1}}$, limiting the detunings to about $10^6\,\mathrm{rad\,s^{-1}}$. For comparison, the angular frequency corresponding to the centre-of-mass motion of a sodium atom moving at $1000\,\mathrm{m\,s^{-1}}$ is $2 \times 10^{14}\,\mathrm{rad\,s^{-1}}$, justifying our assumption that $\Omega' - \Omega'' \ll \Omega', \Omega''$.

4. Conclusion

Use of DSOFs is a simple method to generate momentum coherences and to obtain interference between different initial longitudinal momentum components. We have presented an efficient procedure based on DSOFs for measuring the longitudinal density matrix of a molecular beam.

Acknowledgments

We thank J. Schmiedmayer for helpful conversations. This work was supported by Army Research Office contract No. DAAH04-94-G-0170 and contract No. DAAH04-95-1-0533, Office of Naval Research contract No. N00014-89-J-1207 and contract No. N000014-96-1-0432, Joint Services Electronics Program contract No. DAAH04-95-1-0038, and National Science Foundation contract

No. PHY-9514795. B. Rohwedder acknowledges the support of FONDECYT grant No. 2950068.

References

[1] BESMAN, P. (editor), 1997, *Atom Interferometry* (San Diego, California: Academic Press).
[2] JANICKE, U., and WILKENS, M., 1995, *J. mod. Optics*, **42,** 2183.
[3] KURTSIEFER, C., PFAU, T., and MLYNEK, J., 1997, *Nature*, **386,** 150.
[4] KIENLE, S. H., FREYBERGER, M., SCHLEICH, W. P., and RAYMER, M. G., 1997, *Experimental Metaphysics: Quantum Mechanical Studies for Abner Shimony*, edited by R. S. Cohen, M. A. Horne and J. Stachel (Dordrecht: Kluwer) (to be published).
[5] RAYMER, M. G., BECK, M., MCALLISTER, D. F., 1994, *Phys. Rev. Lett.*, **72,** 1137.
[6] MINIATURA, C., PERALES, F., VASSILEV, G., REINHARDT, J., ROBERT, J., and BAUDON, J., 1991, *J. Phys.*, Paris, II, **1,** 425.
[7] ENGLERT, B.-G., SCHWINGER, J., BARUT, A., and SCULLY, M., 1991, *Europhys. Lett.*, **14,** 25.
[8] SUMMHAMMER, J., 1993, *Phys. Rev.* A, **47,** 556.
[9] PUMARES, L., PLAJA, L., ROSO, L., and RZĄŻEWSKI, K., 1996, *Quantum semiclass. Optics*, **8,** 673.
[10] PRITCHARD, D. E., RUBENSTEIN, R. A., DHIRANI, A., HAMMOND, T. D., KOKOROWSKI, D. A., ROHWEDDER, B., and SMITH, E. T., 1997 (to be published).
[11] STEANE, A., SZRIFTGISER, P., DESBOILLES, P., and DALIBARD, J., 1995, *Phys. Rev. Lett.*, **74,** 4972.
[12] BERNET, S., OBERTHALER, M. K., ABFALTERER, R., SCHMIEDMAYER, J., and ZEILINGER, A., 1996, *Phys. Rev. Lett.*, **77,** 5160.
[13] GOLUB, R., and LAMOREAUX, S., 1992, *Phys. Lett.* A, **162,** 122.
[14] HENKEL, C., STEANE, A., KAISER, R., and DALIBARD, J., 1994, *J. Phys., Paris, II*, **4,** 1877.
[15] KOKOROWSKI, D., and PRITCHARD, D., 1997, *J. mod. Optics*, this issue, 2575.
[16] RAMSEY, N. F., 1956, *Molecular Beams* (Oxford University Press).
[17] RABI, I., 1937, *Phys. Rev.*, **51,** 652.
[18] BATTOCLETTI, M., and ENGLERT, B-G., 1994, *J. Phys., Paris, II*, **14,** 1939.
[19] KAISER, H., WERNER, S. A., and GEORGE, E. A., 1983, *Phys. Rev. Lett.*, **50,** 560.
[20] KAISER, H., WERNER, S. A., and GEORGE, E. A., 1983, *Phys. Rev. Lett.*, **51,** 1105.
[21] WERNER, S. A., CLOTHIER, R., KAISER, H., and RAUCH, H., 1991, *Phys. Rev. Lett.*, **67,** 683.
[22] ENGLERT, B.-G., MINIATURA, C., and BAUDON, J., 1994, *J. Phys., Paris, II*, **4,** 2043.

Bibliography

[1] L. De Broglie. *Théses presentées a la Faculté des sciences de L'Université de Paris.* PhD thesis, L'Université de Paris, 1924.

[2] C. Davisson and L. H. Germer. The scattering of electrons by a single crystal of Nickel. *Nature*, 119:558, 1927.

[3] C. Davisson and L. H. Germer. Diffraction of electrons by a crystal of Nickel. *Phys. Rev.*, 30:705, 1927.

[4] G. P. Thomson and A. Reid. Diffraction of cathode rays by a thin film. *Nature*, 119:890, 1927.

[5] L. Marton. Electron interferometer. *Phys. Rev.*, 85:1057, 1952.

[6] L. Marton, J. A. Simpson, and J. A. Suddeth. An electron interferometer. *Rev. Sci. Inst.*, 25:1099, 1954.

[7] H. Maier-Leibnitz and T. Springer. An interferometer for slow neutrons. *Z. Phys.*, 167:386, 1962.

[8] H. Rauch, W. Treimer, and U. Bonse. Test of a single crystal neutron interferometer. *Phys. Lett. A*, 47:369, 1974.

[9] I. Estermand and O. Stern. Diffraction of molecular beams. *Z. Phys.*, 61:95, 1930.

[10] P. E. Moskowitz, P. L. Gould, S. R. Atlas, and D. E. Pritchard. Diffraction of an atomic beam by standing-wave radiation. *Phys. Rev. Lett.*, 51:370, 1983.

[11] P. L. Gould, G. A. Ruff, and D. E. Pritchard. Diffraction of atoms by light: The near-resonant Kapitza-Dirac effect. *Phys. Rev. Lett.*, 56(8):827–830, 1986.

[12] W. Schollkopf and J. P. Toennies. Nondestructive mass selection of small Van der Waals clusters. *Science*, 266:134–1348, 1994.

[13] M. S. Chapman, C. R. Ekstrom, T. D. Hammond, R. A. Rubenstein, J. Schmiedmayer, S. Wehinger, and D. E. Pritchard. Optics and interferometry with Na_2 molecules. *Phys. Rev. Lett.*, 74:4783, 1995.

[14] P. R. Berman, editor. *Atom Interferometry.* Academic Press, San Diego, 1997.

[15] M. S. Chapman, T. D. Hammond, A. Lenef, J. Schmiedmayer, R. A. Rubenstein, E. Smith, and D. E. Pritchard. Photon scattering from atoms in an atom interferometer: Coherence lost and regained. *Phys. Rev. Lett.*, 75:3783, 1995.

[16] D. W. Weiss, B. C. Young, and S.Chu. Precision measurement of the photon recoil of an atom using atomic interferometry. *Phys. Rev. Lett.*, 70:2706–2709, 1993.

[17] C. R. Ekstrom, J. Schmiedmayer, M. S. Chapman, T. D. Hammond, and D. E. Pritchard. Measurement of the electric polarizability of sodium with an atom interferometer. *Phys. Rev. A*, 51:3883, 1995.

[18] A. Peters, K. Y. Chung, B. Young, J. Hensley, and S.Chu. Precision atom interferometry. *Proc. Roy. Soc. A*, 355:2223–2233, 1997.

[19] M. J. Snadden, J. M. McGuirk, P. Bouyer, K. G. Haritos, and M. A. Kasevich. Measurement of the earth's gravity gradient with an atom interferometer-based gravity gradiometer. *Phys. Rev. Lett.*, 81:971–974, 1998.

[20] A. Lenef, T. D. Hammond, E. T. Smith, M. S. Chapman, R. A. Rubenstein, and D. E. Pritchard. Rotation sensing with an atom interferometer. *Phys. Rev. Lett.*, 78:760–763, 1997.

[21] T. L. Gustavson, P. Bouyer, and M. A. Kasevich. Precision rotation measurements with an atom interferometer gyroscope. *Phys. Rev. Lett.*, 78:2046–2049, 1997.

[22] P. J. Martin, P. L. Gould, B. G. Oldaker, A. H. Miklich, and D. E. Pritchard. Diffraction of atoms moving through a standing wave. *Phys. Rev. A*, 36(5):2495–2498, 1987.

[23] P. J. Martin, B. G. Oldaker, A. H. Miklich, and D. E. Pritchard. Bragg scattering of atoms from a standing light wave. *Phys. Rev. Lett.*, 60(6):515–518, 1988.

[24] E. M. Rasel, M. K. Oberthaler, H. Batelaan, J. Schmiedmayer, and A. Zeilinger. Atom wave interferometry with diffraction gratings of light. *Phys. Rev. Lett.*, 75:2633–2637, 1995.

[25] D. M. Giltner, R. W. McGowan, and S. A. Lee. Atom interferometer based on Bragg scattering from standing light waves. *Phys. Rev. Lett.*, 75:2638–2641, 1995.

[26] F. Riehle, T. Kisters, A. Witte, J. Helmcke, and C. J. Bordé. Optical Ramsey spectroscopy in a rotating frame: Sagnac effect in a matter-wave interferometer. *Phys. Rev. Lett.*, 67:177, 1991.

[27] D. W. Keith, C. R. Ekstrom, Q. A. Turchette, and D. E. Pritchard. An interferometer for atoms. *Phys. Rev. Lett.*, 66:2693–2696, 1991.

[28] O. Carnal and J. Mlynek. Young's double-slit experiment with atoms: A simple atom interferometer. *Phys. Rev. Lett.*, 66:2689–2692, 1991.

[29] J. J. Sakurai. *Modern Quantum Mechanics.* Addison-Wesley, Reading, MA, 1985.

[30] W. Pauli. *General Principles of Quantum Mechanics.* Springer, Berlin, 1980.

[31] U. Fano. Description of states in quantum mechanics by density matrix and operator techniques. *Rev. Mod. Phys.*, 29(1):74, 1957.

[32] U. Leonhardt. *Measuring the Quantum State of Light.* Cambridge Studies in Modern Optics. Cambridge University Press, Cambridge, U.K., 1997.

[33] *J. Mod. Optics. Special Issue: Quantum State Preparation and Measurement*, 44(11), November 1997.

[34] D. T. Smithey, M. Beck, M. G. Raymer, and A. Faridani. Measurement of the wigner distribution and the density matrix of a light mode using optical homodyne tomography: Application to squeezed states and the vacuum. *Phys. Rev. Lett.*, 70:1244–47, 1993.

[35] T. J. Dunn, I. A. Walmsley, and S. Mukamel. Experimental determination of the quantum-mechanical state of a molecular vibrational mode using fluorescence tomography. *Phys. Rev. Lett.*, 74(6):884–887, 1995.

[36] D. Leibfried, D. M. Meekhof, B. E. King, C. Monroe, W. M. Itano, and D. J Wineland. Experimental determination of the motional quantum state of a trapped atom. *Phys. Rev. Lett.*, 77:4281–4285, 1996.

[37] U. Janicke and M. Wilkens. Tomography of atom beams. *J. Mod. Opt.*, 42(11):2183–2199, 1995.

[38] M. Freyberger, S. H. Kienle, and V. P. Yakovlev. Interferometric measurement of an atomic wave function. *Phys. Rev. A*, 56(1):195–201, 1997.

[39] S. H. Kienle, D. Fischer, W. P. Schleich, V. P. Yakovlev, and M. Freyberger. Reconstructing quantum states via quantum tomography and atom interferometry. *Appl. Phys. B*, 65:735–743, 1997.

[40] I. A. Walmsley and N. P. Bigelow. Measuring the quantum state of cold atoms using momentum-shearing interferometry. *Phys. Rev. A*, 57(2):R713–R716, 1998.

[41] Ch. Kurtsiefer, T. Pfau, and J. Mlynek. Measurement of the wigner function of an ensemble of helium atoms. *Nature*, 386(13):150–153, 1997.

[42] I. I. Rabi, J. R. Zacharias, S. Millman, and P. Kusch. *Phys. Rev.*, 53:318, 1938.

[43] I. I. Rabi, S. Millman, P. Kusch, and J. R. Zacharias. The molecular beam resonance method for measuring nuclear magnetic moments: The magnetic moments of $_3Li^6$, $_3Li^7$, and $_9F^{19*}$. *Phys. Rev.*, 55:326–35, 1939.

[44] N.F. Ramsey. A molecular beam resonance method with separated oscillating fields. *Phys. Rev.*, 78(6):695–9, 1950.

[45] N. F. Ramsey. *Molecular Beams.* Oxford University Press, Oxford, 1956.

[46] Ch.J. Bordé. Atomic interferometry with internal state labling. *Phys. Lett. A*, 140(1):10–12, 1989.

[47] V. P. Chebotayev, B. Ya. Dubetsky, A. P. Kasantsev, and V. P. Yakovlev. Interference of atoms in separated optical fields. *J. Opt. Soc. Am. B*, 2(11):1791–1798, 1985.

[48] Ch. Miniatura, F. Perales, G. Vassilev, J. Reinhardt, J. Robert, and J. Baudon. A longitudinal Stern-Gerlach interferometer: the "beaded" atom. *J. Phys. II*, 1(4):425–36, 1991.

[49] F. Mezei. Neutron spin echo: A new concept in polarized thermal neutron techniques. *Z. Phys.*, 255:146–160, 1972.

[50] F. Mezei. Coherent approach to neutron beam polarization. In M. Schlenker, M. Fink, J. P. Goedgebuer, C. Malgrange, J. Ch. Vienot, and R. H. Wade, editors, *Imaging Processes and Coherence in Physics: proceedings of a workshop held at the Centre de Physique, Les Houches, France, March 1979*, pages 282–295, Berlin, 1980. Springer-Verlag.

[51] R. Golub and R. Gähler. A neutron resonance spin echo spectrometer for quasi-elastic and inelastic scattering. *Phys. Lett. A*, 123:43–48, 1987.

[52] R. Golub, R. Gähler, and T. Keller. A plane wave approach to particle beam magnetic resonance. *Am. J. Phys.*, 62(9):779–788, 1994.

[53] M. DeKieviet, D. Dubbers, C. Schmidt, D. Scholz, and U. Spinola. ^{3}He spin echo: New atomic beam technique for probing phenomena in the neV range. *Phys. Rev. Lett.*, 75(10):1919–1922, 1995.

[54] G. Badurek, H. Rauch, and D. Tuppinger. Neutron interferometric double-resonance experiment. *Phys. Rev. A*, 34(4):2600–2608, 1986.

[55] M. Moshinsky. Diffraction in time. *Phys. Rev.*, 88(3):625–31, 1952.

[56] S. R. Barone, M. A. Narcowich, and F. J. Narcowich. Floquet theory and applications. *Phys. Rev. A*, 15(3):1109–1125, 1977.

[57] J. Summhammer. Coherent multiphoton exchange between a neutron and an oscillating magnetic field. *Phys. Rev. A*, 47(1):556–65, 1993.

[58] R. Gähler and R. Golub. Time dependent neutron optics — quantum mechanical effects on beam chopping and a new type of high resolution neutron spectrometer (FOTOF). *Z. Phys. B*, 56:5–12, 1984.

[59] J. Felber, G. Müller, R. Gähler, and R. Golub. Time dependent neutron optics: II Diffraction in space and time. *Physica B*, 162:191–6, 1990.

[60] R. Golub and S. K. Lamoreaux. Elucidation of the neutron coherence length and a matter-wave sideband interferometer. *Phys. Lett. A*, 162:122–8, 1992.

[61] C. Henkel, A.M. Steane, R. Kaiser, and J. Dalibard. A modulated mirror for atomic interferometry. *J. de Phys. II*, 4(11):1877–96, 1994.

[62] Č. Brukner and A. Zeilinger. Diffraction of matter waves in space and time. *Phys. Rev. A*, 56(5):3804–3924, 1997.

[63] J. Summhammer, K. A. Hamacher, H. Kaiser, H. Weinfurter, D. L. Jacobson, and S. A. Werner. Multiphoton exchange amplitudes observed by neutron interferometry. *Phys. Rev. Lett.*, 75(18):3206–9, 1995.

[64] J. Felber, R. Gähler, C. Rausch, and R. Golub. Matter waves at a vibrating surface: Transition from quantum-mechanical to classical behavior. *Phys. Rev. A*, 53(1):319–28, 1996.

[65] A. Steane, P. Szriftgiser, P. Desbiolles, and J. Dalibard. Phase modulation of atomic de Broglie waves. *Phys. Rev. Lett.*, 74(25):4972–5, 1995.

[66] P. Szriftgiser, D. Guéry-Odelin, M. Arndt, and J. Dalibard. Atomic wave diffraction and interference using temporal slits. *Phys. Rev. Lett.*, 77(1):4–7, 1996.

[67] S. Bernet, M.K. Oberthaler, R. Abfalterer, Jörg Schmiedmayer, and Anton Zeilinger. Coherent frequency shift of atomic matter waves. *Phys. Rev. Lett.*, 77(26):5160–3, 1996.

[68] E. T. Smith, A. Dhirani, D. A. Kokorowski, R. A. Rubenstein, T. Roberts, H. Yao, and D. E. Prtichard. Velocity rephased longitudinal momentum coherences with differentially detuned separated oscillatory fields. *Phys. Rev. Lett.*, 81:1996–9, 1998.

[69] R. A. Rubenstein, A. Dhirani, D. A. Kokorowski, T. D. Roberts, E. T. Smith, W. W. Smith, H. J. Bernstein, J. Lehner, S. Gupta, and D. E. Pritchard. Search for off-diagonal density matrix elements for atoms in a supersonic beam. *submitted to Phys. Rev. Lett.*, 1999.

[70] R. A. Rubenstein, D. A. Kokorowski, A. Dhirani, W. W. Smith, J. Lehner, S. Gupta, T. D. Roberts, H. J. Bernstein, and D. E. Pritchard. Measurement of the density matrix of a longitudinally modulated atomic beam. *to be submitted to Phys. Rev. Lett.*, 1999.

[71] E. T. Smith. *Velocity Rephased Coherences in a Longitudinal Atom Interferometer.* PhD dissertation, Harvard University, Department of Applied Physics, 1998.

[72] E. L. Hahn. *Phys. Rev.*, 80:580, 1950.

[73] B.-G. Englert, J. Schwinger, A.O. Barut, and M.O. Scully. Reflecting slow atoms from a micromaser field. *Europhys. Lett.*, 14(1):25–31, 1991.

[74] M. Battocletti and B.-G. Englert. Reflecting slow atoms from a damped resonator. *J. de Phys. II*, 14(11):1939–53, 1994.

[75] L. Pumares, L. Plaja, L. Roso, and K. Rzążewski. Stopped atomic wavepackets generated by interaction with a square-profile laser beam. *Quantum Semiclass. Opt.*, 8(3):673–86, 1996.

[76] Ch.J. Bordé. Matter-wave interferometers: A synthetic approach. In P.R. Berman, editor, *Atom Interferometry*, pages 257–92. Academic Press, San Diego, 1997.

[77] C. Brukner and A. Zeilinger. Diffraction of matter waves in space and time. *Phys. Rev. A*, 56(5):3804–3824, 1997.

[78] D. L. Haavig and R. Reifenberger. Dynamic transmission and reflection phenomena for a time-dependent rectangular potential. *Phys. Rev. B*, 26(12):6408–6420, 1982.

[79] D. Dubbers, P. El-Muzeini, M. Kessler, and J. Last. Prototype of a zero-field neutron spin-echo spectrometer. *Nuc. Inst. Meth. A*, 275:294–300, 1989.

[80] T. Keller, R. Golub, F. Mezei, and R. Gähler. Recent developments and results from the neutron resonance spin-echo spectrometer (NRSE) at BENSC berlin. *Physica B*, 234:1126–1127, 1997.

[81] A. Dhirani, D. A. Kokorowski, R. A. Rubenstein, T. D. Hammond, , B. Rohwedder, E. T. Smith, and D. E. Prtichard. Determining the density matrix of a molecular beam using a longitudinal matter wave interferometer. *J. Mod. Opt.*, 44:2583–9, 1997.

[82] H. Kaiser, S. A. Werner, and E. A. George. Direct measurement of the longitudinal coherence length of a thermal neutron beam. *Phys. Rev. Lett.*, 50(8):560–3, 1983.

[83] A. G. Klein, G. I. Opat, and W. A. Hamilton. Longitudinal coherence in neutron interferometery. *Phys. Rev. Lett.*, 50(8):563–5, 1983.

[84] G. Comsa. Comment on 'Direct measurement of the longitudinal coherence length of a thermal neutron beam'. *Phys. Rev. Lett.*, 51(12):1105, 1983.

[85] H. J. Bernstein and F. E. Low. Measurement of longitudinal coherence lengths in particle beams. *Phys. Rev. Lett.*, 59(9):951–3, 1987.

[86] I.I. Rabi. On the process of space quantization. *Phys. Rev.*, 49:324–8, 1936.

[87] R. Golub, R. Gähler, and T. Keller. Neutron resonance spin-echo—a new tool for high resolution spectroscopy. *Physica B*, 180:899–902, 1992.

[88] I.I. Rabi, S. Millman, P. Kusch, and J.R. Zacharias. The molecular beam resonance method for measuring nuclear magnetic moments: The magnetic moments of ${}_3Li^6$, ${}_3Li^7$ and ${}_9F^{19*}$. *Phys. Rev.*, 55:526–35, 1939.

[89] U. Sterr, K. Sengstock, W. Ertmer, F. Riehle, and J. Helmcke. Atom interferometery based on separated light fields. In P.R. Berman, editor, *Atom Interferometry*, pages 293–362. Academic Press, San Diego, 1997.

[90] R.M. Hill and T.F. Gallagher. Deflection of CsF molecules by resonant inhomogeneous electric fields. *Phys. Rev. A*, 12(2):451–9, 1975.

[91] G. Arfken. *Mathematical Methods for Physicists.* Academic Press, San Diego, 1985.

[92] K. Patorski. The self-imaging phenomenon and its applications. In E. Wolf, editor, *Progress in Optics, XXVII*, pages 1–108. North-Holland, Amsterdam, 1989.

[93] L. D. Landau and E. M. Lifshits. *Quantum Mechanics: Non-Relativistic Theory.* Pergamon Press, Oxford, U.K., 1977.

[94] D.A. Kokorowski and D.E. Pritchard. Longitudinal quantum beam tomography. *J. Mod. Opt.*, 44:2575–81, 1997.

[95] M. Hillery, R. F. O'Connell, M. O. Scully, and E. P. Wigner. Distribution functions in physics: Fundamentals. *Phys. Reports*, 106(3):121–167, 1984.

[96] B.-G. Englert, C. Miniatura, and J. Baudon. Least-bias description of atomic beams. *J. de Phys. II*, 4(11):2043–59, 1994.

[97] D. W. Keith. *An Interferometer for Atoms.* PhD dissertation, Massachusetts Institute of Technology, Department of Physics, 1991.

[98] M. G. Raymer. The Whittaker-Shannon sampling theorem for experimental reconstruction of free-space wave packets. *J. Mod. Opt.*, 44:2565–2574, 1997.

[99] D. E. Pritchard, R. A. Rubenstein, A. Dhirani, D. A. Kokorowski, E. T. Smith, T. D. Hammond, , and B. Rohwedder. Longitudinal atom optics using localized oscillating fields: A fully quantum mechanical treatment. *submitted to Phys. Rev. A*, 1998.

[100] W. H. Press, S. A. Teukolsky, W. T. Vetterling, and B. P. Flannery. *Numerical Recipes in C: The Art of Scientific Computing.* Cambridge University Press, Cambridge, U.K., 1988.

[101] C. R. Ekstrom. *Experiments with a Separated Beam Atom Interferometer.* PhD dissertation, Massachusetts Institute of Technology, Department of Physics, 1993.

[102] M. S. Chapman. *Photon Induced Coherence Loss in Atom Interferometry.* PhD dissertation, Massachusetts Institute of Technology, Department of Physics, 1995.

[103] P. Horowitz and W. Hill. *The Art of Electronics.* Cambridge University Press, Cambridge, U.K., 1980.

[104] T. D. Hammond. *Atom Interferometry: Dispersive Index of Refraction and Rotation Induced Phase Shifts for Matter-Waves.* PhD dissertation, Massachusetts Institute of Technology, Department of Physics, 1997.

[105] E. Majorana. *Nuovo. Cim.*, 9:43, 1932.

[106] W. Ketterle and H.-J. Miesner. Coherence properties of Bose-Einstein condensates and atom lasers. *Phys. Rev. A*, 56:3291–93, 1997.

[107] J. Robert, Ch. Miniatura, S. Nic Chormaic, J. Lawson-Daku, O. Gorciex, F. Perales, and J. Baudon. Angular correlation measurements in a thermal beam of $H^*(2s)$ atoms using a Stern-Gerlach atomic axicon. *J. de Phys. II*, 4(11):2061–71, 1994.

[108] H. Kaiser, S. A. Werner, and E. A. George. Comment on 'Direct measurement of the longitudinal coherence length of a thermal neutron beam' (and reply). *Phys. Rev. Lett.*, 51(12):1105–6, 1983.

[109] B. Saubaméa, T. W. Hijmans, S. Kulin, E. Peik, M. Leduc, and C. Cohen-Tannoudji. Direct measurement of the spatial correlation function of cold atoms. *Phys. Rev. Lett.*, 79(17):3146–9, 1997.

[110] V. L. Lepore. Density-matrix description of neutron-interferometry experiments. *Phys. Rev. A*, 50(6):5014–7, 1994.

[111] J. D. Scargle. Studies in astronomical time series analysis. II. Statistical aspects of spectral analysis of unevenly sampled data. *Astrophys. J.*, 263:835–853, 1982.

[112] J. H. Horne and S. L. Balliunas. A prescription for period analysis of unevenly sampled time series. *Astrophys. J.*, 302:757–763, 1986.

[113] J. R. Taylor. *An Introduction to Error Analysis.* University Science Books, Mill Valley, CA, 1982.

[114] U. Leonhardt and M. G. Raymer. Observation of moving wave packets reveals their quantum state. *Phys. Rev. Lett.*, 76(12):1985–1989, 1996.

[115] R. A. Rubenstein. *Longitudinal Atom Optics: Measuring the Density Matrix of a Matter Wave Beam.* PhD dissertation, Massachusetts Institute of Technology, Department of Physics, 1999.

[116] M.-O. Mewes, M. R. Andrews, D. M. Kurn, D. S. Durfee, C. G. Townsend, and W. Ketterle. Output coupler for Bose-Einstein condensed atoms. *Phys. Rev. Lett.*, 78(4):582–585, 1997.

[117] M. R. Andrews, C. G. Townsend, H.-J. Meisner, D. S. Durfee, D. M. Kurn, and W. Ketterle. Observation of interference between two Bose condensates. *Science*, 275:637–640, 1997.

[118] H. Hinderthür, A. Pautz, V. Rieger, F. Ruschewitz, J. L. Peng, K. Sengstock, and W. Ertmer. Three-beam atom interferometer. *Phys. Rev. A*, 56:2085–2089, 1997.

[119] T. D. Hammond, D. E. Pritchard M. S. Chapman, A. Lenef, and J. Schmiedmayer. Multiplex velocity selection for precision matter-wave interferometry. *Appl. Phys. B*, 60:193–197, 1995.

Acknowledgments

I have a large number of people to thank for their support and friendship. Without them, neither my graduate career at MIT nor the work described in this thesis would have been possible.

My first thanks must go to my advisor, Professor David E. Pritchard. A good advisor's job is to provide a balance of criticism and support, encouraging a student to grow into an accomplished physicist. I can say without reservation that in my case Dave has performed this task with patience and distinction. Of course, I learned a tremendous amount of physics from him. Perhaps more importantly, Dave encouraged me to communicate effectively and to rapidly distinguish between the essential and the extraneous. I'll use what I've learned from him for a long time to come.

The previous graduate students I worked with over the past years have been good friends and important influences on my scientific development. Chris Ekstrom's wide ranging interests and physical intuition were models for me when I first joined the interferometer group in 1993. Mike Chapman's productivity and powerful personality made him an effective physicist, whose mark on our group still remains. Troy Hammond's physical insight, along with his patience, tact, and motivational abilities, taught me a lot of physics, but even more about how to work with other people. Mike and Troy also gave me a plethora of techniques for running our atomic beam machine.

The structure of our research group made Edward Smith and David Kokorowski, the graduate students immediately preceding and following me, very important to my scientific development and my ability to accomplish the experiments described in this thesis. I shared an office with each, spent innumerable all-nighters taming a recalcitrant apparatus with their aid, and many hours with them at the blackboard wading through tough physics problems. I am fortunate to count them among my best friends.

Edward Smith lead the charge to build our new apparatus. Its nearly flawless functioning over the last year and a half is a testament to the skill with which he accomplished this task. He also blazed a path through the unfamiliar techniques

of molecular beam resonance, leaving a trail I followed on every experimental run. I learned a lot about design from Edward, but even more from his relentless and creative solutions to all sorts of problems, whether he was extracting a crucial part from a recalcitrant vendor, or making the radical changes to the magnetic field geometry in our machine that lead to a functioning longitudinal interferometer.

Looking back over acknowledgment sections of past graduates, I've noticed they rarely mention learning from younger students. I learned a lot from David Kokorowski. We've had many discussions that influenced the work in this thesis, in particular about the correspondence between classical and quantum descriptions of our experiments. I have always been impressed by his keen physical insights and found him an invaluable resource for theoretical issues, data analysis, and experimental problems. His computer skills enabled all of our data acquisition over the past two and a half years. In the many papers we've worked on together, his incisive comments improved the prose and sharpened the science. I know that with him, the future of the experiment is in the best of hands.

The rest of the current crew, Tony Roberts, Deep Gupta, and post-doc Jana Lehner, have also been valuable friends and colleagues, crucial to the success of our collective research efforts over the last year. I must in particular thank Tony for his help with acquiring our final deconvolution data, and Jana and Deep for assistance with the modeling and analysis of this data. Together, we got a superior final product, one that we could not have achieved working individually. I think we had some fun, too.

The two other post-docs with whom I've worked in my years at MIT have been important influences as well. Al Lenef seemed to know something about everything and was always generous with his time. He and his wife Lori (and their daughter Julia) have become my good friends. I must also acknowledge the important contributions of Al-Amin Dhirani. The insights I gained from him about the theory of DSOF rephasing, along with his theoretical work on the density matrix deconvolution algorithm, were enabling ideas for our experiments.

I was fortunate to have the assistance of Professors Winn Smith (University of

Connecticut) and Herb Bernstein (Hampshire College). Winn's work on the three-state Ramsey problem was a key element of the deconvolution experiment. Herb's work on longitudinal coherence first attracted us to this field, and his insights greatly strengthened our papers. I also thank undergraduate students Huan Yao and Aron Qasba for their work on our experiments.

Visiting scientists Jörg Schmiedmayer, Marek Czachor, and Bernt Rohwedder round out the list of people who have contributed to our group during my tenure here. Jörg, a regular visitor from his own lab in Innsbruk, has in particular been a great source of ideas and advice for everyone in our group.

The other half of the Pritchard group, the ICR experiment, has provided still more great people. I had many late night discussions with the present ICR graduate students Mike Bradley, Simon Rainville and James Thompson, and post-doc Trey Porto. I and also interacted with past team members Vasant Natarajan, Frank DiFillipo, and Fred Palmer.

The wider atomic physics community has been another valuable resource during my time here. Professor Wolfgang Ketterle's group, just next door to our lab, has provided a wealth of borrowed equipment and interesting colleagues. I thank Wolfgang himself for his friendly advice, for agreeing to serve on my thesis committee, and for his careful reading of this document. The explosive growth of Wolfgang's group over the last five years makes his BEC group too numerous to acknowledge everyone individually. I had particularly valuable conversations with Mike Andrews, Dan Stamper-Kurn, Marc-Oliver Mewes, Mike Joffe, Hans-Joachim Meisner, Klaasjan van Druten, Dallin Durfee, and Chandra Raman.

At the other end of the hall, Dan Kleppner's Rydberg atom workers were another important resource. Jeff Holley and Neal Spellmeyer were particularly generous with their time and equipment, and I've talked over a lot of great physics with them, as well as with Joel DeVries, Robert Lutwak, and Hong Jiao. The hydrogen BEC gang in Building 13: Dale Fried, Tom Killian, Steve Moss, and David Landhuis, were always willing to lend us yet more equipment (in particular one of the HP8662A frequency synthesizers we needed for our experiments), and showed remarkable restraint when

we needed it for much longer than anticipated.

Other important people at MIT include a list of friends from outside the AMO community: Pete Steinberg, Ibo Mathews, Sandra Brown, Patrick Wojdowski, Dan Ripin, and Yuliya Vugmeyster.

I must take this opportunity to thank some of MIT staff that enable our research to go smoothly. Carol Costa, the AMO administrative assistant always checks up on all of the students on the hall, and goes well out of her way to make our lives easier. Our friendly conversations often re-injected an aura of normality to the crazy environment MIT sometimes presented. Physics Department administrators Peggy Berkovitz and Pat Solakoff kept track of all the details and arranged smooth sailing through the maze of departmental demands. The RLE administrative staff, in particular Maxine Samuels, also deserve my sincere thanks. Maxine, the RLE purchasing agent, always responded with skill and patience when we urgently needed parts "yesterday." The guys in the LNS machine shop provided first rate service: Peter, Andy, and the rest always managed to sneak our rush jobs to the top of the list, and consistently delivered excellent final products.

Several physicists from Amherst College, in particular Professors Larry Hunter (my undergraduate research advisor), Bob Romer (editor of the American Journal of Physics, where I worked as an editorial assistant), and Steve Blau (formerly of Amherst and now of Ripon College), and Bob Hilborn all contributed in important ways to my development as a physicist. Steve Peck, then a graduate student of Prof. Hunter, was another big influence.

Switching gears to my life outside physics, I've got even more people to thank, and just as much to be thankful for.

My wife, Patricia Anne Rubenstein, has borne the cost of graduate school to our marriage with more tolerance than I could ask. Being the spouse of a graduate student is no picnic. Money is tight, schedules are uncertain, and stress is high. The nights when I was not at home to be with her are too numerous to count. While she contributed in important ways to my accomplishments at MIT, at the end of the day I've received a Ph.D., while she will not be fully recognized. I can't change this, but

I can thank her, and acknowledge her contributions here.

Patricia's success in her own alumni relations career, highlights her remarkable abilities. I do not know anyone who is as sensitive to the needs of others. I've often asked her advice in how to sort out an issue in the personal interactions of laboratory life, and always found her intelligent insights worth seeking. Her grace under pressure and her organizational skills are unmatched. We are truly a team, and I thank her for her love, advice, friendship, and support over the last five and a half years. I could not have done it without her.

Patricia and I have been blessed with a large and wonderful family. My parents, Morton and Myrna Rubenstein, taught me to think, to work, and to get along. Their love, encouragement, and support made my studies possible. Marge and Vibart Henriques have also been supportive, helpful, and understanding. My brothers Lee and Stephen, along with my sister-in-law Christina and her fiancé Kevin, have all been friends and distractions from the rigors of MIT. I also thank Charles and Dottie Russek for their warm hospitality during the three months I stayed with them while finishing my graduate work, and Stephanie and Vincent Demma for assistance to Patricia during her move to Washington.

Finally, I'd like to thank the community of Temple Emunah for being so hospitable and friendly. Patricia and I enjoyed our time there, and will miss everyone more than we can say. Our special thanks must go to our chavurah, and all the great people in it: Robert and Debbie Cohen, Kevin and Lee Ann Best, Wayne and Robin Goldstein, Bennett and Dina Savitz, and Eric Goldstein and Audrey Tolman.